
Parameter Uncertainties in Tracer Kinetic Modelling of Dynamic Contrast Enhanced MRI

Limitations from Arterial Input Functions, Data Acquisition and Choice of Model



Tammo Rukat

Born on the 12th of December 1988 in Berlin

Department of Physics

Humboldt-Universität zu Berlin

Submitted in fulfillment of the requirements for the academic degree of

Master of Science in Physics

1st of October 2013

1. Reviewer: PD Dr. Niels Wessel
2. Reviewer: Prof. Dr. Stefan A. Reinsberg

Abstract

The delineation of tumor tissue with dynamic contrast-enhanced magnetic resonance imaging (DCE-MRI) is of great interest for cancer treatment monitoring and for a broad spectrum of clinical and pre-clinical research. By means of a simulation study, the precision and accuracy of haemodynamic parameters in DCE-MRI with five tracer kinetic models is investigated.

The impact of variations in the injection speed of the contrast agent is examined, as well as the effect of deficient arterial input functions, i.a. errors in haematocrit and the bolus arrival time and the bolus peak. The benefits of weighted multi-model parameter estimates with Aikaike's and the Bayesian information criterion are studied, as well as the dependence of model precision and accuracy on the SNR.

Fast injections are beneficial for the precision of the volume transfer constant, K^{trans} , within the extended Tofts model for typical arterial input functions (AIFs) in a mouse and within the two-compartment exchange model for typical human and mouse AIFs. They have no notable effect for the other models under investigation. Biases from errors in the AIF are mostly consistent in size and direction for the simple and the extended Tofts model, while they are hardly predictable for the other models. Errors in the haematocrit introduce the strongest loss in parameter accuracy, amounting to an average K^{trans} bias of 40% for a 30% overestimation throughout all models and individual measurements may be of advisable. Overestimations of the bolus amplitude introduce a significantly more severe bias than underestimation.

The benefit of SNRs higher than 50 is very limited, except for the two-compartment exchange model, which gains significantly in accuracy and precision from SNRs of 100 and higher. AIC and BIC weighted estimates perform roughly as good as the model with the best performance, respectively. For all investigated situations collectively, the weighted parameter estimates perform clearly better than any of the single models.

For Jihyun Annie Park

Acknowledgements

First of all I want to thank Stefan Reinsberg from the University of British Columbia for introducing me into the field of DCE-MRI, for giving me the possibility to do this research and for supporting me with intense discussions and most helpful collaboration and advice. I want to thank Simon Walker-Samuel from University College London for his ideas and collaboration, as well as Niels Wessel from Humboldt Universität zu Berlin for his ongoing support.

Furthermore, I would like to thank Firas Moosvi and Jen Moroz from the SARlab group at UBC for rewarding dicussions and pleasurable company. Thanks to Piotr Kozlowski and Andrew Yung from the UBC 7T group for helpful discussions and suggestions.

I also wish to express my gratitude to the University of British Columbia for facilitating my stay and my reserch in Vancouver and to Evangelisches Studienwerk Villigst, for funding it.

Finally I want to express my gratitude to my parents for their manifold support, their confidence and love.

Contents

List of Abbreviations	vii
1 Motivation and Purpose	1
2 Principles of DCE-MRI	5
2.1 MRI Technique for Rapid Imaging	6
2.2 Contrast Agents	8
2.3 Tumor Physiology and Contrast Agent Uptake	9
3 Compartmental Modelling	11
3.1 Tofts models and the Impulse Response Formalism	11
3.2 The two-compartment exchange model	15
3.3 The Tissue Homogeneity Model and its Adiabatic Approximation	15
3.4 Distributed parameter model	17
3.5 Further Models	17
4 Simulation of Contrast Agent Input and Uptake	19
4.1 AIFs for Arbitrary Injection Rates	19
4.2 Tissue Uptake Simulation with MMID4	22
4.3 Systematic AIF Mismeasurements	23
4.3.1 Error in the Bolus Arrival Time	24
4.3.2 Error in the haematocrit	25
4.3.3 Error in the Peak Position	25
5 Data Fitting and Estimation the Sampling Distribution	29
5.1 Parametric Bootstrap	29
5.2 Simulating Noise	30
5.3 Fitting Algorithm and Initial Parameters	31

CONTENTS

5.4 AIC and BIC weighted Parameter Estimates	31
6 Accuracy and Precision of Haemodynamic Parameters	35
6.1 Variation of the Injection Speed	36
6.2 Mismeasurements in the AIF	43
6.2.1 Rate and Bolus Arrival Time	45
6.2.2 Haematocrit	49
6.2.3 Horizontal and peak AIF concentration	52
6.3 Variation of the SNR	56
6.4 Information Criteria Weighted Parameter Estimates	59
7 Discussion and Conclusion	65
Appendices	69
A Solution of the Rate Equation for the TM	71
B Additional Figures	73
B.1 Accuracy and Precision for various Injection Speeds	74
B.1.1 Mouse AIFs, Negligible Vascular Volume	74
B.1.2 Human AIFs, significant Vascular Volume	78
B.1.3 Human AIFs, negligible Vascular Volume	82
B.2 Accuracy and Precision for Deficient AIFs	86
B.2.1 Error in the Bolus Arrival Time	86
B.2.2 Error in the Hematocrit	89
B.2.3 Error in the Injection Rate	91
B.2.4 Error in the Vertical Peak Position	94
B.2.5 Error in the Horizontal Peak Position	97
B.3 AIC weighted Parameter Estimates for a Human AIF	100
Index	103
References	105

List of Abbreviations

c_v	coefficient of variation
<i>E</i>	extraction fraction
<i>K^{trans}</i>	volume transfer constant
<i>PS</i>	permeability surface area product
<i>v_e</i>	fractional volume of the EES
<i>v_p</i>	fractional volume of the plasma space
2CXM	two-compartment exchange model
accy	accuracy
AIF	arterial input function
ATHM	adiabatic approximation to the tissue homogeneity model
BAT	bolus arrival time
CA	contrast agent
DCE	dynamic contrast enhanced
DPM	distributed parameter model
EES	extravascular extracellular space
ETM	extended Tofts model
FLASH	fast low angle shot
HCT	haematocrit

LIST OF ABBREVIATIONS

IQR	interquartile range
IRF	impulse response function
THM	tissue homogeneity model
TM	Tofts model
var	variance
VS	vascular space

1

Motivation and Purpose

Microvasculature characteristics are known to be an essential biomarker for a disease progression, in particular for the development of tumors, whose rapid angiogenesis produces poorly organized hyperpermeable vessels [Barrett *et al.*, 2007; Folkman, 2002]. As a noninvasive imaging technique, dynamic contrast enhanced (DCE) MRI is therefore increasingly used in drug development [O'Connor *et al.*, 2007], the monitoring of treatment effect [Hodgson *et al.*, 2007; Kershaw *et al.*, 2008] and pathophysiology of such tissues [Benjaminsen *et al.*, 2008; Sourbron *et al.*, 2009; Tofts *et al.*, 1995]. An introductory review is given by Yankeelov & Gore [2009]. Pharmacokinetic models are widely used for the data analysis of DCE MRI and are meant to map the physiological properties of the tissue onto a set of haemodynamic parameters. A recent comprehensive review of available models is given by Sourbron & Buckley [2013]. Most frequently applied are the Tofts (TM) and the extended Tofts model (ETM) [Tofts, 1997], which facilitate the quantification of the volume transfer constant (K^{trans}), a measure that contains information about the blood flow, the microvascular permeability and surface area. Additional parameters are the volume of the extracellular extravascular space (v_e) and, for the extended model, the plasma volume (v_p).

In recent years, the improvement of data quality gave rise to the application of more complex models, which allow for a separate quantification of the blood flow and the permeability-surface area. In particular the two-compartment exchange model (2CXM) [Donaldson *et al.*, 2010, 2011; Thomassin-Naggara *et al.*, 2010], the adiabatic approximation to the tissue homogeneity model (ATHM) Bisdas *et al.* [2008]; Korpela *et al.* [2012]; Michoux *et al.* [2008]; Naish *et al.* [2009], and the distributed parameter model (DPM) [Bisdas *et al.*, 2008; Koh *et al.*, 2011a,b] have been shown to be applicable in various clinical and preclinical contexts. It is of great importance to understand the re-

1. MOTIVATION AND PURPOSE

liability and accuracy of haemodynamic parameter estimates from different models and a number of studies have addressed this issue in the last decade, mostly focusing on the Tofts models [Buckley, 2002; De Naeyer *et al.*, 2011; Garpebring *et al.*, 2012; Kershaw & Buckley, 2006]. Almost all of these studies used one of the above mentioned models to produce the ground-truth, tissue-uptake curves, even though this entails a broad simplification of the tissue physiology, and makes it difficult to distinguish, whether impairments in the accuracy and precision of model estimates originates from the model fit or the generation of the data to be fit. Merely Buckley [2002] suggested the use of the distinctly more complex MMID4 (Multiple path, Multiple tracer, Indicator Dilution, 4 region) model¹ Kroll *et al.* [1996]. This strategy has been adopted throughout this study.

The dependence of the parameter accuracy on errors in the arterial input function (AIF) has previously been investigated for the ATHM [Kershaw & Cheng, 2010] and for the ETM [Cheng, 2008]. E.g. the latter reported a K^{trans} and v_p error that is inversely proportional to an error of the AIF peak amplitude. However, the scope of these investigations was substantially limited regarding the range of tissue parameters and the number of investigated models. Overall, very little attention was paid towards parameter precision. Solely Aerts *et al.* [2008] showed an improved precision for higher contrast agent injection speeds and higher volumes within the ETM for a limited range of tissue parameters.

The study presented here aims to give a more comprehensive account of the accuracy and the precision of the five above mentioned models by means of a parametric bootstrap analysis. Practically relevant situations, that are a potential subject of variation by the investigator, are considered and include:

- The functional form of the arterial input function (AIF) and its accuracy.
- The signal-to-noise ratio (SNR).
- The choice of model or model selection criteria.

By denoting estimates with a hat and by choosing K^{trans} as exemplary haemodynamic parameter the objective of this work can be formalized as determining the accuracy and precision of the following quantity and the dependency on its parameters:

$$\hat{K}^{trans}(\text{AIF}, \text{accy(AIF)}, \text{SNR}, \text{model}) \quad (1.1)$$

¹<http://physiome.org/jsim/models/webmodel/NSR/MMID4/>

In particular the following questions are to be addressed and the immediately associated answers given in the Conclusion (page 65):

1. How does the width of the AIF peak affect the parameter estimates. Does a more δ -like AIF, i.e. a fast injection of contrast agent (CA), improve the precision?
2. To what extent does a lack of knowledge of the true AIF affect the precision and accuracy of haemodynamic parameters? How is the connection to the strength and the type of the AIF bias, as for example the bolus arrival time, the haematocrit or the injection rate?
3. How strongly do parameters estimates benefit from an improved SNR? What model is appropriate for a certain SNR?
4. Do model selection criteria (AIC or BIC) improve the parameter precision or accuracy?

1. MOTIVATION AND PURPOSE

2

Principles of DCE-MRI

Dynamic Contrast-Enhanced MRI is the time resolved acquisition of MR images, before, during and after the admission of an intravenous contrast agent. Rapid acquisition of T1 or T2 weighted images allows to determine the concentration of the contrast agent in the body in a time resolved manner. The resulting quantification of blood flow and vessel characteristics, especially in pathological tissue, is of great interest for scientists and clinicians, as they allow to detect the presence of diseases, the extent of the diseases and the effect of treatment [Choyke *et al.*, 2003; Jackson *et al.*, 2005]. This holds especially for the angiogenesis of tumor tissue and the effect of anti angiogenic drugs. Fig. 2.1 depicts the structure of a complete DCE-MRI experiment.

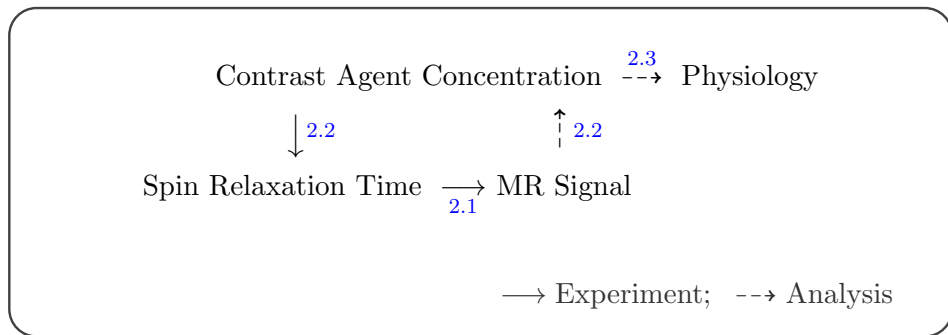


Figure 2.1: Experimental Flowchart – A paramagnetic contrast agent (CA) is injected into the vasculature, from where it might extravasate into surrounding tissues. It is designed to shorten the spin-lattice or spin-spin relaxation time constants of the hydrogen protons in the tissue (sect. 2.2). These changes can be measured in a spatially and time resolved fashion, by means of a rapid MR imaging technique (sect. 2.1). Thereupon voxel-wise CA uptake curves are calculated from the dynamic MR images (sect. 2.2). Eventually, physiological information is derived from these uptake curves (sect. 2.3).

2. PRINCIPLES OF DCE-MRI

The flow of the experimental procedure and the subsequent analysis is represented by the solid and dashed arrows, respectively. Each of these steps is discussed in more detail in the following sections, as indicated.

This chapter is not meant to be a comprehensive introduction to magnetic resonance principles and imaging techniques, nor to DCE-MRI or its role in Oncology. It rather introduces the basic concepts that are of immediate importance for this study, while a basic understanding of NMR and MRI is required. The interested reader is referred to the rich body of textbooks and review papers. Thorough introductions to the principles of magnetic resonance for physicists are given by [Slichter \[1990\]](#) and [Levitt \[2008\]](#). The basic concepts of magnetic resonance imaging are described by [Weishaupt *et al.* \[2006\]](#), while a more involved treatment for physicists is given by [Kuperman \[2000\]](#). Pulse sequences and other technical topics can be found in [Bernstein *et al.* \[2004\]](#).

The role of DCE-MRI for Oncology has been reviewed in great detail by [Jackson *et al.* \[2005\]](#) and more recently by [Yankelev & Gore \[2009\]](#).

2.1 MRI Technique for Rapid Imaging

Short repetition times (TR) allow for fast imaging on the order of 10^{-1} s to 10^1 s, while only a single K space line is acquired for each repetition. The tradeoff between signal strength and time resolution is optimized by using a fixed flip angle, known as the *Ernst Angle*, which has first been derived by [Ernst & Anderson 1966](#).

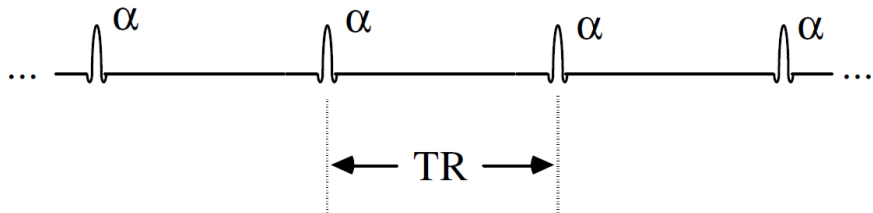


Figure 2.2: RF pulses with flip angle α , with repetition time TR . (Adopted from [Xiang \[2012\]](#))

For a series of radio frequency (RF) pulses with a flip angle α , as shown in Fig. 2.2, the transverse magnetization M_T in the excited slice is proportional to the signal. After application of an RF pulse with flip angle α it can be written as

$$M_T(0) = M \sin \alpha , \quad (2.1)$$

where M is the longitudinal magnetization before the excitation. The residual longi-

2.1 MRI Technique for Rapid Imaging

tudinal magnetization after application of the pulse is then given by:

$$M_L(0) = M \cos \alpha. \quad (2.2)$$

Between two RF pulses the longitudinal magnetization recovers according to:

$$M_L(t) = M + [M_L(0) - M] \exp \left[\frac{t}{T_1} \right]. \quad (2.3)$$

Thus for long TR (large values of t in the above equation), the longitudinal magnetization recovers fully to its initial value. Following eq. (2.1) a flip angle of 90° creates the strongest signal. For short TR on the other hand, a flip angel of 90° does not allow for sufficient recovery of the longitudinal magnetization for the next RF pulse. Following from eqs. (2.2) and (2.3) the longitudinal magnetization right before application of the nth RF pulse is given by:

$$M_L[(n+1)TR] = M + [M_L(nTR) \cos(\alpha) - M] \exp \left[\frac{-TR}{T_1} \right]. \quad (2.4)$$

After a sufficient number of RF pulses a steady state (SS) in the longitudinal magnetization, $M_L^{SS} = M_L[(n+1)TR] = M_L[nTR]$, will be reached. Then eq. (2.4) yields:

$$M^{SS} = M \frac{1 - E}{1 - E \cos(\alpha)}. \quad (2.5)$$

Here, the abbreviation $E := \exp[TR/T_1]$ is introduced. Following eq. (2.1), transverse magnetization (which is proportional to the signal) is then given by:

$$M_T^{SS} = M \sin(\alpha) \frac{1 - E}{1 - E \cos(\alpha)}. \quad (2.6)$$

Its maximization with respect to α yields the expression, that defines the *Ernst angle*:

$$\cos \alpha_{Ernst} = \exp \left[\frac{-TR}{T_1} \right]. \quad (2.7)$$

Using this flip angle allows for significant reduction of the repetition time, while there is still a reasonable signal magnitude. It gives rise to the fast low angle shot technique (FLASH), which is a gradient echo sequence, differing from a conventional gradient echo merely by the small flip angles. Many modifications have been proposed, e.g. spoiled gradient acquisition in steady state (SPGR), where gradient spoilers are added

2. PRINCIPLES OF DCE-MRI

to dephase the residual transverse magnetization after every sequence. This and other related sequences are discussed in great detail in [Bernstein et al. \[2004\]](#), chap. 14]. However, they all comply with the signal eq. (2.6), as derived above. This equation relates the spin-lattice relaxivity, T_1 , to the MR signal. As the following section points out DCE-MRI contrast agents act by changing the T_1 relaxivity and therefore eq. (2.6) is of fundamental importance for this study.

2.2 Contrast Agents

Contrast agents (CAs) for DCE-MRI are designed to change the characteristic T_1 (spin-lattice) or T_2 (spin-spin) relaxation time constants of the tissue. This study focuses on the analysis of T_1 weighted images. Therefore notation and discussion are limited to T_1 altering agents. Nevertheless, the basic relations that are discussed in this section are valid for changes in T_2 relaxation times, as well.

Typically, stable chelates of paramagnetic ions, such as gadolinium, iron, or manganese are used. These ions feature unpaired electrons in their outer orbits, which create local magnetic fields. These fields eventually cause a reduction of the relaxation time constants in the tissue. A more comprehensive discussion is given in the review by [Yankelev & Gore \[2009\]](#). It is important to point out, that it is not the actual CA which is imaged, but rather the relaxation time constants of the molecules in vicinity of the contrast agent. The CA is only indirectly observed, not as for example in contrast enhanced x -ray imaging where the direct effect of iodine CAs is observed.

It has been shown in a variety of studies, that the change in Gadolinium concentration is inversely proportional to the change in relaxation time over a sufficiently wide range (for discussion see e.g. [Jackson et al. \[2005\]](#)). With due regard to the baseline relaxation time ($T_{1,0}$) and with neglecting any BMS¹ shift, the dependency of CA concentration on the relaxation time can be described according to the Solomon-Bloembergen equation [[Freeman & Gowland, 1994](#)]:

$$\frac{1}{T_1} = \frac{1}{T_{1,0}} + r_1[Gd]. \quad (2.8)$$

Here r_1 is the relaxivity constant, which signifies the change in relaxation time of hydrogen atom per time and concentration.

T_1 enhancement effects are present only in the near vicinity of the agent. They are

¹Bulk magnetic susceptibility. A discussion of its effect is given by [Chu et al. \[1990\]](#).

2.3 Tumor Physiology and Contrast Agent Uptake

caused by the weak dipole-dipole interaction between the nuclear magnetic moments. Thus they are mostly observed in areas of a uniform contrast agent concentration. This makes T1 weighting imaging the common choice for the imaging of tumors, where the contrast agent usually leaks from the blood pool and no barriers are present.

An inhomogeneous distribution of paramagnetic ions causes a relatively long range gradient magnetic field, which causes dephasing of the transverse magnetization and thus shortens T2. This effect is dominating for a strong compartmentalization of contrast agent. Its long range nature lets a small amount of contrast agent in the vascular space dominate any relaxivity, even far beyond the vessel walls. This makes T2 weighting the common choice for the imaging of contrast agent behind an intact blood-brain barrier.

More general, CAs can be classified by their molecular weight which ranges from about 500 D to more than 5 kDa, where heavier molecules are often used to prolong the intravascular retention in order to quantify the leakiness of vessels, as discussed by [Barrett et al. \[2007\]](#).

The contrast agent is typically injected via a catheter into a peripheral vein. It circulates throughout the body and may diffuse in surrounding tissues before it reaches the artery of interest. This makes it difficult to estimate the incoming amount of contrast agent in a certain region. The corresponding concentration time course is the aforementioned arterial input function (AIF).

2.3 Tumor Physiology and Contrast Agent Uptake

The maximum diameter of an avascular tumor does not exceed a few mm³ [[Yankeeov & Gore, 2009](#)] and is essentially limited by the diffusion range of oxygen. Thus further tumor growth is necessarily connected to vascularization of the tumor, which is achieved by stimulation of surrounding blood vessels, a process known as *angiogenesis* [[Folkman, 1995, 2002; Ribatti et al., 2000](#)]. The structural maturation of the new vessels is slow, compared to their rapid growth, such that especially fast growing, malignant tumors feature a disorganized system of vessels, which are coarse and dilated, have twisting and sharp bends and large gaps between the endothelial cells. This is shown for different tissue types and corresponding tumors in Fig. 2.3.

Hence, the tumor capillaries are very leaky and intravascular administered contrast agent rapidly permeates the vessel walls into to extravascular extracellular space (EES) by passive diffusion [[Knopp et al., 1999; Padhani, 1999](#)]. Together with the overall high vascularity this leads to a notably faster DCE-MRI signal enhancement in malignant

2. PRINCIPLES OF DCE-MRI

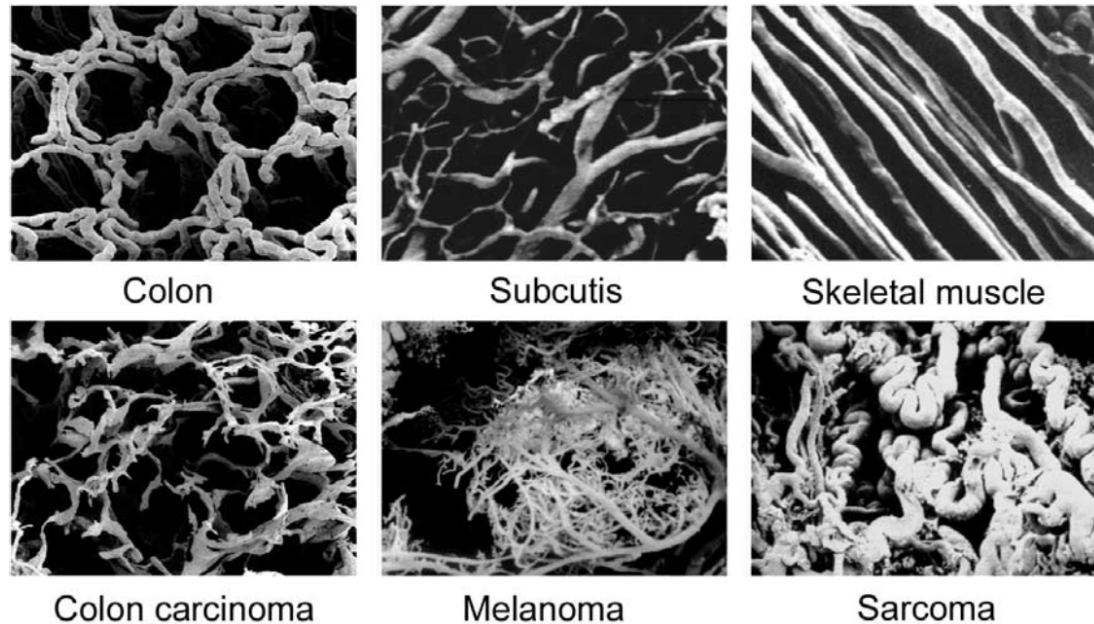


Figure 2.3: Representations of normal vasculature (top) and tumor vasculature (bottom) (adopted from [Vaupel \[2004\]](#), courtesy of M.A. Konerding)

tumors compared to normal tissue.

In addition to the mere characterization of the tumor tissue, the vascularity itself is a target of cancer treatment by anti angiogenic drugs [[Bagri *et al.*, 2010](#)]. Furthermore it is of importance, as the tumor oxygenation plays a crucial role in radiation therapy [[Evans & Koch, 2003](#)].

3

Compartmental Modelling

The commonly used models for contrast agent (CA) uptake are based on rate equations for the diffusive transport across selectively permeable membranes. This approach was first introduced by [Kety \[1951\]](#) in the context of general gas exchange and by [Crone \[1963\]](#) in the context of indicator¹ diffusion. A detailed introduction is given by [Jackson *et al.* \[2005, chap. 6\]](#) and a comprehensive review of available models by [Sourbron & Buckley \[2013\]](#).

Physiological systems are considerably more complex than a single membrane and thus it is important to notice, that all derived parameters are bulk parameters. In the following, five different models, which are used throughout this study are described and summarized in Tab. 3.2. They can all be expressed within the same impulse response formalism, as it is introduced in the next section. An overview of all model parameters that are used in this study is given in Tab. 3.1. Other representations and parameters may be advantageous in some cases and the conversion is straightforward in most cases (see e.g. [\[Sourbron & Buckley, 2013\]](#)).

3.1 Tofts models and the Impulse Response Formalism

The diffusion is driven by a concentration gradient across the membrane, between the vascular and the extravascular, extracellular compartment, with their fractional volumes denoted as v_p and v_e , respectively. Contrast agents don't pass into the intracellular space of the tissue, v_i , which completes the three subvolumes, such that the

¹As pointed out by [Sourbron & Buckley \[2013\]](#) the term *indicator* is more appropriate than *tracer*, to describe substances that are used in DCE-MRI. This is because they are not identical to any system substances. We will nevertheless stick with the convention to speak of *tracer* kinetics.

3. COMPARTMENTAL MODELLING

Symbol	Units	Explanation
K^{trans}	1/min	Volume transfer constant
PS	1/min	Permeability-surface area product
F_p	1/min	Plasma flow
T	min	Mean transit time
E	%	Fraction of CA that is extracted into the EES
v_e	%	rel. extracellular extravascular volume
v_p	%	rel. plasma volume
v_i	%	rel. intracellular volume
c_a	M	tracer concentration in the plasma of the feeding artery (AIF)
c_p	M	average tracer concentration in the plasma space
c_e	M	average tracer concentration in the EES
c_t	M	average tracer concentration in the whole tissue

Table 3.1: Model parameters used throughout this study

Model	Impulse Response Function	Model Assumptions
TM	$e^{-t \frac{EF_p}{v_e}}$	CA instantaneously and well mixed in every compartment. Negligible plasma volume.
ETM	$v_p \delta(t) + e^{-t \frac{EF_p}{v_e}}$	CA instantaneously and well mixed in every compartment.
2CXM	$A_+ e^{-tB_+} + A_- e^{-tB_-}$ see eq. (3.13) – (3.15)	Well mixed plasma compartment and well mixed EES.
ATHM	$F_p; t < T$ $F_p \exp[-\frac{EF_p}{v_e}(t - T)]; t \geq T$	Plasma space is a plug-flow system, EES is well mixed. Exchange at outlet only.
DPM	$F_p; t < T$ see eq. (3.20); $t \geq T$	Plasma space is a plug-flow , EES is distributed (no transport parallel to capillary).

Table 3.2: Overview of PK models, that are used throughout this study.

tissue is subdivided into:

$$v_p + v_e + v_i = 1. \quad (3.1)$$

The three compartments are sketched in Fig. 3.1. The volume transfer constant K^{trans} is the parameter of greatest interest for the tissue characterization. It is the rate at which nutrients are delivered from the plasma space into the extracellular extravascular space (EES) and measured in 1/min. Alternatively K^{trans} can be defined as the product of the plasma flow and the extraction fraction:

$$K^{trans} = EF_p \quad (3.2)$$

3.1 Tofts models and the Impulse Response Formalism

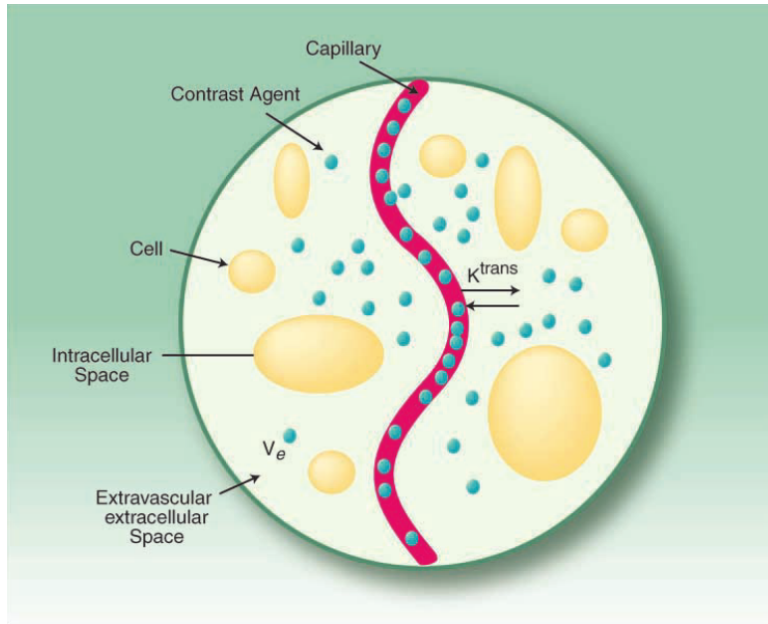


Figure 3.1: Compartmental model of the microvasculature (adopted from Jackson *et al.* [2007])

The simplest rate equation for the distribution of contrast agent, based on the concentration gradient accounting for the CA flow, is given by the CA mass conservation:

$$v_e \cdot \frac{d}{dt} c_e(t) = K^{trans}(c_p(t) - c_e(t)), \quad (3.3)$$

where $c(t)$ describes the CA concentration time course in the respective volume. Eq. (3.3) simply states, that the change in contrast agent concentration in the EES is proportional to the difference in concentration in the VS and the EES, i.e. that the diffusion from the vessel is driven by the concentration gradient. With the additional assumption, that the concentration in the plasma, c_p , equals the concentration at the arterial input throughout the tissue, i.e.

$$c_a(t) = c_p(t) \quad (3.4)$$

the extended Tofts (ETM) model is fully defined.

Eq. (3.3) can be solved analytically for $c_e(t)$ (see appendix A on page 71):

$$c_e(t) = \frac{K^{trans}}{v_e} \int_0^t c_p(t') \exp \left[\frac{-K^{trans} \cdot (t - t')}{v_e} \right] dt' \quad (3.5)$$

3. COMPARTMENTAL MODELLING

The total contrast agent concentration is given by the sum of the contrast agent in the plasma space and in the extracellular extravascular space: $c_t = v_p c_p + v_e c_e$. The integral in eq. (3.5) represents a convolution operation. Thus, with eq. (3.4), it can be written as:

$$c_t(t) = v_p c_a(t) + K^{trans} \int_0^t c_a(t') \exp \left[\frac{-K^{trans} \cdot (t - t')}{v_e} \right] dt' \quad (3.6)$$

$$= c_a(t) * I(t). \quad (3.7)$$

Here $*$ denotes the convolution operation and $I(t)$ is the impulse response function, which fully describes the tissue properties. Its functional form defines the tissues response on a δ -spike input. $c_a(t)$ is the previously mentioned arterial input function (AIF). Eq. (3.6) defines the ETM within the impulse response formalism, with the impulse response function

$$I(t)_{\text{ETM}} = v_p \delta(t) + e^{-t \frac{EF_p}{v_e}}. \quad (3.8)$$

The ETM has been first derived by [Tofts \[1997\]](#) and is widely used in DCE-MRI. One of its major advantages is, that it features only three parameters, and thus allows for estimates of K^{trans} , v_e , and v_p from data with a relatively low temporal resolution. Neglection of the vascular tracer yields the original Tofts model (TM) with its response function [[Tofts et al., 1999](#)]

$$I(t)_{\text{TM}} = e^{-t \frac{EF_p}{v_e}} \quad (3.9)$$

It is mostly used in cases where the data quality does not allow for fitting a model with more parameters, even though the assumption $v_p = 0$ may not be fulfilled. In such cases the resulting K^{trans} and v_e might be strongly biased and have to be interpreted with care. This effect has been described by [Buckley \[2002\]](#) is also apparent in the results of this study, by comparing the parameter estimates from the TM for a negligible v_p and a v_p of 5% with all other parameter being equal, as e.g. in Fig. 6.3 and B.5 (pp. 39 and 78), compared to B.1 and B.9 (pp. 74 and 82).

All discussed models can be written within the introduced formalism (eq. (3.7)) where the arterial input $c_a(t)$ is convolved with a model specific impulse response functions.

3.2 The two-compartment exchange model

3.2 The two-compartment exchange model

The two-compartment exchange model (2CXM) features four free parameters. A major difference to the Tofts models is, that it estimates the blood flow and the permeability surface area separately. The plasma space and the EES are both modelled as well mixed compartments, i.e. they feature a uniform CA concentration. The mass conservation for extravascular compartment then reads:

$$v_e \frac{d}{dt} c_e(t) = PSc_p(t) - PSc_e(t), \quad (3.10)$$

while the dynamic of the concentration in the plasma is given by

$$v_p \frac{d}{dt} c_p(t) = F_p c_a(t) - F_p c_p(t) + PSc_e(t) - PSc_p(t),. \quad (3.11)$$

The solution of this inhomogeneous system of coupled linear differential equations, yields the impulse response function [Sourbron & Buckley, 2011]:

$$I_{\text{2CXM}}(t) = A_+ e^{-tB_+} + F_- e^{-tB_-}, \quad (3.12)$$

with

$$B_{\pm} = \frac{F_p}{(v_p + v_e)\tau_{\pm}}, \quad (3.13)$$

$$A_{\pm} = \pm F_p \frac{\tau_{\pm} - 1}{\tau_+ - \tau_-}, \quad (3.14)$$

$$\tau_{\pm} = \frac{E - E \frac{v_e}{v_p+v_e} + \frac{v_e}{v_p+v_e}}{2E} \left[1 \pm \sqrt{1 - 4 \frac{E \frac{v_e}{v_p+v_e} (1 - E) \left(1 - \frac{v_e}{v_p+v_e}\right)}{\left(E - E \frac{v_e}{v_p+v_e} + \frac{v_e}{v_p+v_e}\right)^2}} \right]. \quad (3.15)$$

The 2CXM has been introduced for DCE-MRI in the breast by Brix *et al.* [2004] and was used in a variety of clinical studies [Donaldson *et al.*, 2010, 2011; Thomassin-Naggara *et al.*, 2010].

3.3 The Tissue Homogeneity Model and its Adiabatic Approximation

In contrast to the 2CXM the tissue homogeneity model (THM) models the plasma space as a plug-flow system, which means that the flow velocity is fixed while the

3. COMPARTMENTAL MODELLING

concentration may vary within the plasma space. It was first introduced by [Johnson & Wilson \[1966\]](#). The name originates from the red blood cells, that work as plugs and force all substances to move with the same velocity. The EES is still assumed to be a well mixed compartment. c_p is now a function of the position in the vascular tube x and of the time t . Dividing the vascular tube into pieces of length Δx , each with a constant CA concentration and taking the limit $\Delta x \rightarrow 0$, yields the conservation of tracer mass for both compartments:

$$v_p \frac{\partial}{\partial t} c_p(x, t) = -F_p L \frac{\partial}{\partial x} c_p(x, t) + PS c_e(x) - PS c_p(x, t), \quad (3.16)$$

$$v_e \frac{d}{dt} c_e(t) = PS (c_p(t) - c_e(t)). \quad (3.17)$$

Here $c_p(t)$ is the average concentration within the vascular tube:

$$c_p(t) = \frac{1}{L} \int_0^L dx c_p(x, t), \quad (3.18)$$

where L is the length of the tube. In order to derive a analytic solution, the tracer exchange is assumed to take place only at the venous outlet or, equivalently, the change in $c_e(t)$ is assumed to be negligible compared to that in $c_p(t)$. This assumption is known as adiabatic approximation to the tissue-homogeneity model (ATHM). It allows for an analytic solution of eq. (3.16) and (3.17) yielding the tissue response function:

$$I_{\text{ATHM}}(t) = \begin{cases} F_p; & t < T \\ EF_p \exp \left[-\frac{EF_p}{v_e} (t - T) \right]; & t \geq T \end{cases}. \quad (3.19)$$

This solution elucidates the separation into a plug-flow vascular phase for times smaller than the mean transit time T and an exchange phase for larger times, which is formally equivalent to a tissue-homogeneity model with negligible plasma volume.

The ATHM has been applied in pre-clinical and clinical DCE-MRI and DCE-CT studies [[Bisdas et al., 2008](#); [Kershaw & Buckley, 2006](#); [Korporaal et al., 2012](#); [Michoux et al., 2008](#); [Naish et al., 2009](#)].

A solution of the full THM is possible in the Laplace domain and described by [Lawrence & Lee \[1998\]](#). It has been applied to DCE-MRI by [Moran & Prato \[2001\]](#), but requires the AIF to be transformed to the Laplace domain. In order for this transformation to converge the AIF has to start and end at zero. The authors suggested to circumvent

this limitation by fitting the AIF with functions, that individually allow for a Laplace transform. In spite of another, more recent, proof of concept by [Garpebring *et al.*, 2009] full TH model is hardly applied in practical situations and therefore not considered in this study.

3.4 Distributed parameter model

[Sangren & Sheppard \[1953\]](#) first introduced the distributed parameter model (DPM) and a more recent derivation can be found in [Larson *et al.* \[1987\]](#) and in the context of DCE-MRI in [Koh *et al.* \[2003\]](#). It has lately been applied in several clinical contexts [[Bisdas *et al.*, 2008](#); [Koh *et al.*, 2011a,b](#)]. In common with the TH model the distributed parameter model (DP) describes the plasma space as a plug-flow system, while the EES is distributed. In order to allow for a simple solution, movement of particles in the EES is restricted by barriers perpendicular to the vessel walls, i.e. there is no motion along the direction of the vessel in the EES. While there is no physiological justification for this assumption it allows for an analytic solution in the time domain and serves as a good approximation to the THM [[Sourbron & Buckley, 2013](#)]. Besides the extravascular concentration c_e being a function of x and t , the equations for the conservation of tracer mass are identical to eqs. (3.16) and (3.17) for the ATHM and yield a similar solution:

$$I_{\text{DP}} = \begin{cases} F_p; & t < T \\ EF_p \left[1 + \int_0^T d\tau \exp \left[-\frac{PS}{v_e} \tau \right] \sqrt{\frac{PS^2}{Fv_e \tau}} J_1 \left(2\sqrt{\frac{PS^2 \tau}{Fv_e}} \right) \right]; & t \geq T \end{cases} \quad (3.20)$$

Here J denotes the Bessel function of first kind.

3.5 Further Models

In some cases, especially in early stages after the CA arrival, the backflow of CA from the EES to the VS can be neglected. This assumption gives rise to a class of models known as *tissue-uptake models*. They are not suitable for the simulated observation times, used in this study. Likewise, PK models with only one parameter (one-region uptake model, steady-state model) are not able to describe the data at hand.

A comprehensive description of these models is given by [Sourbron & Buckley \[2013\]](#).

3. COMPARTMENTAL MODELLING

4

Simulation of Contrast Agent Input and Uptake

4.1 AIFs for Arbitrary Injection Rates

In order to generate typical AIFs for a variety of injection rates, two procedures were employed. The first procedure follows [Aerts *et al.* \[2008\]](#) and derives the AIF by convolution of the concentration time curve of the CA injection with a transfer function, whose parameters are phenomenologically derived by fitting to a known injection shape and a measured AIF. The second approach, described in more detail in the next paragraph, models the AIF as linear upslope followed by a single exponential decay (eq. (4.1)). This allows for a simple analytic expression, which is fully defined by four parameters and thus facilitates systematic changes in the functional form of the AIF. For both cases, possible recirculation bumps are neglected. The derived curves are normalized to their peak concentration, as the absolute value of the concentration is not of importance for any of the following analysis. AIFs from both procedures have been used to carry out simulations and no significant differences between the two approaches was found. All results in this work are therefore merely based on the simpler analytic approach.

The broad characteristics of the concentration time course of a typical AIF can be described by a linear slope (α) during the bolus injection (with duration τ) and an ensuing exponential decay (decay constant: β) towards a steady-state concentration

4. SIMULATION OF CONTRAST AGENT INPUT AND UPTAKE

c_f :

$$AIF(\alpha, \beta, \tau, c_f; t) = \underbrace{\Theta(\tau - t) \alpha t}_{\text{Linear upslope}} + \underbrace{\Theta(t - \tau) \left[(\alpha\tau - c_f)e^{-\beta(t-\tau)} + c_f \right]}_{\text{Exponential decay}}. \quad (4.1)$$

This form allows for modification of the injection rate with a constant injection volume: Under variation of the injection rate the slope α and the duration of the injection phase τ change, while the amount of CA, that passes the tissue of interest during the injection phase is kept constant, i.e. the area under the upslope A_{up} is constant. As the total amount of CA is constant, the area under the decay phase A_{decay} is constant, too. Analytic expressions for both these areas are:

$$A_{up} = 1/2 \alpha \tau^2, \quad (4.2)$$

$$A_{decay} = c_f(t_f - \tau) + \frac{\alpha\tau - c_f}{\beta}, \quad (4.3)$$

where t_f is the final point in time of the observation. Parameters α , β , τ , c_f , and t_f are derived from fitting eq. (4.1) to measured AIFs. Keeping the consequent values for A_{up} and A_{decay} constant, yields the following conditions for variation of α :

$$\tau = \sqrt{\frac{2A_{up}}{\alpha}}, \quad (4.4)$$

$$\beta = \frac{\alpha\tau - c_f}{A_{decay} - c_f(t_f - \tau)}. \quad (4.5)$$

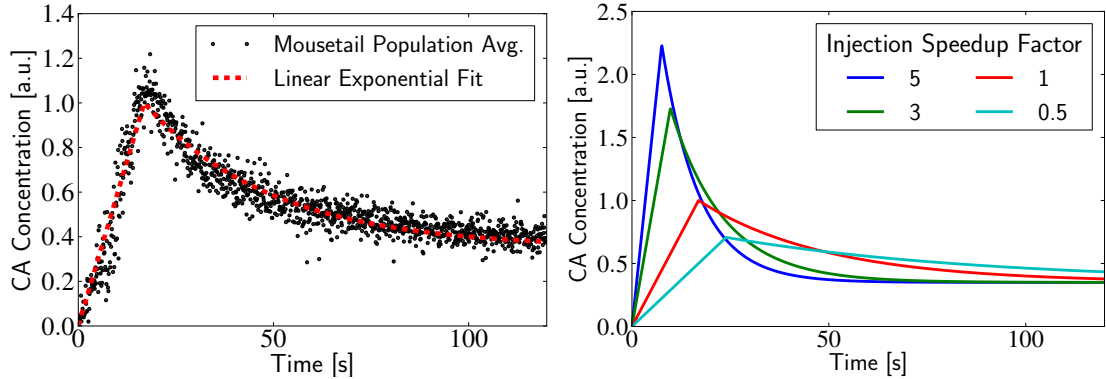
Holding the observation time t_f and the final concentration c_f constant, leaves the upslope α (and therewith the injection rate) as the only free parameter.

This procedure is carried out for a population averaged AIF from measurements in mouse tails, featuring a high temporal resolution of 100 ms [Moroz *et al.*, 2013] and for a human AIF, where the analytic approximation for a population average from Parker *et al.* [2006] is used. The recirculation bump that was reported is replaced by a linear decay. Fits of the model to both AIFs and examples for the modified injection rates are given in Fig. 4.1.

The modification of the slope is parametrized by an *injection speedup* factor:

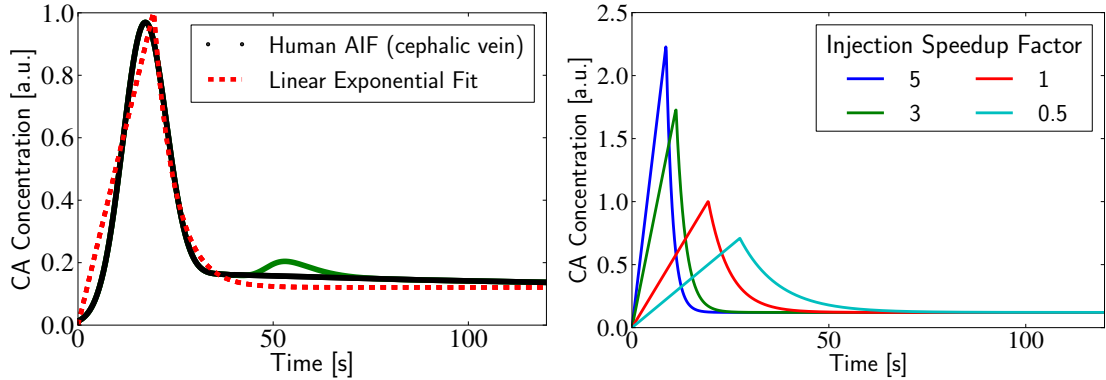
$$\alpha \rightarrow \text{inj. speedup} \cdot \alpha \quad (4.6)$$

4.1 AIFs for Arbitrary Injection Rates



(a) Fit to mouse tail population average with a sampling interval of 100 ms, as reported by Moroz *et al.* [2013] (Rate: 1 ml/min).

(b) Derived AIFs for different injection speedup factors. The red curve corresponds to the fit in Fig. a.



(c) Fit to the analytic approximation of human AIF from injections in the antecubital vein as reported by Parker *et al.* [2006]. (Rate: 3 ml/s) The recirculation bump (green) has been removed for the analysis.

(d) Derived AIFs for different injection speedup factors. The red curve corresponds to the fit in Fig. c.

Figure 4.1: Procedure to create AIFs from a mouse population average (a and b), as well as from an analytic approximation of a human AIF (c and d), by making use of eq. (4.1). The linear slope plus exponential decay equation is fitted to population average AIFs, that were reported in literature and subsequently the upslope is varied according to eq. (4.6).

4. SIMULATION OF CONTRAST AGENT INPUT AND UPTAKE

4.2 Tissue Uptake Simulation with MMID4

Simulation studies of DCE-MRI often employ PK models to simulate the uptake curves, which are then analyzed with similar models or even with the same models (E.g. Kershaw & Buckley [2006]; Luypaert *et al.* [2011, 2012]). The results of such studies have to be interpreted carefully, as it is a matter of fact, that physiological uptake is far more complicated than any of these models. Therefore errors and biases of such studies are likely to originate from the data simulation, rather than the model fitting.

A model that is distinctively closer to physiology is chosen for this study. Based on the AIFs that were described in section 4.1 tissue uptake curves are simulated using the Multiple path, Multiple tracer, Indicator Dilution, 4 region model (MMID4)¹. This model is described in detail by Kroll *et al.* [1996]. It simulates blood tissue exchange and accounts for flow dispersion and heterogeneity. The simulation procedure is adopted from a study by Buckley [2002]. From the large number of parameters that are variable within the MMID4, only the mean plasma flow (F_p), the permeability surface area (PS), the plasma volume and the interstitial volume (v_p, v_e) are modified. Non-exchanging vessels are neglected and the flow heterogeneity is modelled by apportioning the flow across 20 pathways using a lagged normal density distribution. A tissue density of 1 g/ml is assumed. The tracer uptake is modelled by convolution of the incoming concentration with a transport function for each vessel, while the input concentration is uniformly distributed throughout the flow pathways. This allows to calculate the volume transfer constant as it is derived in Sourbron & Buckley [2013]:

$$K^{trans} = \frac{F_p PS}{F_p + PS}. \quad (4.7)$$

In order to asses the whole range of relevant parameters tissue uptake curves were simulated for eight different parameter combinations. All combinations of the following parameter values were considered:

$$F_p[\text{ml/g/min}] = .5, 1.2; \quad (4.8)$$

$$PS[\text{ml/g/min}] = .2, .6; \quad (4.9)$$

$$v_e[\%] = 40; \quad (4.10)$$

$$v_p[\%] = 0.1, .5 \quad (4.11)$$

A certain combination of these parameters will be referred to as *parameter setup*

¹<http://physiome.org/jsim/models/webmodel/NSR/MMID4/>

4.3 Systematic AIF Mismeasurements

throughout this study. The simulated concentration curves for two injection rates are shown in Fig. 4.2. The total acquisition time of 270 s and the sampling interval of 2.5 s is held constant, throughout.

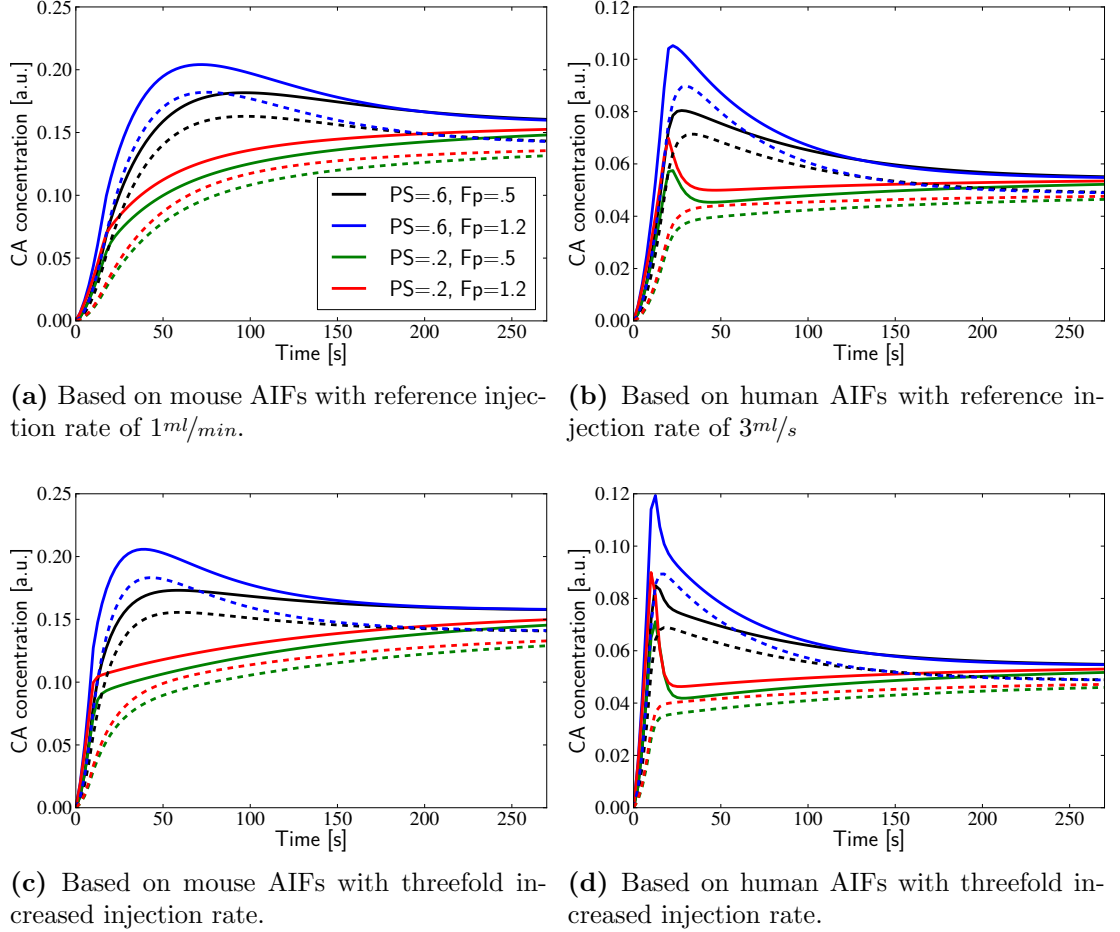


Figure 4.2: Concentration time curves based on the AIFs from Fig. 4.1 and simulated with the MMID4. Solid Line: $v_p = .05$; Dashed line: $v_p = .001$. The lower row shows the uptake for increased injection rates.

4.3 Systematic AIF Mismeasurements

In order to assess the effect of a lack of knowledge or a mismeasurement of the AIF, its functional form is systematically modified in five different ways to emulate such errors.

1. The bolus arrival time (BAT) is varied by means of an additive parameter Δt (sect. 4.3.1).

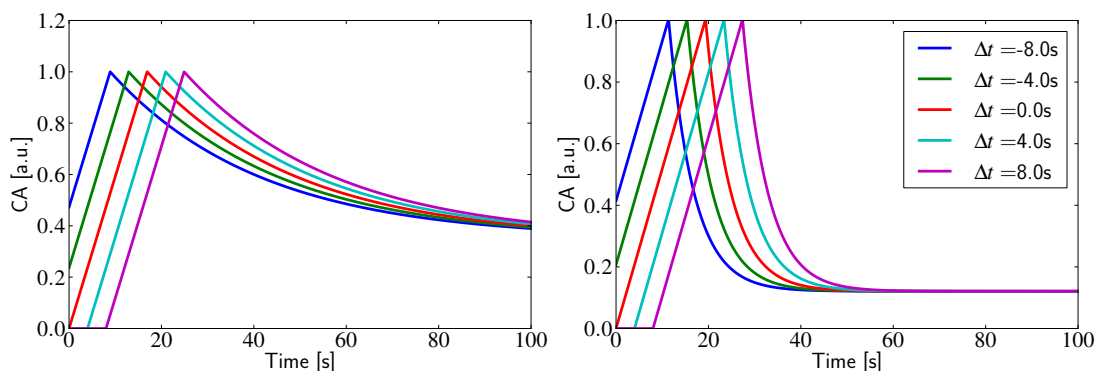
4. SIMULATION OF CONTRAST AGENT INPUT AND UPTAKE

2. The injection rate is varied as it was discussed in section 4.1, quantified as a relative error ϵ_r , such that $\tilde{\alpha} = \alpha(1 + \epsilon_r)$. This reflects the realistic scenario of a manual injection, where the rate is particularly error prone.
3. The haematocrit is varied as discussed in sect. 4.3.2.
4. The horizontal peak position is varied, while keeping the vertical position and the total area under the AIF constant. (sect. 4.3.3).
5. The peak AIF concentration is varied, while keeping the horizontal position and the total area under the AIF constant. (sect. 4.3.3).

The effect of using a *wrong* AIF for fitting a concentration time course is assessed separately for all four methods, the results are discussed in section 6.2 on p. 43.

4.3.1 Error in the Bolus Arrival Time

An important uncertainty in the analysis of DCE-MRI is the bolus arrival time in the tissue of interest [Henderson *et al.*, 1998; Meyer, 1989; Singh *et al.*, 2009]. For that reason it has been suggested to be a free model parameter [Lawrence & Lee, 1998; Meyer, 1989], but this approach is hardly used in practice. The BAT's effect on the AIF is straightforward as shown in Fig. 4.3.



(a) Error in the bolus arrival time for a mouse (b) Error in the bolus arrival time for a human
AIF.

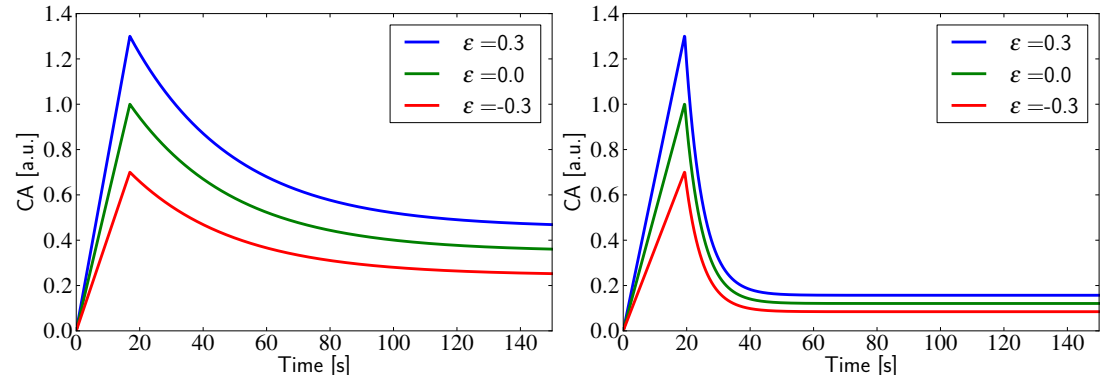
Figure 4.3: Error in the bolus arrival time correspond to a shift of the AIF along the time axis.

4.3.2 Error in the haematocrit

It has been pointed out by Parker *et al.* [2006, chap. 6, sect. 6], that the haematocrit (HCT) is one of the major sources of error in a DCE-MRI experiment. Contrast agents only occupy the plasma volume of the blood, and thus the determination of an AIF needs a conversion from the measured concentration in the whole blood to the concentration in the plasma. Most studies assume a fractional value of 0.4 and refrain from individual measurements, even though it is known that there is a significant variation between vessels of different sizes, known as the Fahraeus effect [Barbee & Cokelet, 1971; Gaehtgens, 1980]. Furthermore, there is a inter and intrapatient variation, which holds especially true for patients with advanced cancer [Just *et al.*, 2011; Roberts *et al.*, 2011]. An underestimation of the haematocrit yields an overestimation of the AIF by a scaling factor ϵ_{HCT} , such that:

$$A\tilde{F}(t) = AIF(t)(1 + \epsilon_{HCT}). \quad (4.12)$$

where positive ϵ_{HCT} correspond to an underestimation of the haematocrit. Examples of the resulting AIFs shown in Fig. 4.4.



(a) Error in the haematocrit for a mouse AIF. (b) Error in the haematocrit for a human AIF.

Figure 4.4: A misestimation of the haematocrit causes a scaling of the AIF.

4.3.3 Error in the Peak Position

The vertical and horizontal peak position, which correspond to the peak concentration and the time of maximum concentration, are two distinct features of an AIF. Both can be modified systematically, based on the simple model that was described in section 4.1

4. SIMULATION OF CONTRAST AGENT INPUT AND UPTAKE

on page 19. Equations (4.4), and (4.5) are still valid, i.e. the total volume and the final concentration are kept constant. Again, a single parameter without units, ϵ , controls the magnitude of the relative error in the horizontal and peak AIF concentration. Modified parameters are denoted with a tilde.

The horizontal peak position is parametrized by τ and thus modified according to

$$\tilde{\tau} = \tau(1 + \epsilon_h). \quad (4.13)$$

While the vertical position, given by the product of the upslope and the duration of the upslope phase $\alpha\tau$, is kept constant. Together with eq. (4.4) this yields the two conditions:

$$\tilde{A}_{up} = 1/2 \alpha\tau \cdot \tilde{\tau}, \quad (4.14)$$

$$\tilde{\alpha} = \frac{\alpha\tau}{\tilde{\tau}}. \quad (4.15)$$

Here, an error of $\epsilon_h = -1$ corresponds to an infinite initial upslope.

The peak AIF concentration is controlled by the product $\alpha\tau$. Its error is parametrized by ϵ_v , such that $\epsilon_v = -1$ corresponds to a peak concentration equal to that observed at the final observation time, c_f , and $\epsilon_v = 1$ to an overestimation of the peak by the same amount.:

$$\tilde{\alpha} = \alpha(1 + \epsilon_v) - \frac{\epsilon_v c_f}{\tau}. \quad (4.16)$$

The horizontal position is kept constant, i.e. $\tilde{\tau} = \tau$. This yields

$$\tilde{\alpha}\tilde{\tau} - c_f = (\alpha\tau - c_f)(1 + \epsilon_v), \quad (4.17)$$

$$\tilde{\alpha} = \alpha\tau(1 + \epsilon_v) - \frac{\epsilon_v c_f}{\tau}. \quad (4.18)$$

The total volume is still conserved ((4.4), (4.5)).

The effect of both modifications on the consequent AIFs is shown in Fig. 4.5 for both, the mouse and the human case.

4.3 Systematic AIF Mismeasurements

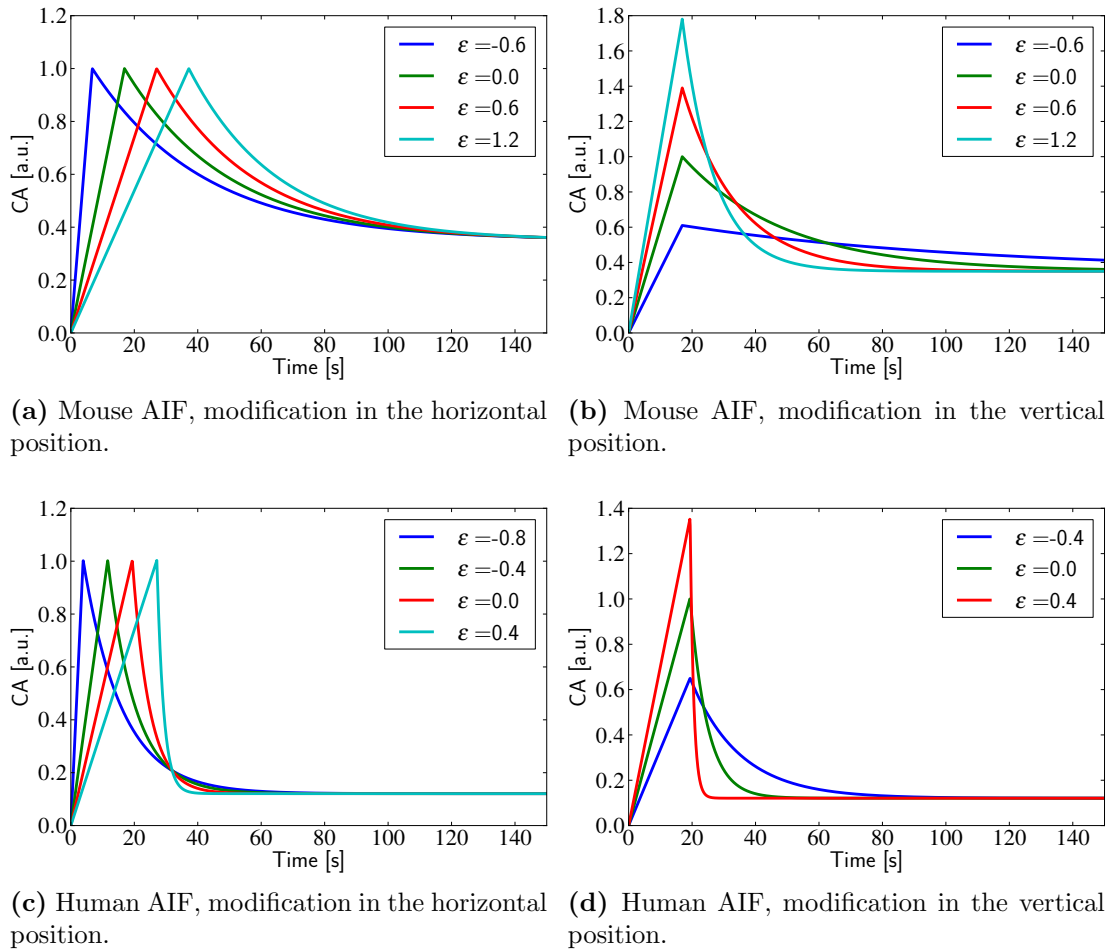


Figure 4.5: The parameter ϵ shifts the peak horizontal or vertical relative to the true value. The total injected volume (area under the AIF) and the final concentration are preserved.

4. SIMULATION OF CONTRAST AGENT INPUT AND UPTAKE

5

Data Fitting and Estimation the Sampling Distribution

5.1 Parametric Bootstrap

In order to assess the statistical distribution of parameter estimates from the different models, a parametric bootstrap procedure is employed. Bootstrapping is a resampling method to estimate the sampling distribution of a random variable. It was first introduced by [Efron \[1979\]](#) and is thoroughly explained by [Singh & Xie \[2009\]](#).

The general idea of bootstrapping is, to treat a sample, which is drawn from a population as a surrogate population and resample the data with replacement from this sample. The so achieved samples are called bootstrap samples. An arbitrary number of bootstrap samples can be drawn from the surrogate population, which then allows for the estimation of the statistical distribution of any property within the surrogate population. For larger samples the property of the surrogate population converges towards the property of the full population. The method employed in this study is called *parametric bootstrap*. A model is fitted to data, and random samples are drawn from the model prediction by adding different realizations of random noise. The current study uses noise free data from a physiological model (see section 4.2), such that bootstrap samples can be drawn by adding different realizations of Gaussian random noise with a certain SNR, as it would be observed in an actual measurement.

The whole procedure, including simulation of the data, is summarized in the following recipe.

1. Generate AIFs for arbitrary injection rates (sect. 4.1).

5. DATA FITTING AND ESTIMATION THE SAMPLING DISTRIBUTION

2. Generate tissue uptake curves $c_t(t)$ for each AIF using the MMID4 (sect. 4.2).
3. Add noise to $c_t(t)$ (sect. 5.2).
 - (a) Convert $c_t(t)$ to MR signal. (eq. (2.6) and eq. (2.8)).
 - (b) Add Gaussian noise with certain SNR. (SNR = 30, or mentioned otherwise)
 - (c) Transform back to (noisy) $c_t(t)$.
4. Fit PK models (TM, ETM, 2CXM, ATHM, DPM) with a certain AIF true (or deficient) to the noisy data.
5. Iterate steps 3 and 4 one thousand times to derive a distribution for the fit parameters.

The investigation of the effect of different injection rates (sect. 6.1) precisely follows this procedure. For studying the effect of deficient AIFs, different SNRs and information criteria weighted estimates (sect. 6.2, 6.3, 6.4), only the reference AIF is considered for simulating $c_t(t)$ in step 2.

5.2 Simulating Noise

For a FLASH experiment the, transverse magnetization (proportional to the signal) is given by eq. (2.6) which was derived on p. 7. It is a function of the repetition time TR, the baseline spin-lattice relaxation time $T_{1,0}$ and the time dependent spin-lattice relaxation time after injection of the contrast agent.

To add a realistic measurement noise to the concentration time course $c_t(t)$, it is converted to a signal before the noise is added. Eventually, the noisy signal curve is converted back to a (noisy) concentration. The conversion is done according to the signal equation (2.6) and the inverse relations:

$$E = \frac{M_T^{SS}/M - \sin(\alpha)}{M_T^{SS}/M \cos(\alpha) - \sin(\alpha)}, \quad T_1 = \frac{-TR}{\ln(E)}, \quad c_t = \frac{1}{r} \left(\frac{1}{T_1} - \frac{1}{T_{1,0}} \right). \quad (5.1)$$

Typical values are assumed for the conversion:

$$r = 5.99 \text{ mM}^{-1}\text{s}^{-1}, \quad \text{TR} = 100 \text{ ms}, \quad T_{1,0} = 2000 \text{ ms}, \quad \alpha = 25^\circ. \quad (5.2)$$

5.3 Fitting Algorithm and Initial Parameters

The relaxivity value r is taken from [Caravan *et al.* \[2009\]](#) for a Gadolinium based contrast agent at a main magnetic field of 4.7 T. The SNR is defined as

$$\text{SNR} = \frac{\langle \text{Signal}(t) \rangle}{\text{Noise Amplitude}}. \quad (5.3)$$

5.3 Fitting Algorithm and Initial Parameters

Fit parameters were limited to be positive and fractional volumes to be smaller than one. The bootstrap iteration was discarded, if no minimum was found after 200.000 function calls or if the coefficient of determination (R^2) of the final guess was negative. The models' objective functions are generally not convex and it is therefore important to have good knowledge of the initial guesses or a reliable global minimization algorithm. In this study the `scipy.leastsq` search algorithm¹, based on a modified Levenberg-Marquardt algorithm [Levenberg \[1944\]](#), is used. Initial parameters are derived by performing brute force fitting for every parameter setup with the noise free data. In order to resemble a realistic scenario, where investigators lack knowledge of the best initial parameters, they were then randomly sampled from a uniform distribution with a width of $\pm 25\%$ around the actual best (brute force) guess. Trials with a larger sampling interval led to increased numbers of fits that had to be discarded by the abovementioned criteria, while the distributions of haemodynamic parameters were not significantly affected.

5.4 AIC and BIC weighted Parameter Estimates

This section gives a heuristic introduction to model weighting based on the Akaike information criterion (AIC) and the Bayesian information criterion (BIC). While merely the most important results are given explicitly, the interested reader may be referred to the more detailed literature. An instructive introduction to Akaike's original derivation can be found in [Leeuw \[1992\]](#) and a unified derivation of AIC and AIC_c is given by [Cavanaugh \[1997\]](#).

AIC [Kullback & Leibler \[1951\]](#) derived a measure for the loss of information if a probability distribution P is approximated by a probability distribution Q . For the purpose at hand P is thought of as the *true* distribution of the data, while Q is a

¹<http://docs.scipy.org/doc/scipy/reference/generated/scipy.optimize.leastsq.html>

5. DATA FITTING AND ESTIMATION THE SAMPLING DISTRIBUTION

model, that approximates P . If denoting the corresponding probability densities with p and q their result reads:

$$I(p, q) = \int dx f(x) \log \left(\frac{p(x)}{q(x)} \right). \quad (5.4)$$

[Akaike \[1974a,b\]](#) derived a connection between the Kulback-Leibler information and the maximized likelihood and hence a model selection criterion, which is known as Akaike information criterion:

$$\text{AIC} = -2 \ln[\mathcal{L}(\hat{\Theta}|\text{data})] + 2K, \quad (5.5)$$

where $\hat{\Theta}$ is the maximum likelihood estimate of the model parameters, and K is the number of parameters.

For least squares fitting with normal distributed errors the likelihood can be written explicitly, such that it follows:

$$\text{AIC} = n \ln \left(\frac{\text{RSS}}{n} \right) + 2K, \quad (5.6)$$

where n is the number of data points and RSS is the sum of the squared residuals of the fitted model. Intuitively, the AIC weighs the residuals of a model against number of model parameters. [Sugiura \[1978\]](#) derived a correction for small samples sizes, which is applied throughout this study and known as AIC_C :

$$\text{AIC}_c = -2 \ln[\mathcal{L}(\hat{\Theta}|\text{data})] + 2K + \frac{2K(K+1)}{n-K-1}. \quad (5.7)$$

In order to compare different models by means of their AIC score the AIC needs to be rescaled. A procedure is suggested by [\[Burnham, 2004\]](#). It suggests a rescaling which assigns a value of zero to the best model

$$\Delta_i = \text{AIC}_i - \text{AIC}_{min}, \quad (5.8)$$

where all candidate models are indexed by i . Subsequently the normalized likelihood for every model yields the so called Akaike weights:

$$w_i = \frac{\exp(\Delta_i/2)}{\sum_r \exp(-\Delta_r/2)}. \quad (5.9)$$

These weights can be thought of as the probability that the model i is the best model

5.4 AIC and BIC weighted Parameter Estimates

of the set of evaluated models, where the goodness is defined in terms of Kullback-Leibler-Information.

BIC The original derivation of the BIC was given by [Schwarz \[1978\]](#). A more general, insightful approach was chosen by [Cavanaugh & Neath \[1999\]](#). The BIC originates from a formal Bayesian argument, that the preferred model is that with the largest *marginal density* m .

$$m = \int \mathcal{L}(\Theta) \pi(\Theta) d\Theta , \quad (5.10)$$

Here \mathcal{L} is again the likelihood function and π is the prior density. Under certain assumptions, that are unproblematic for most practical cases, $\ln(m)$ is approximated by the BIC.

$$\text{BIC} = -2 \ln[\mathcal{L}(\hat{\Theta}|\text{data})] + K \ln(n) , \quad (5.11)$$

(compare eq. (5.6) for the AIC)

The model weights are calculated similarly to the the procedure, that was introduced for the AIC criterion (eq. (5.8), (5.9)). Compared to the AIC, the BIC prefers more parsimonious models, i.e. it penalizes the number of model parameters stronger. A thorough discussion of the BIC in the context of model selection is given by [Burnham \[2004\]](#).

**5. DATA FITTING AND ESTIMATION THE SAMPLING
DISTRIBUTION**

6

Accuracy and Precision of Haemodynamic Parameters

The main results of the study at hand are presented in this chapter. In order to depict the distributions of haemodynamic parameters, in particular their accuracy and precision, box-and-whisker plots are employed. Fig. 6.1 illustrates this notation.

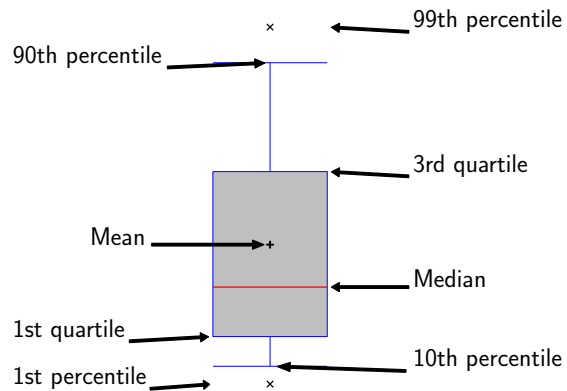


Figure 6.1: Boxplots notation as is used to describe the parameter distributions throughout this chapter.

Section 6.1 reveals the influence of variations in the injection speed on the parameter estimates. Hereafter, section 6.2 shows the influence of a deficient AIF and section 6.3 points out the influence of the SNR. Lastly, the distributions of AIC and BIC weighted parameter estimates are presented in section 6.4

6. ACCURACY AND PRECISION OF HAEMODYNAMIC PARAMETERS

6.1 Variation of the Injection Speed

Bootstrap distributions for K^{trans} , v_e , v_p , E , and F_p for the different models, parameter setups and AIFs are presented in figures as indicated in Tab. 6.1.

	Mouse AIF, $v_p = .5$	Mouse AIF, $v_p = .001$	Human AIF, $v_p = .05$	Human AIF, $v_p = .001$
K^{trans}	Fig. 6.3, p. 39	Fig. B.1, p. 74	Fig. B.5, p. 78	Fig. B.9, p. 82
v_e	Fig. 6.4, p. 39	Fig. B.2, p. 75	Fig. B.6, p. 79	Fig. B.10, p. 83
v_p	Fig. 6.5, p. 39	Fig. B.3, p. 76	Fig. B.7, p. 80	Fig. B.11, p. 84
F_p, E	Fig. 6.6, p. 42	Fig. B.4, p. 77	Fig. B.8, p. 81	Fig. B.12, p. 85

Table 6.1: Bootstrap results and their location in this chapter or in the appendix.

The mean effect of a variation in the injection rate on the precision in K^{trans} – averaged of eight parameter setups – is depicted in Fig. 6.2, which summarizes the primary qualitative result regarding the parameter precision under variation of the injection rate: There is no clear dependence on the injection rate for TM, ATHM, and DPM, while fast injections yield an increase in precision for the ETM and the 2CXM. Precision and accuracy are discussed separately the following.

Parameter Precision For most parameter setups no significant dependence between the injection speed and the precision has been observed within the TM, ATHM and DPM. For the ETM and the 2CXM parameter precision increases for faster injections for most parameter setups. The 2CXM features the most consistent sensitivity to the injection speed. The maximum of this increase is observed for mouse AIFs with a significant vascular volume ($v_p = 0.5$) and a high permeability-surface areas ($PS = 0.6 \text{ min}^{-1}$, see Fig. 6.3 for K^{trans} or Fig. 6.6 on pp. 39 and 42 for E and F_p). However, measured by the interquartile range (IQR) of the distribution even the most extreme case does not yield more than a 30% gain in precision for a doubling of the injection speed, while in half of the cases the gain in precision is smaller than 10%. E.g. for the human AIFs, a gain in precision is almost absent and clearly irrelevant for practical considerations (in particular for a negligible vascular volume, shown in Fig. B.9, p. 82). The highest gain in precision is observed in the regime of the reference injection speed, which corresponds to the regime of practical interest. This holds true for all parameters of interest. Opposed to the TM, whose precision is almost constant, the precision in the four-parameter plug-flow models ATHM and DPM is fluctuating under variation of the injection speed. The loss in precision for the four parameter models, compared

6.1 Variation of the Injection Speed

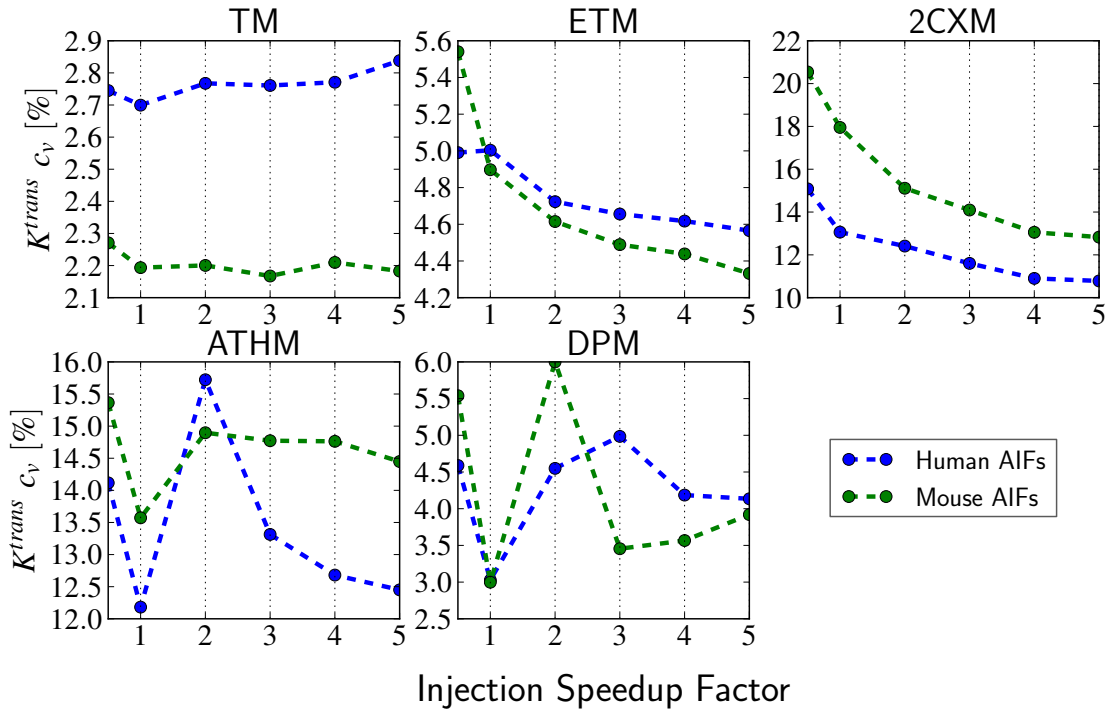


Figure 6.2: Precision (quantified by the coefficient of variation, c_v) as a function of injection rate for mouse and human AIFs for a SNR of 30. Shown is an average over the eight parameter setups, as described on page 22.

to the ETM, ranges between a factor of one and five (measured by the IQR). Only the DPM consistently features a comparably high precision and its interquartile range doesn't surpass that of the ETM by more than a factor of 2.

For the case of a significant vascular volume and a small permeability surface area ($v_p = .05$, $PS = .2$, as e.g. in the lower rows in Fig. 6.3, p. 39) the 2CXM features a precision as high as that of the ETM, while it is significantly lower for other cases.

The results for the ETM comply with the observations from [Aerts et al. \[2008\]](#), who investigated data that was simulated and fitted with the ETM under a variation of K^{trans} , while the other parameters were fixed.

Naturally, the precision decreases for a higher dimensional model space. According to that, the gain in precision between the TM and the ETM (measured by the IQR) is up to a factor of two for some parameter setups. Especially for setups with a significant vascular volume this gain is notably smaller, often close to unity. This is reasonable, because the ETM accounts for the larger influence of the vascular volume, which is neglected by the TM. Despite the similar IQRs the ETM features a significantly wider

6. ACCURACY AND PRECISION OF HAEMODYNAMIC PARAMETERS

range of outliers in K^{trans} and v_e (see Fig. B.1 and B.3, pp. 74 and 76) for mouse AIFs. However, for human AIFs with significant vascular volume no loss in precision of the ETM is observed, at all (see Fig. B.5 and B.6, pp. 78 and 79).

Parameter Accuracy None of the models features a consistent bias in the parameter accuracy under change of the injection speed. The Tofts and extended Tofts model accuracy is not depend at all, while the 2CXM shows a small, but inconsistent change for low injection rates. As its precision, the ATHM and DPM accuracy change with the injection rate. However, this dependence exhibits no trend and appears to be rather random.

A detailed discussion of the parameter accuracy for the different models apart from its dependency on the injection rate is given within the scope of AIC/BIC weighted parameter estimates in section 6.4.

6.1 Variation of the Injection Speed

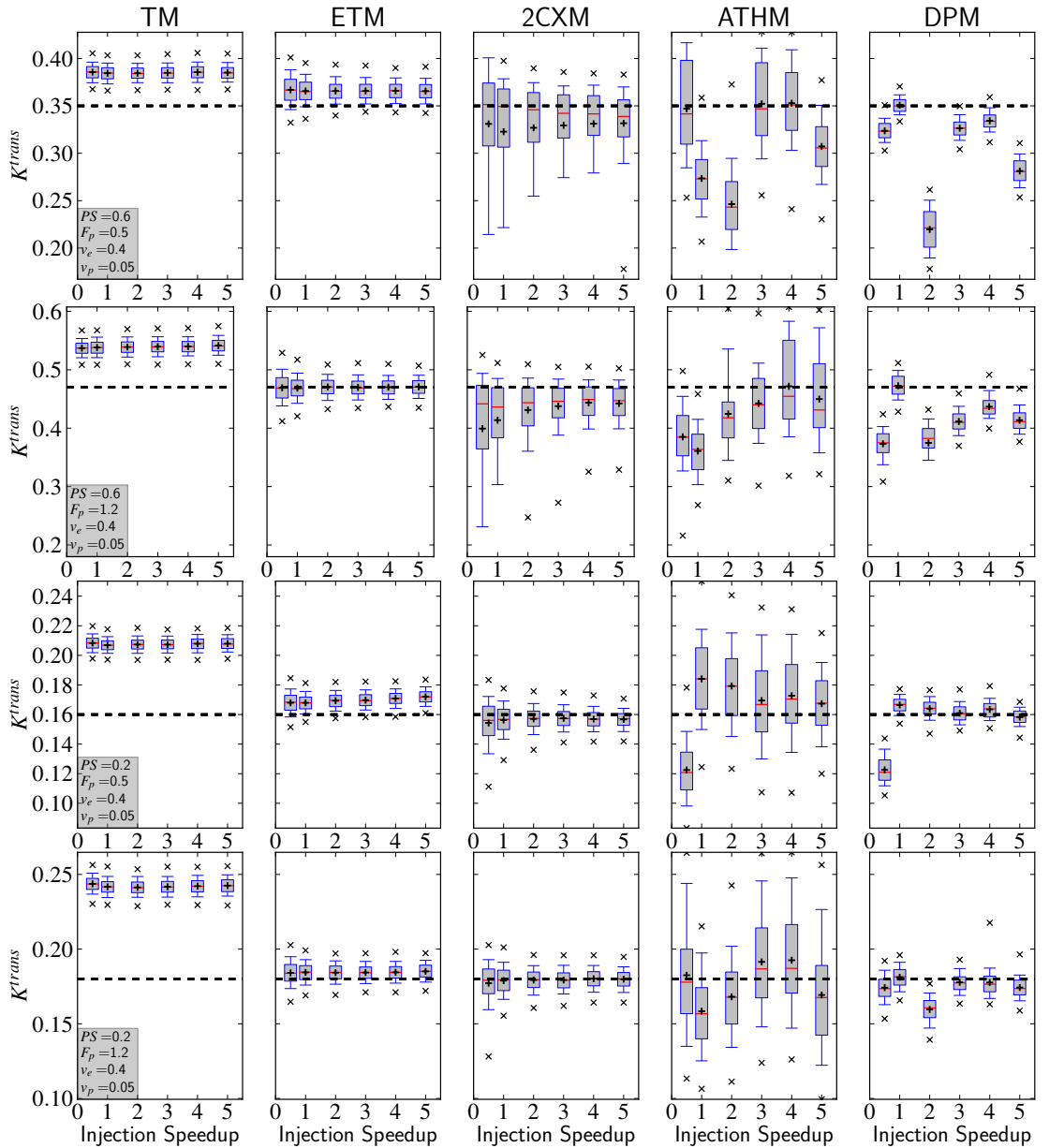


Figure 6.3: Dependence of the accuracy and precision of K^{trans} estimates from five different PK models on the injection speed for an AIF in a mouse tail with a significant vascular volume.

6. ACCURACY AND PRECISION OF HAEMODYNAMIC PARAMETERS

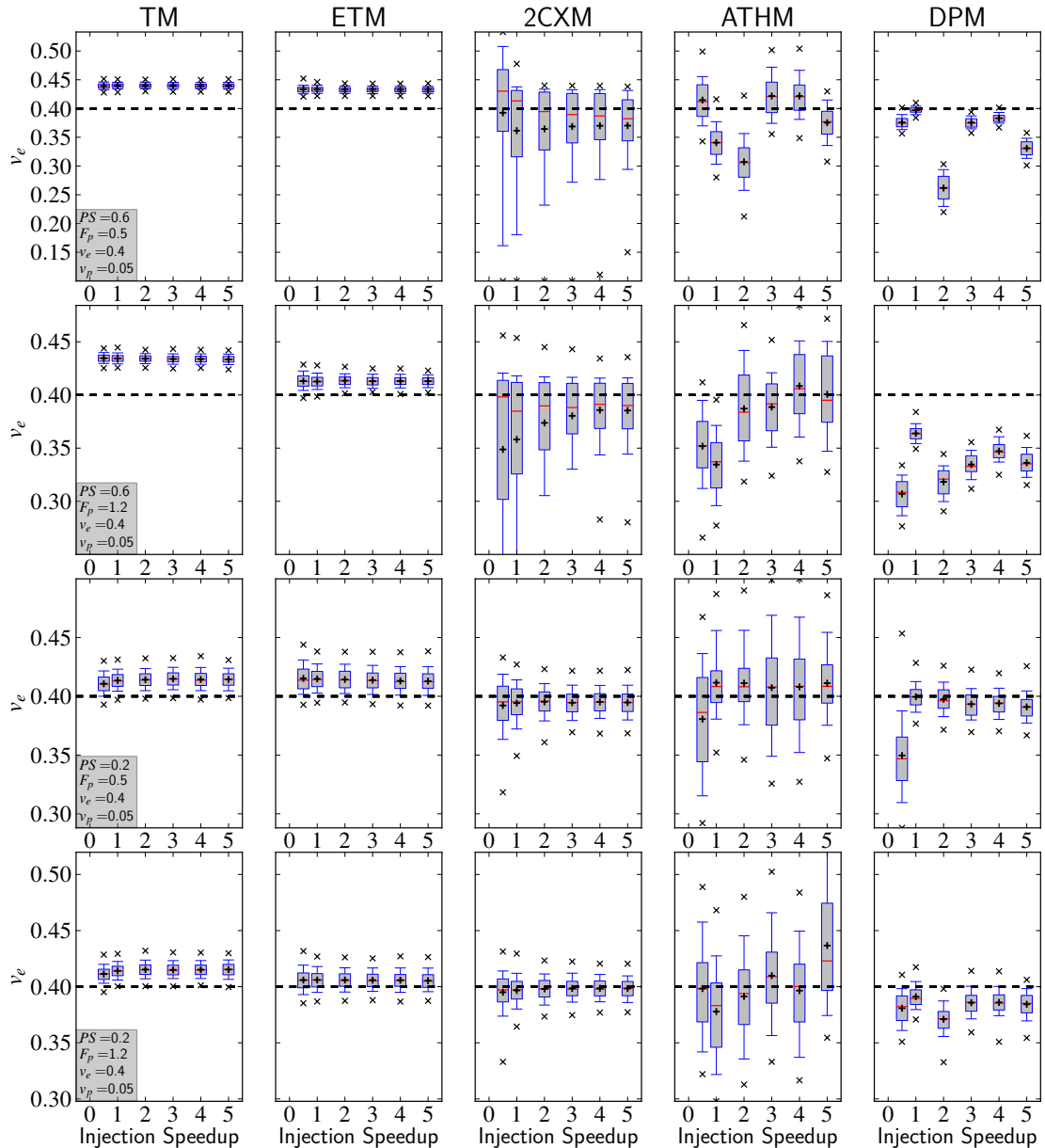


Figure 6.4: Dependence of the accuracy and precision of v_e estimates from five different PK models on the injection speed for an AIF in a mouse tail with a significant vascular volume (SNR = 30).

6.1 Variation of the Injection Speed

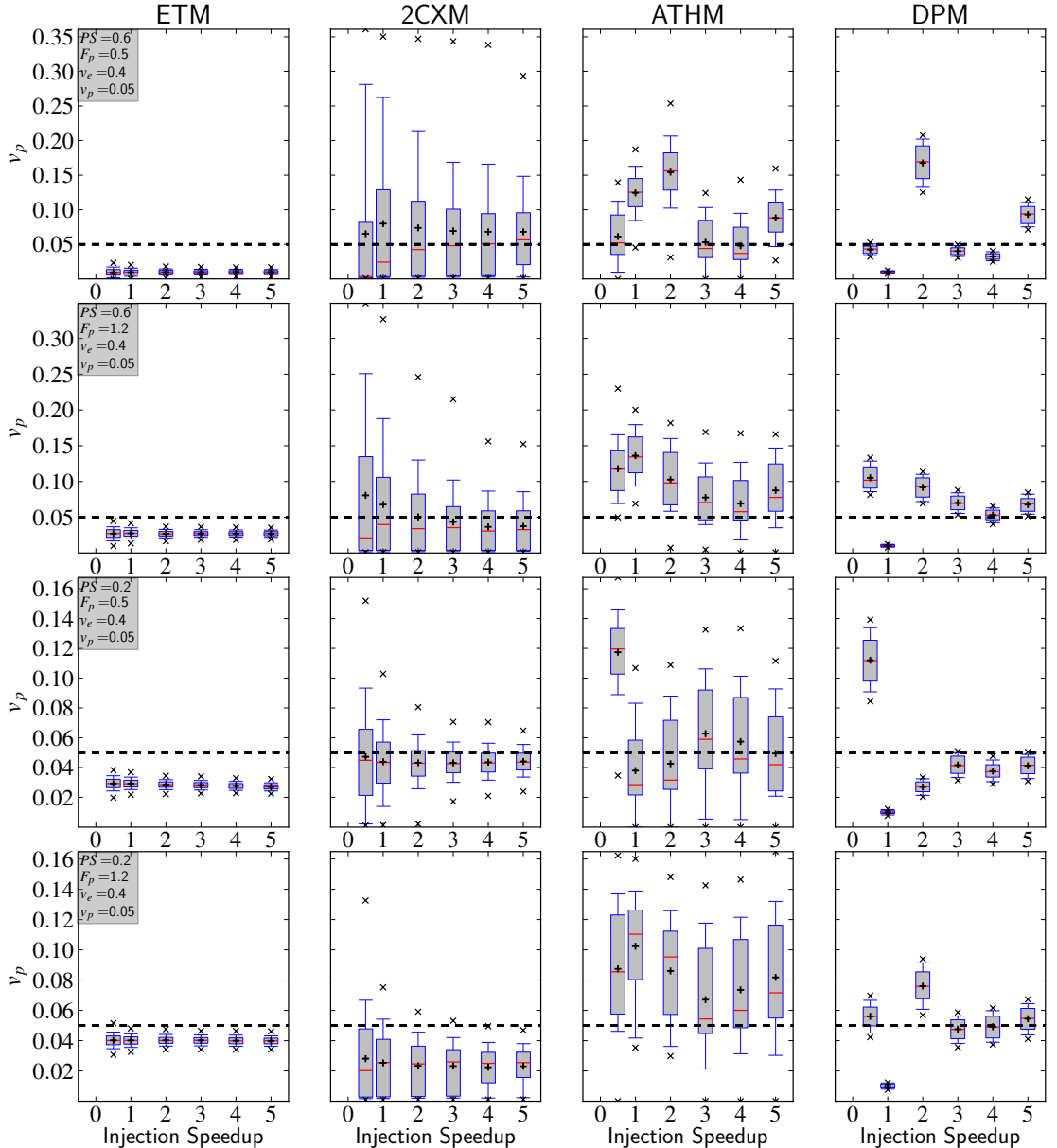


Figure 6.5: Dependence of the accuracy and precision of v_p estimates from five different PK models on the injection speed for an AIF in a mouse tail with a significant vascular volume (SNR = 30).

6. ACCURACY AND PRECISION OF HAEMODYNAMIC PARAMETERS

Blood Flow and Extraction Fraction

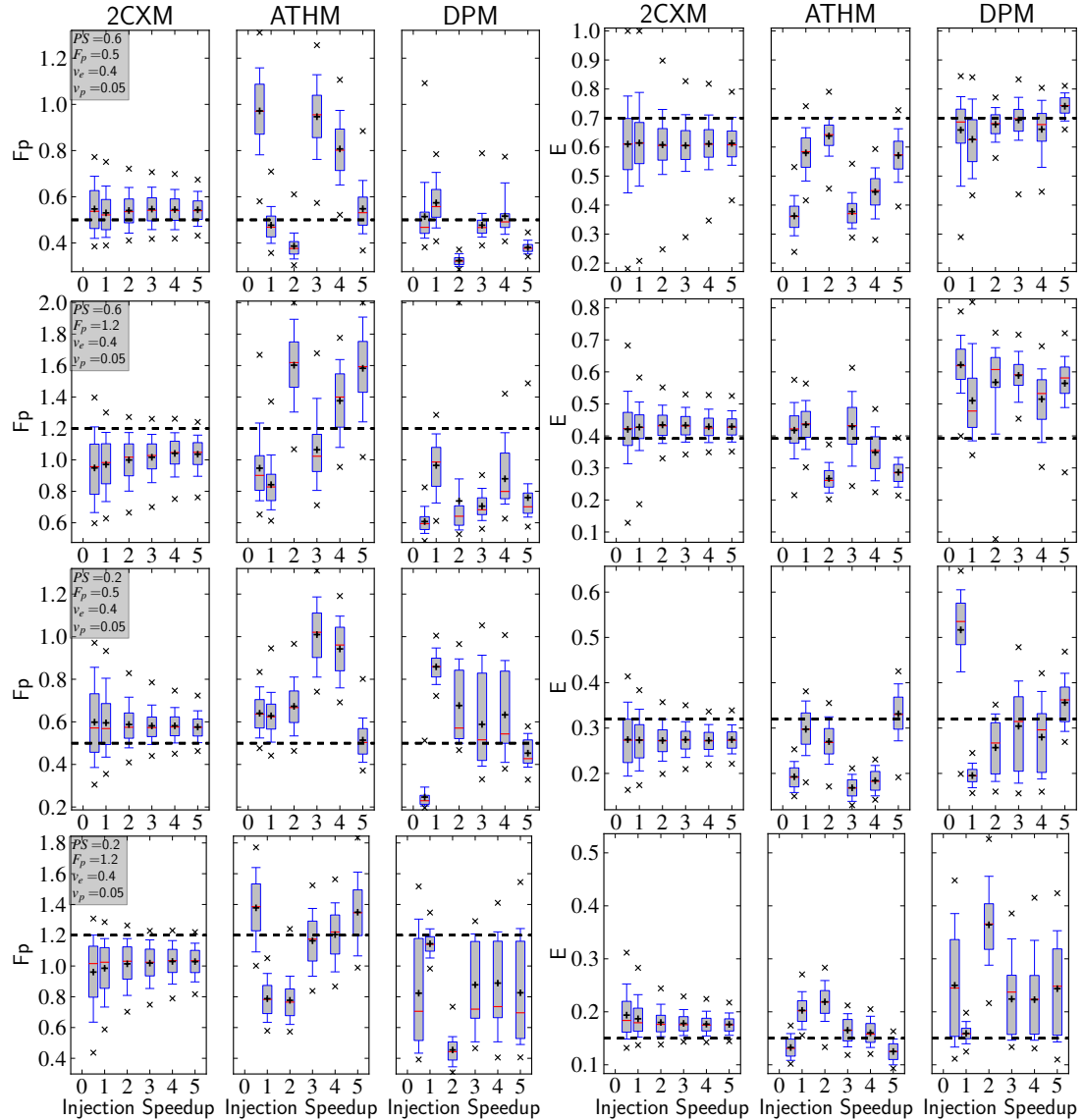


Figure 6.6: Dependence of the accuracy and precision of the blood flow F_p and the extraction fraction E estimates from 2CXM and ATHM on the injection speed for a AIF in a mouse tail with a significant vascular volume (SNR = 30).

6.2 Mismeasurements in the AIF

Parameter distributions for fits with systematically varied deficiencies are shown as indicated in Tab. 6.2.

Error Type	Mouse AIF, $v_p = .5$	Mouse AIF, $v_p = .001$	Human AIF, $v_p = .5$	Human AIF, $v_p = .001$
Bolus Arrival	Fig. 6.7, p.47	Fig. B.13, p.86	Fig. B.14, p.87	Fig. B.15, p.88
Haematocrit	Fig. 6.9, p.50	Fig. B.16, p.89	Fig. 6.10, p.51	Fig. B.17, p.90
Rate	Fig. 6.8, p.48	Fig. B.18, p.91	Fig. B.19, p.92	Fig. B.20, p.93
Horizontal	Fig. 6.11, p.54	Fig. B.24, p.97	Fig. B.25, p.98	Fig. B.26, p.99
Vertical	Fig. 6.12, p.55	Fig. B.21, p.94	Fig. B.22, p.95	Fig. B.23, p.96

Table 6.2: Overview of the results for deficient AIFs and their location in the text.

As described in sect. 5.1 concentration curves were simulated with the mouse and the human reference AIFs (see Fig. 4.1a and 4.1c on p. 21), and fitted with deficient AIFs that were simulated, as described in section 4.3 on p. 23.

The effect of deficient AIFs has previously been discussed in the scope of individual measurements compared to population averaged AIFs in small animals Loveless *et al.* [2012]; McGrath *et al.* [2009]; Pickup *et al.* [2003] and humans Li *et al.* [2011]; Meng *et al.* [2010]. The results are partly ambiguous and indicate that there exists no general answer regarding the need of individual AIF measurements. Again, all aforementioned studies employed only a single PK model (ETM). However, the unclear results suggest a more thorough investigation of the effect of certain types of mismeasurements.

A further important source of error in the AIF is a misestimation of the haematocrit (HCT). The effect of individual HCT measurements compared to a population mean has been investigated in a clinical study on prostate cancer by Just *et al.* [2011] for the ETM. The results indicate a strong underestimation of K^{trans} .

Tab. 6.3 summarizes the results by clustering the susceptibility to the different AIF arrows into eight different categories.

The clustering allows for a few general observations:

- Models with fewer parameters, show a more consistent K^{trans} bias, for a certain type of AIF error. The biases point consistently in the same direction for 13 out of 16 cases within the TM and for 9 out of 16 for the ETM. For the DPM half of the parameters have a consistent bias, while that is the case for only 5 and 3 errors, respectively.

6. ACCURACY AND PRECISION OF HAEMODYNAMIC PARAMETERS

Error Type	Horizontal		Vertical		BAT		Rate		HCT		avg.
Direction	↓	↑	↓	↑	↓	↑	↓	↑	↓	↑	[%]
Mouse											
TM	↑	↑	↑	↓	↑	↑	↑	↑	↓	↑	13
ETM	↑	↓	↓	↓	↓	↓	↓	↓	↓	↑	10
2CXM	↓	↓	↓	↓	↓	↓	↓	↓	↓	↑	12
ATHM	↑	↑	↑	↑	↑	↑	↑	↑	↑	↑	17
DPM	↓	↓	↓	↓	↓	↓	↓	↓	↓	↑	17
Human											
TM	↓	↓	↑	↓	↓	↑	↓	↓	↓	↑	9
ETM	↓	↓	↓	↑	↓	↓	↓	↓	↓	↑	12
2CXM	↓	↓	↓	↓	↓	↓	↓	↓	↓	↑	11
ATHM	↑	↓	↑	↑	↑	↑	↑	↑	↑	↑	13
DPM	↓	↓	↓	↓	↓	↓	↓	↓	↓	↑	13
avg. [%]	8	6	14	6	6	7	12	7	20	39	13

Table 6.3: Effects of the different AIF deficiencies on the K^{trans} estimates for different models from 1000 bootstrap iterations with a SNR of 30. Colors and arrows indicate strength and direction of the mean bias of all 8 parameter setups. The bias is calculated as the relative difference of mean estimate from fitting the tissue uptake curves with a deficient AIF, compared to fitting with the *true* AIF and subsequent averaging over all 8 parameter setups. The magnitude of the AIF error is chosen to be 30% or 3 s, depending on the error type. The arrows indicate, whether K^{trans} is biased towards the same direction for all parameter setups. The bias of the magnitude is coded in the following way: < 3% ; 3% to 6% ; 7% to 10% ; 10% to 15% ; 15% to 20% ; 20% to 30% ; 30% to 50% ; > 40% .

- Errors in haematocrit introduce the strongest bias. Overestimating the haematocrit by 30% introduces an average bias in the mean estimate of 39%, which is roughly twice the bias that is caused by a same-size underestimation and about 3 to 6 times as much as any other AIF error with a size of 30% or 3 s.
- An overestimation of the peak height has the smallest effect on the mean estimates. It never surpasses 15% for $\epsilon = 50\%$ or 6% for $\epsilon = 30\%$. Underestimating the peak height on the other hand, introduces a bias that is more than twice as strong.
- K^{trans} estimates for human AIFs, are on average 20% less susceptible to the investigated AIF errors with 30%/3 s magnitude.

The precision in K^{trans} is not significantly affected by the magnitude of the AIF error in many cases, while large increases are observed for a few settings and especially for the

2CXM and the ATHM. A detailed description of the accuracy for the individual error types and models is given in the following sections.

6.2.1 Rate and Bolus Arrival Time

The Tofts model shows a consistent bias for misestimation in the bolus arrival time (BAT). Underestimating the BAT yields lower K^{trans} estimates, while overestimating it yields higher K^{trans} estimates. These biases amount to 10% to 20% for a BAT shift of 8 s.

Errors of similar size are introduced by fitting AIFs with a wrong rate. Overestimating the rate yields a rather mild decrease in K^{trans} of less than 10% for a 100% error. Underestimating the rate causes a more significant increase in K^{trans} up to 30% for a 50% decrease in the rate of a mouse AIF, while this effect is smaller or completely absent for human AIFs.

The extended Tofts model features a decrease in K^{trans} for an overestimation of the BAT of up to 30% for an error of 8 s. Underestimating the BAT causes either an increase in K^{trans} of the same size (low permeability surface area and significant vascular volume, e.g. Fig. 6.7, p. 47, lower two rows) or leads to a decrease in the precision by up to a maximum of a threefold interquartile range.

Overestimating the rate induces either an increase in the width of the parameter distribution, while the mean stays constant (negligible vascular volume) or a deviation in the mean of 5% to 15%, while the precision is unaltered. Underestimating the rate may have no effect at all (mouse AIF with negligible vascular volume, e.g. Fig. B.20, p. 93) or may yield a large decrease in K^{trans} (e.g. for a human AIF with significant vascular volume in Fig. B.19, p. 92)

The two-compartment exchange model shows various effects. Errors in the BAT have mostly no impact on the accuracy for a negligible vascular volume (e.g. Fig. B.15, p. 88). For significant vascular volumes an error in the BAT in any direction yields a decrease in K^{trans} . This decrease is more pronounced for an underestimation of the BAT and a small permeability surface area.

Errors in the rate almost always cause a loss in precision. Underestimating the rate leads mostly to underestimates in K^{trans} accuracy while the effect of a rate overestimation on the accuracy is variable in size and direction.

6. ACCURACY AND PRECISION OF HAEMODYNAMIC PARAMETERS

The adiabatic approximation to the tissue homogeneity model shows fluctuations in the parameter accuracy for errors in the BAT, that have a magnitude up to 20% over the whole range of -8 s up to 8 s , while the interquartile range increases up to threefold.

Overestimating the rate causes a much large decrease in precision. Widely independent of the size of the error, the interquartile range increases by a factor of five, while the effects on the accuracy are mixed and moderate in size. Underestimating the injection rate induces a higher K^{trans} estimates for a significant vascular volume.

The distributed parameter model, again, is not impaired in its high precision by any of the errors. An error in the rate has a rather small effect on the accuracy, which is mostly smaller than 10% for a rate error of 50%. Overestimation of the rate yields slightly smaller K^{trans} estimates.

Errors in the BAT cause fluctuations in the predicted K^{trans} means, with a global bias towards smaller K^{trans} values. These fluctuations have a magnitude up to 30% (e.g. in the 2nd row in Fig. 6.7, p. 47) but are notably lower for most other cases (e.g. in the same Fig., 4th row).

6.2 Mismeasurements in the AIF

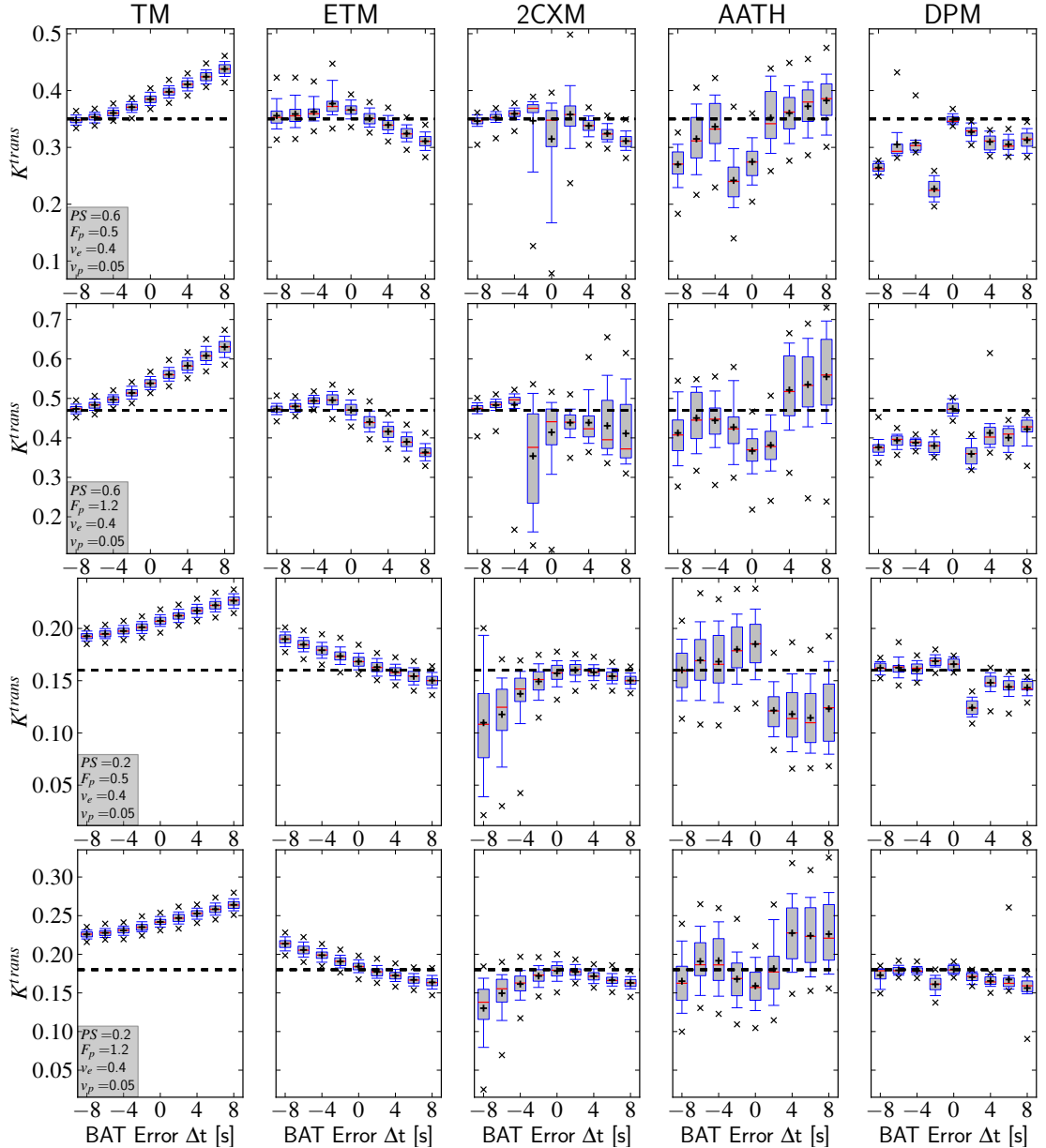


Figure 6.7: Accuracy and precision in K^{trans} for mouse AIFs with a error in the bolus arrival time. The AIFs are shown in Fig. 4.3, p. 24.

6. ACCURACY AND PRECISION OF HAEMODYNAMIC PARAMETERS

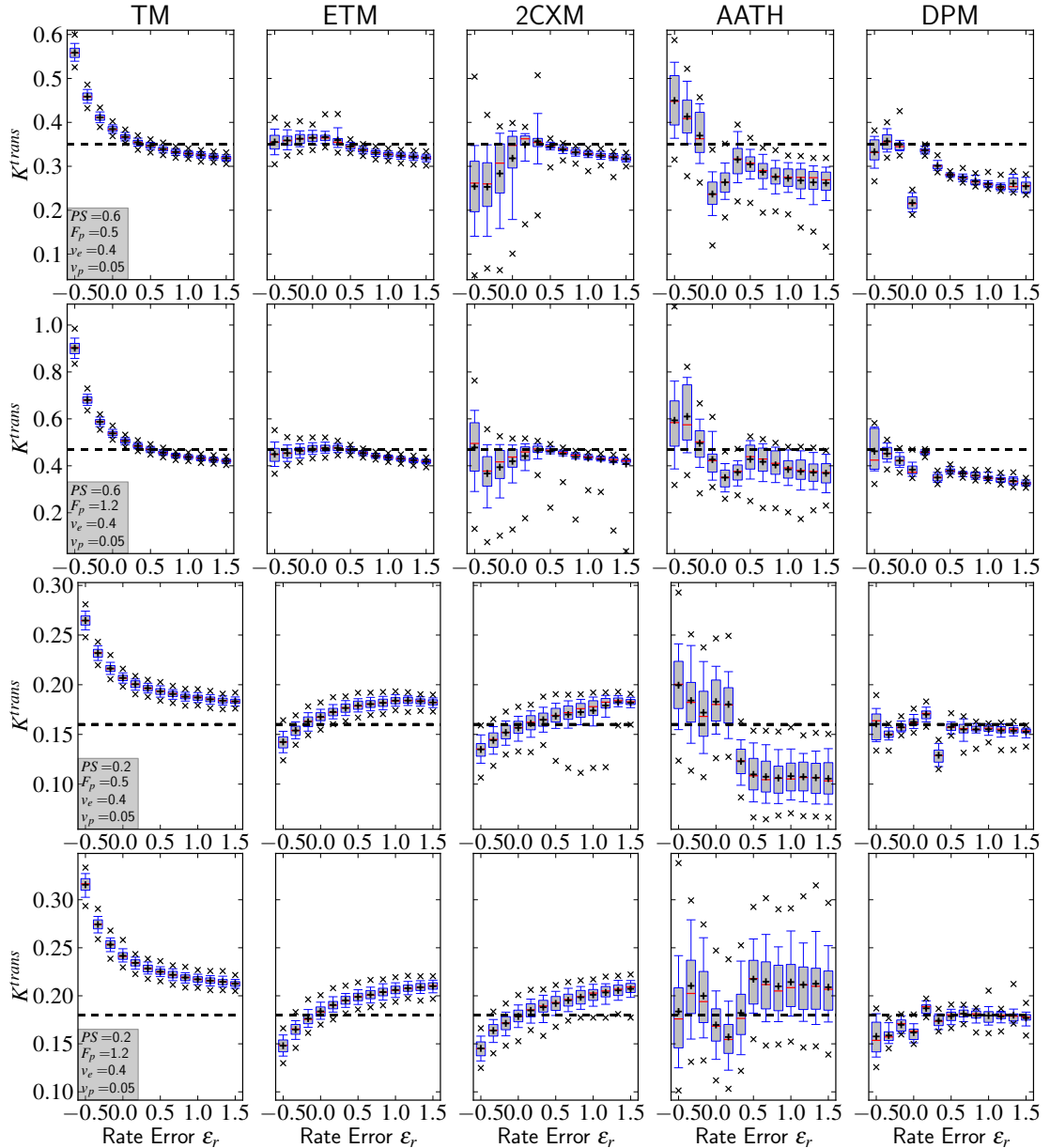


Figure 6.8: Accuracy and precision in K^{trans} for mouse AIFs with an error in the rate. The AIFs are shown in Fig. 4.1, p. 21.

6.2.2 Haematocrit

Errors in the haematocrit cause a similar bias in the K^{trans} estimates for all models. This bias is approximately proportional to that of the haematocrit. A 20% overestimation of the haematocrit causes an overestimation in K^{trans} of roughly the same size, while the effect of an underestimation is slightly milder. This holds true for all setups and human, as well as mouse AIFs. Merely the **ATHM** features a more scattered behavior and an overall weaker bias. The K^{trans} precision is constant. These results agree with observations that [Roberts *et al.* \[2011\]](#) have made for the TM.

Overall the effect of an error in the HTC is big compared to the other investigated sources of error. As discussed in sect. 4.3.2 these errors are common, due to a lack of individual HTC measurements. Therefore, an individual measurement of the HTC is of similar importance as an individual AIF measurement.

6. ACCURACY AND PRECISION OF HAEMODYNAMIC PARAMETERS

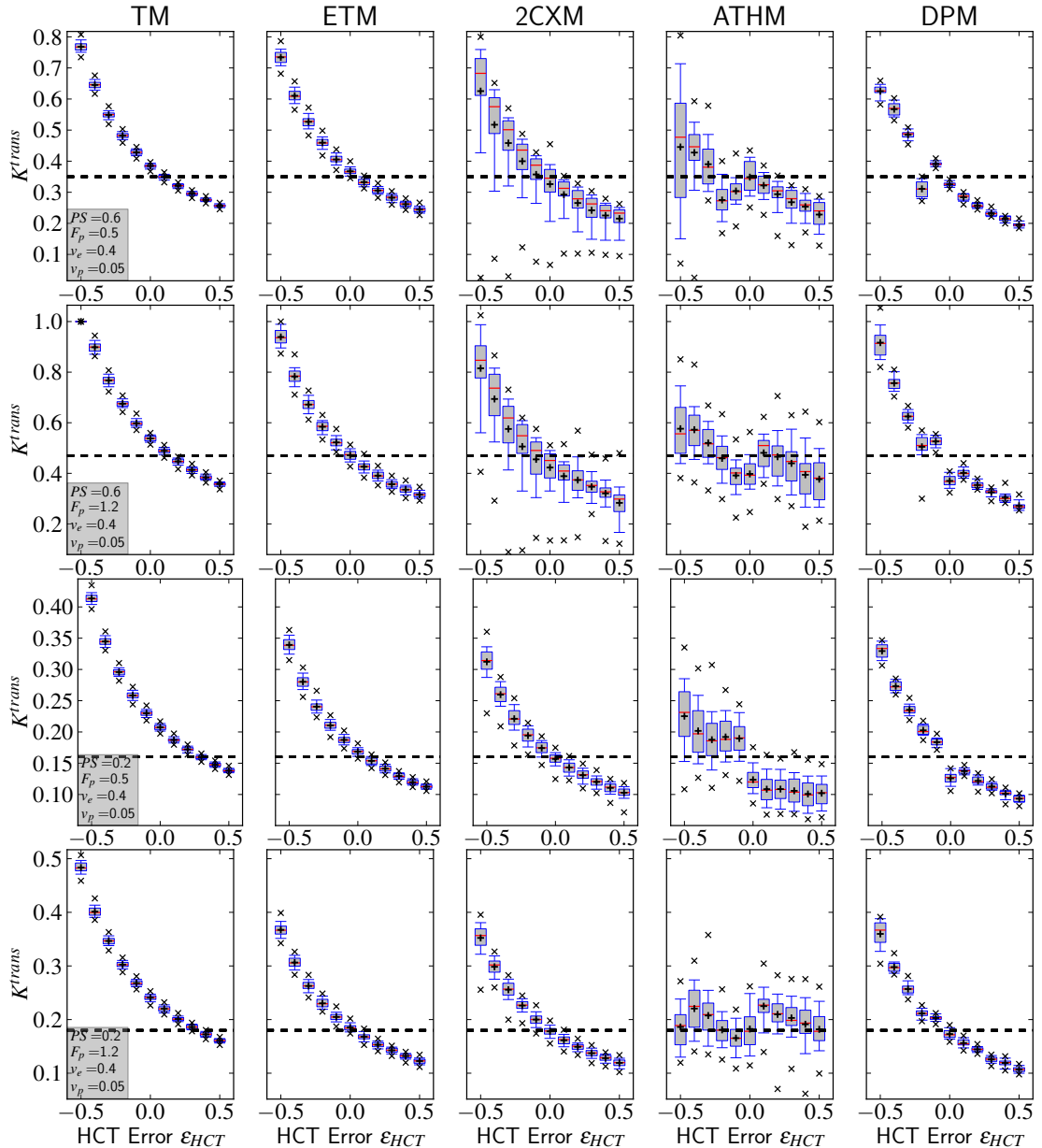


Figure 6.9: Accuracy and precision in K^{trans} for mouse AIFs with a error in the haematocrit. The AIFs are shown in Fig. 4.4, p. 25.

6.2 Mismeasurements in the AIF

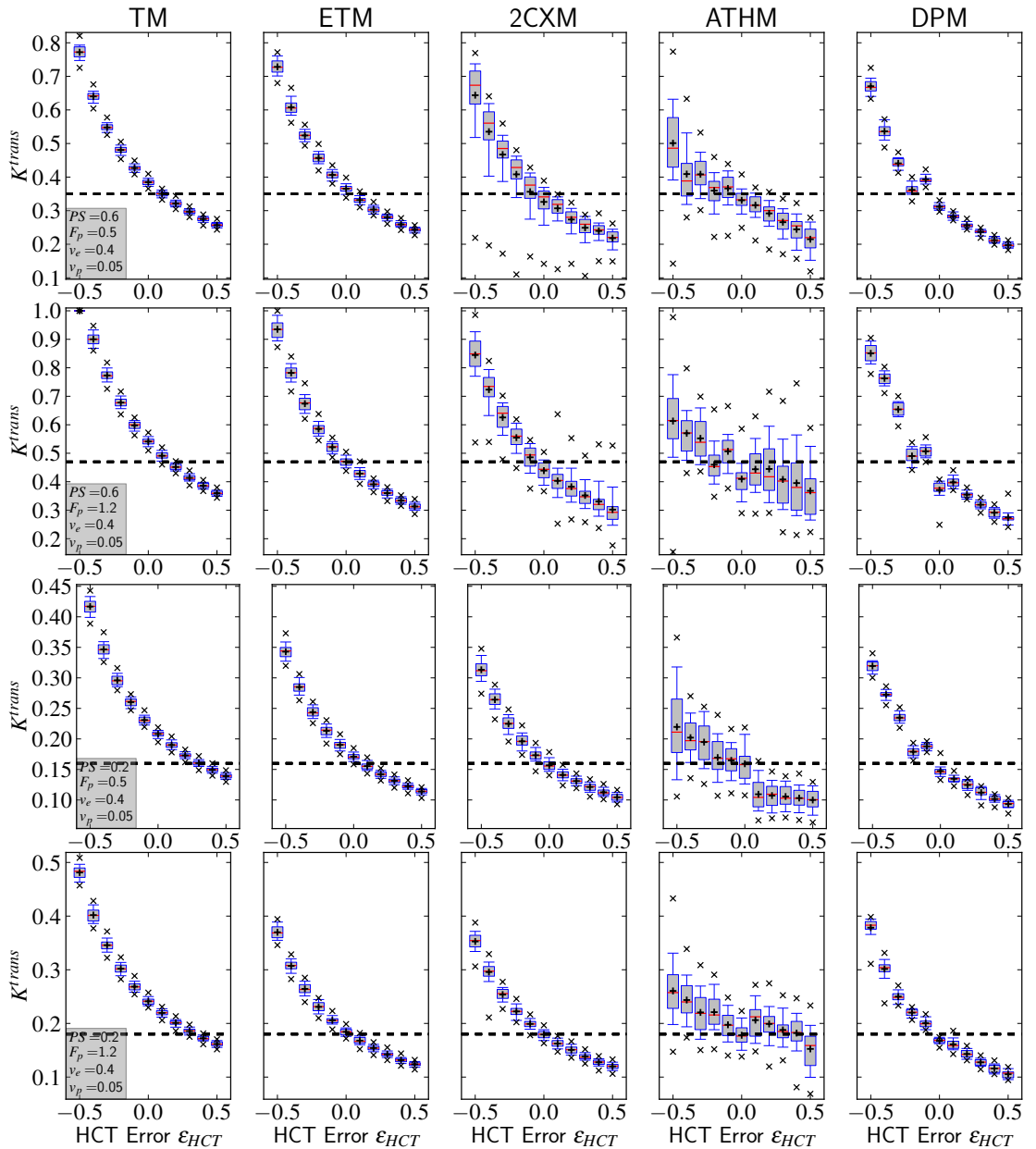


Figure 6.10: Accuracy and precision in K^{trans} for human AIFs with an error in the haematocrit. The AIFs are shown in Fig. 4.4, p. 25.

6. ACCURACY AND PRECISION OF HAEMODYNAMIC PARAMETERS

6.2.3 Horizontal and peak AIF concentration

The **Tofts model** is mostly insensitive to a horizontal shift in the AIF peak. A 100% shift towards positive times introduces overestimation in K^{trans} of less than 5% in any case. The strongest bias of this kind is observed for a high flow and a high permeability surface area in a mouse tail (Fig. 6.11 on p. 54, 2nd row). Almost no bias is apparent in most of the other setups.

A vertical shift in the AIF peak introduces a bias, whose magnitude and direction depends strongly on the direction of the shift. An overestimation of the peak concentration yields a rather mild bias towards smaller K^{trans} values. Its magnitude never exceeds 5% per 50% shift. Opposed to that, an underestimation of the peak concentration introduces a significant overestimation in K^{trans} , such that a peak underestimation of 50% causes an overprediction between 30% and 100%. Both effects are less pronounced in human AIFs.

The **extended Tofts model** shows similar behavior to that of the TM for vertical shifts in the AIF in a mouse tail. Overestimating the peak concentration has an even smaller effect and the overall bias is significantly smaller for small permeability surface areas. (Compare rows 1/2 with 3/4 in Fig. 6.12, p. 55.) For human AIFs underestimation of the AIF peak yields a reverse bias, such that K^{trans} is underestimated up to 50%, for a peak concentration that is underestimated by the same percentage (e.g. Fig. B.25, p. 98).

For the special case of an overestimation of the AIF peak within the ETM a simulation study has been previously carried out by Cheng [2008]. It reports a K^{trans} bias, that is inversely proportional to error in the vertical position of the AIF peak. This is in rough qualitative accordance with the above observations for a mouse AIF, but contradicts the results for the human AIF. The general behavior of the ETM for such error in the AIF is heterogeneous and dependent on the actual form of the AIF. It does not allow for such general conclusions.

Horizontal shifts towards larger times yield a underestimation of K^{trans} up to 50% for a shift of 100%, while such shifts towards smaller times yield an overestimation of similar magnitude for most studies. These effects are smaller for a negligible vascular volume.

The **two-compartment exchange model** shows no consistent trends for horizontal, nor for vertical shifts of the AIF peak. The precision, as well as in the accuracy of K^{trans} estimates for mouse AIFs are more susceptible to both, horizontal and vertical

6.2 Mismeasurements in the AIF

shifts than estimates for human AIFs. For some setups the precision is heavily impaired (e.g. in the 2nd row of Fig. B.26, p. 99; human AIF, negligible VS), while others show no such behavior (e.g. in the 4th row in Fig. 6.12, p. 55; mouse AIF, significant VS). As it has been already observed for the Tofts models, an overestimation of the peak concentration has a very small influence on the accuracy of less than 5% for a 100% peak error in any case.

The adiabatic approximation to the tissue homogeneity model features a deviation in the K^{trans} mean of up to 20% for a 50% horizontal shift of the AIF in both directions. This effect typically constant from AIF shifts of 30% onward and is most apparent for setups with a small permeability surface area. The precision of the estimates show fluctuations but mostly no overall impairment for larger errors.

An overestimation of the peak concentration produces similar errors, while an underestimation, again, introduces large errors, which are less significant for low permeability surface area. (Compare e.g. rows 1/2 with rows 3/4 in Fig. B.21, p. 94.)

The distributed parameter model features almost no impairment in the remarkable high precision of its estimates for either error. A horizontal shift of 100% towards positive times causes K^{trans} estimates to be up to 20% lower for mouse AIFs, while estimates for human AIFs are hardly affected, at all.

Overestimation of the peak AIF concentration by 100% causes a change in the K^{trans} accuracy of less than 15%. Underestimation of the peak concentration causes changes of up to 20% for a 50% underestimation in some cases, and much smaller biases in other cases. Generally peak overestimation yields lower K^{trans} estimates for mouse AIFs, while the effect for human AIFs is mixed.

6. ACCURACY AND PRECISION OF HAEMODYNAMIC PARAMETERS

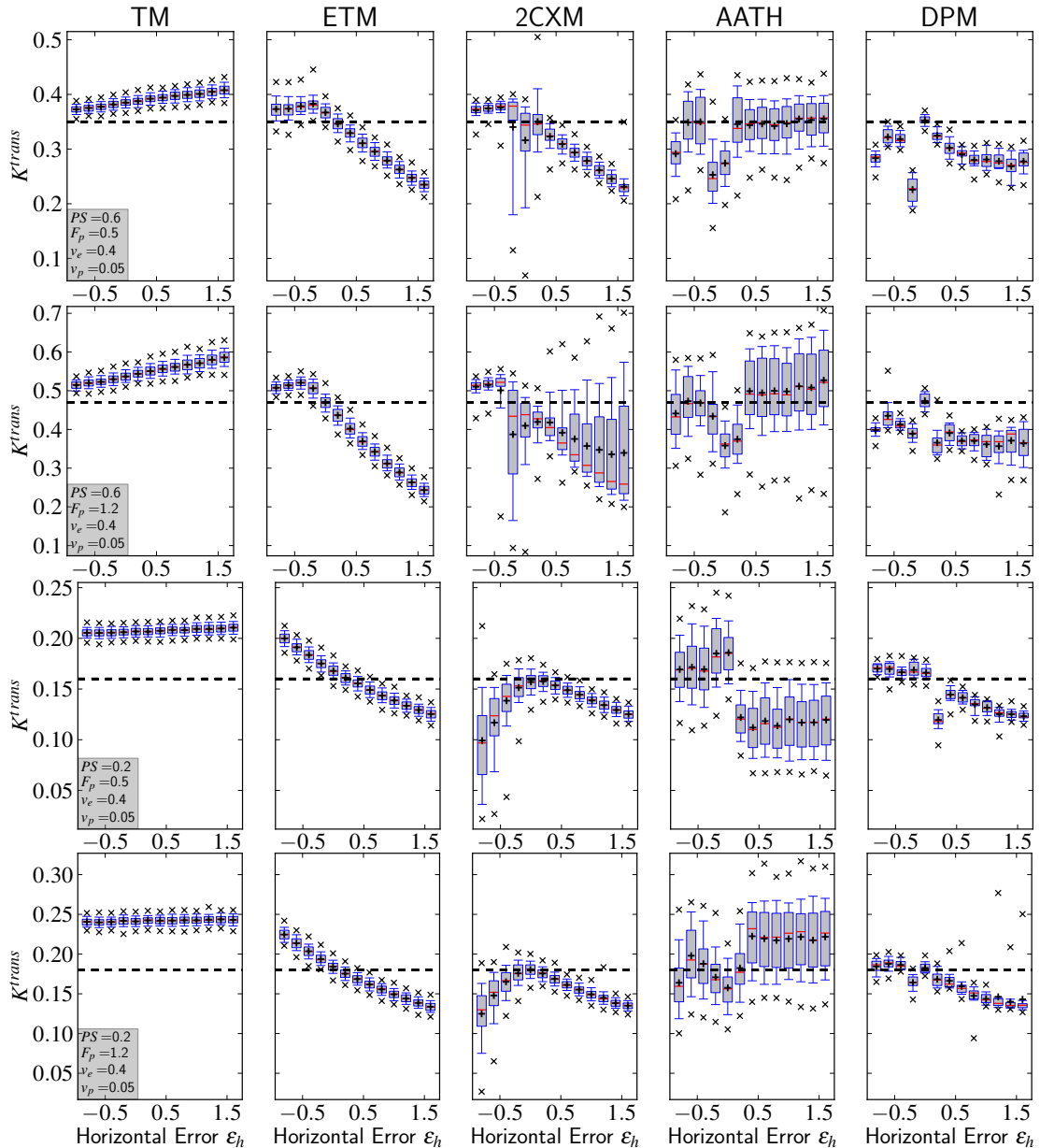


Figure 6.11: Accuracy and precision in K^{trans} for mouse AIFs with a error in the horizontal peak position. The AIFs are shown in Fig. 4.5 on page 27.

6.2 Mismeasurements in the AIF

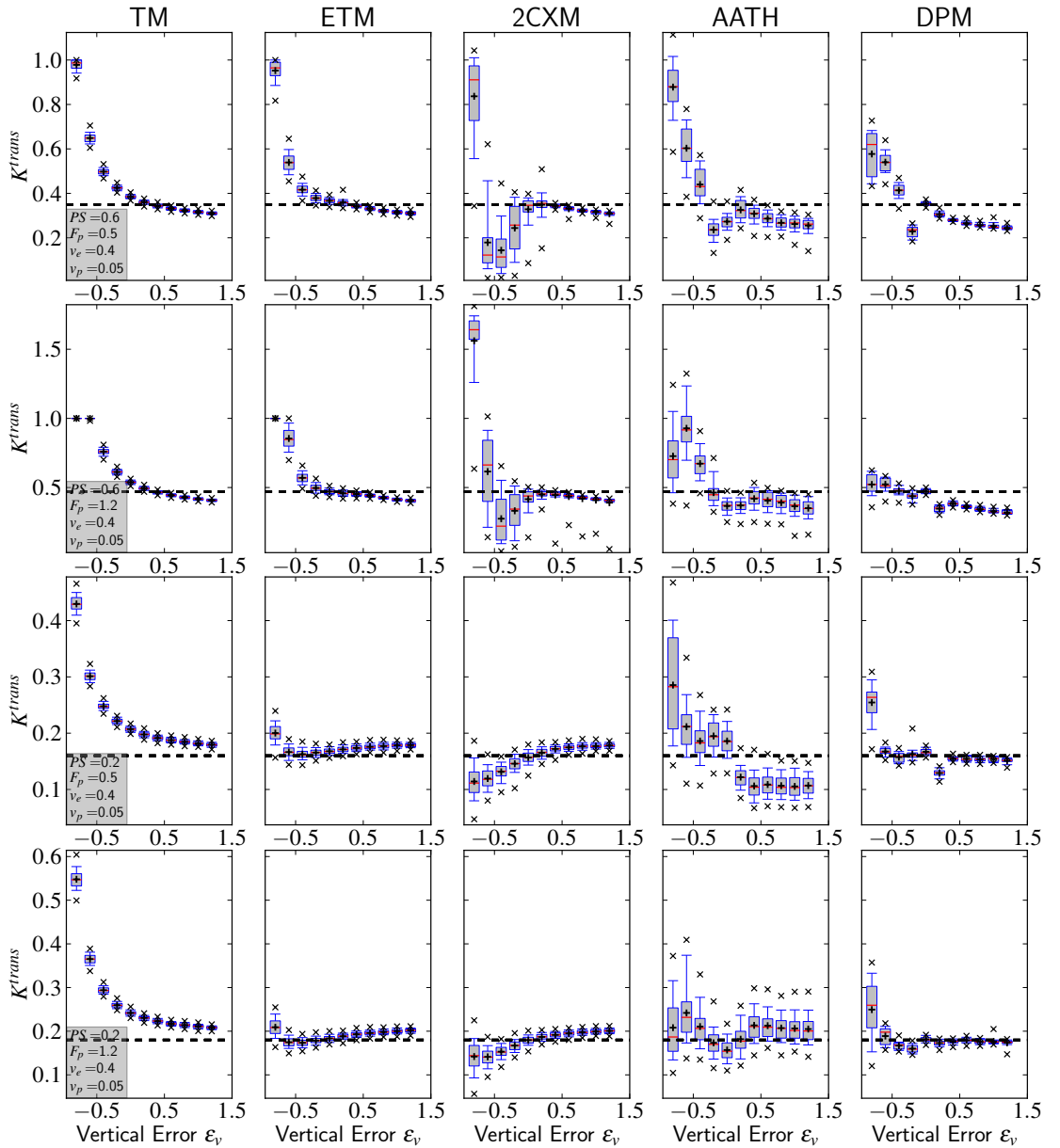


Figure 6.12: Accuracy and precision in K^{trans} for mouse AIFs with a error in the peak AIF concentration. The AIFs are shown in Fig. 4.5 on page 27.

6. ACCURACY AND PRECISION OF HAEMODYNAMIC PARAMETERS

6.3 Variation of the SNR

The distribution of K^{trans} estimates under variation of the SNR for two generic setups is shown in Fig. 6.13. A separate discussion of the influence of the SNR on the accuracy and the precision follows.

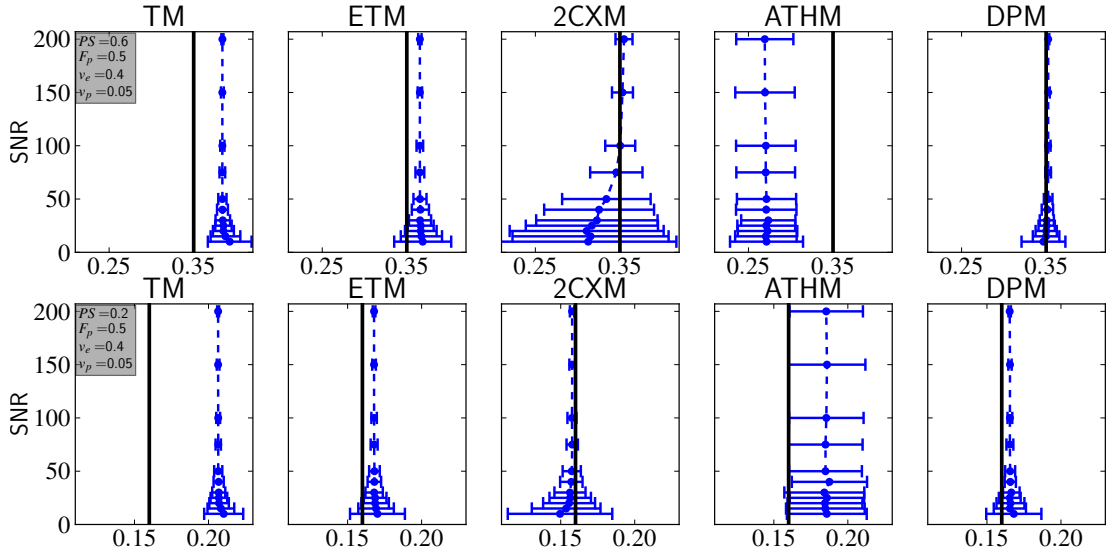


Figure 6.13: Accuracy and precision for different SNRs and models, for two parameter setups with a mouse AIF.

Parameter Accuracy For SNRs greater than 20 most of the employed models show now bias in the K^{trans} accuracy under SNR variation as it is shown in Fig. 6.13. Solely, the 2CXM tends to underestimate K^{trans} for SNRs below 100.

This behavior is apparent throughout most other parameter setups as indicated by Fig. 6.14, which shows the relative accuracy in K^{trans} for all models, averaged over all parameter setups. The 2CXM shows a significant K^{trans} underestimation of up to 15% for SNRs lower than 200. The other three models consistently predict the same mean value for all parameter setups and SNRs from 20 onward and do not feature a bias under variation of the SNR.

A previous simulation study by [Kershaw & Cheng \[2010\]](#) reported accurate estimates for sufficiently high SNRs and sampling rates within the ATHM. While the sampling rate was not varied in this study, its results indicate that the bias does not depend on the SNR. This might be due to the insufficient sampling rate or the different approach in simulating the ground truth.

6.3 Variation of the SNR

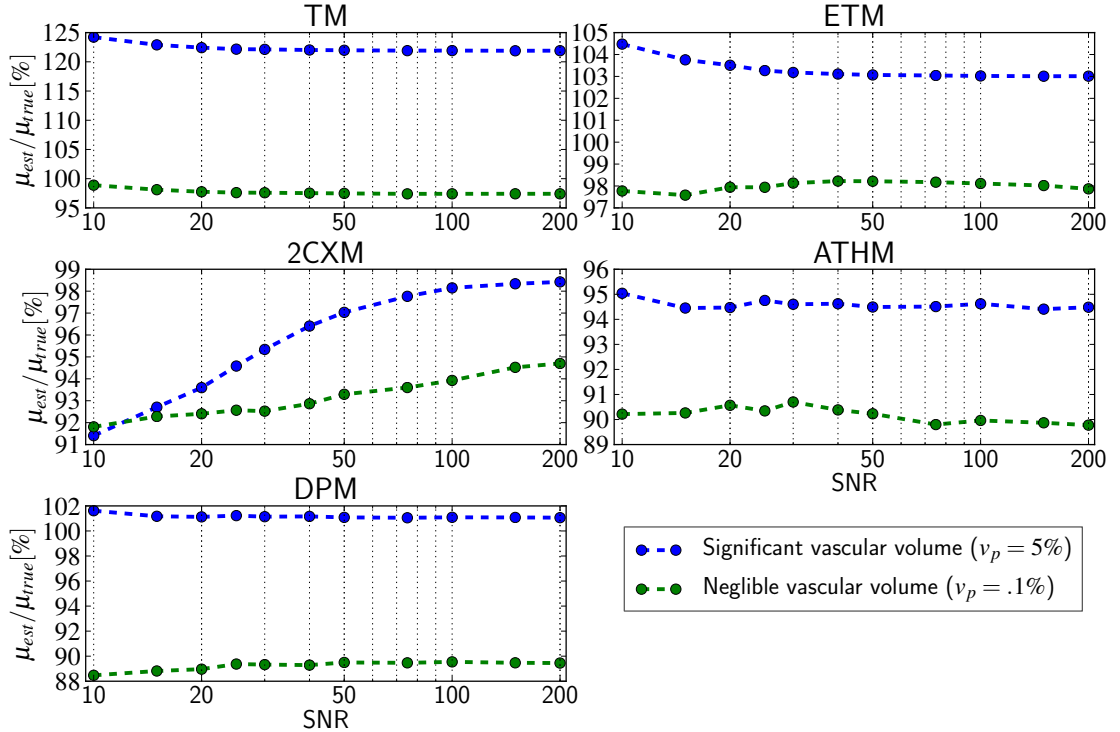


Figure 6.14: Averaged K^{trans} accuracy for significant and insignificant vascular volumes. Averages are taken over all parameter combinations (see p. 22) and human, as well as mouse AIFs.

Parameter Precision Fig. 6.15 shows the averaged K^{trans} precision. As expected models with fewer parameters feature an overall higher precision. Thus the simple Tofts model performs best for every SNR. Nevertheless, the c_v differences to the ETM, the ATHM, and the DPM with three and four parameters are not larger than 2% to 10%.

Generally, for these four models, the coefficient of variation features a exponentially decaying behavior on a logarithmic SNR scale. Thus the improvement in precision in a regime of high SNRs is very small compared to low SNRs, and eventually the c_v does not improve notably for higher SNRs. The ATHM Model will not benefit from SNRs higher than 50. The Tofts and extended Tofts Model shown an improvement less than 2% for a SNR that improves from 50 to 100.

The 2CXM features a different behavior. It performs worse in precision than any other models for low SNRs. For higher SNRs it shows a rather linear behavior on a logarithmic SNR scale. Thus a higher SNR yields an improvement of precision, even in the regime of high SNRs.

For maximum likelihood approach [De Naeyer *et al.*, 2011] found that the precision

6. ACCURACY AND PRECISION OF HAEMODYNAMIC PARAMETERS

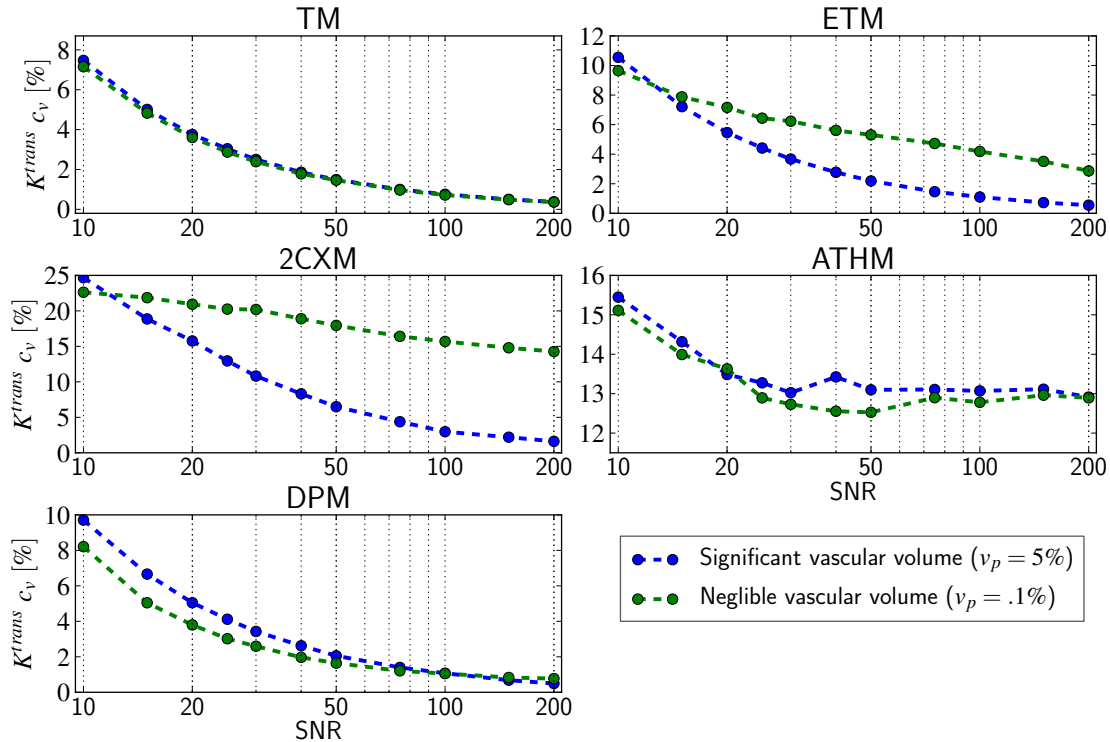


Figure 6.15: Coefficient of variation (c_v) for K^{trans} as a function of SNR. The curves show averages over all parameter combinations (see p. 22) and human, as well as mouse AIFs.

of K^{trans} is proportional to the SNR. This strongly contradicts the results that are presented above.

6.4 Information Criteria Weighted Parameter Estimates

AIC and BIC weights are calculated as described in section 5.4. The original fits to the AIF in a mouse tail and a human AIF were used for simulating the data with the MMID4. The consequent K^{trans} estimates for the mouse AIF are shown in Fig. 6.16 (p. 61) and the corresponding AIC and BIC weights in Fig. 6.17 and 6.18 (pp. 62, 63). The same data for the human AIF is given in the appendix in Fig. B.27 (p. 100) and the corresponding weights in Fig. B.28 and B.29 (pp. 101, 102).

By means of their interquartile range the AIC and BIC weighted parameter estimates are similarly good as estimates from the best model for most cases. Only if one of the models features very accurate estimates, these might not be fully reproduced by the AIC weighting (e.g. the setup in the 1st row of the 1st column in Fig. 6.16, p. 61). Even here the deviation in terms of the means is clearly below 5%. In other cases the weighted estimates are as accurate as, the best of the single models (e.g. in the setup in the 3rd row of the 1st column in Fig. B.27, p. 100). While its overall precision is similar to that of the best models, the distribution of the AIC weighted estimates features heavier tails, i.e. outliers outside the double interquartile range occur more frequently than they do for any of the single models. To a distinctly smaller extent this is also true for the BIC weighted estimates. The BIC penalizes the number of parameters stronger than the AIC and thus the TM has overall higher weights than it does for AIC based model selection. However, the BIC criterion only rejects the TM for a significant vascular volume in cases of a low permeability surface area ($PS = 0.2 \text{ min}^{-1}$), while it still gives most weight to the TM for a high PS of 1.2 min^{-1} .

The distribution of the weights in Fig. 6.17 (p. 62) shows, that the AIC tends to reject the TM for a significant vascular volume, while it puts most weight on it for a negligible vascular volume. In this sense the AIC weight itself correctly gives some indication of the underlying physiology. The ATHM exhibits overall negligible weights with means lower than 5% in any case.

The interquartile range of the weights varies over a large range of 5% up to 50%. For the first row in Fig. 6.17 the variability is especially large. Thus it can be concluded that the physiology of a system with high permeability surface area ($PS = 0.6 \text{ min}^{-1}$), a low flow ($F_p = 0.5 \text{ min}^{-1}$) and a high vascular volume (5%) is comparably poorly captured by the proposed models. Opposed to that the distribution of the weights in the first column of the last row in the same Fig. is particularly precise. The given set of models is more appropriate to describe tissue with low permeability surface area ($PS = 0.2 \text{ min}^{-1}$), a high flow ($F_p = 1.2 \text{ min}^{-1}$), and a significant vascular volume.

6. ACCURACY AND PRECISION OF HAEMODYNAMIC PARAMETERS

The overall difference between the AIC and the BIC estimates is very subtle. In the majority of cases the AIC produces more accurate results, while the BIC is slightly more precise. In order to decide between the two, further investigations are indicated. Previous results by [Buckley \[2002\]](#) showed that the Tofts model overpredicts K^{trans} for a nonzero vascular space. This behavior is reproduced by our investigation.

A recent publication by [\[Luypaert et al., 2012\]](#) indicates that AIC weighted parameter estimates are useful in some cases while they introduce a biases or a loss of precision in others. This study uses one of the model candidates (2CXM) as ground truth, which seems problematic, especially for investigation of a model selection criterion. However, the authors interpretation of their findings contradict the results of the study at hand.

6.4 Information Criteria Weighted Parameter Estimates

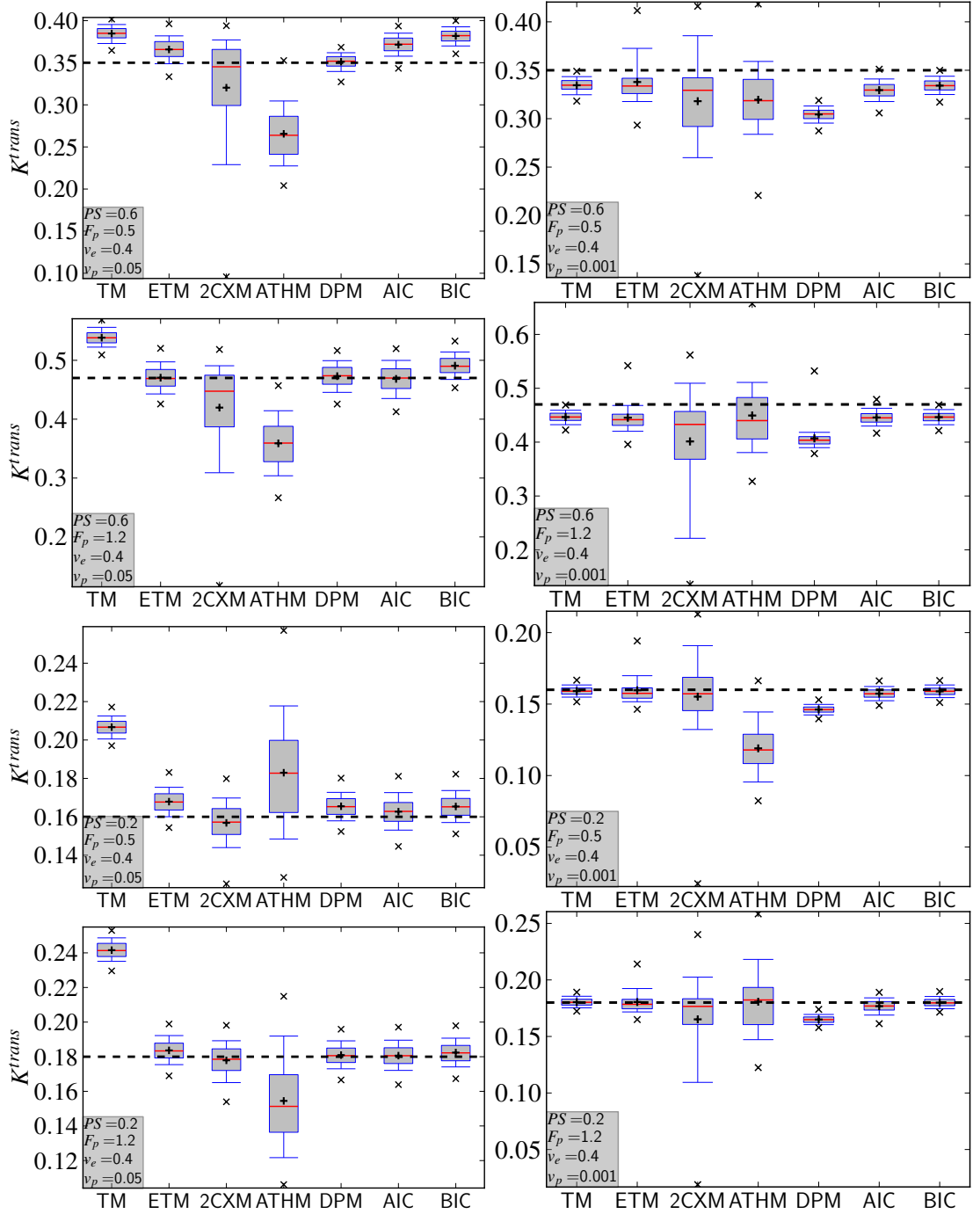


Figure 6.16: Comparison of Model Estimates and AIC/BIC weighted averages for a mouse AIF (Reference AIF, as shown in Fig. 4.1a, p. 21). The corresponding weights are shown in Figs. 6.17 and 6.18.

6. ACCURACY AND PRECISION OF HAEMODYNAMIC PARAMETERS

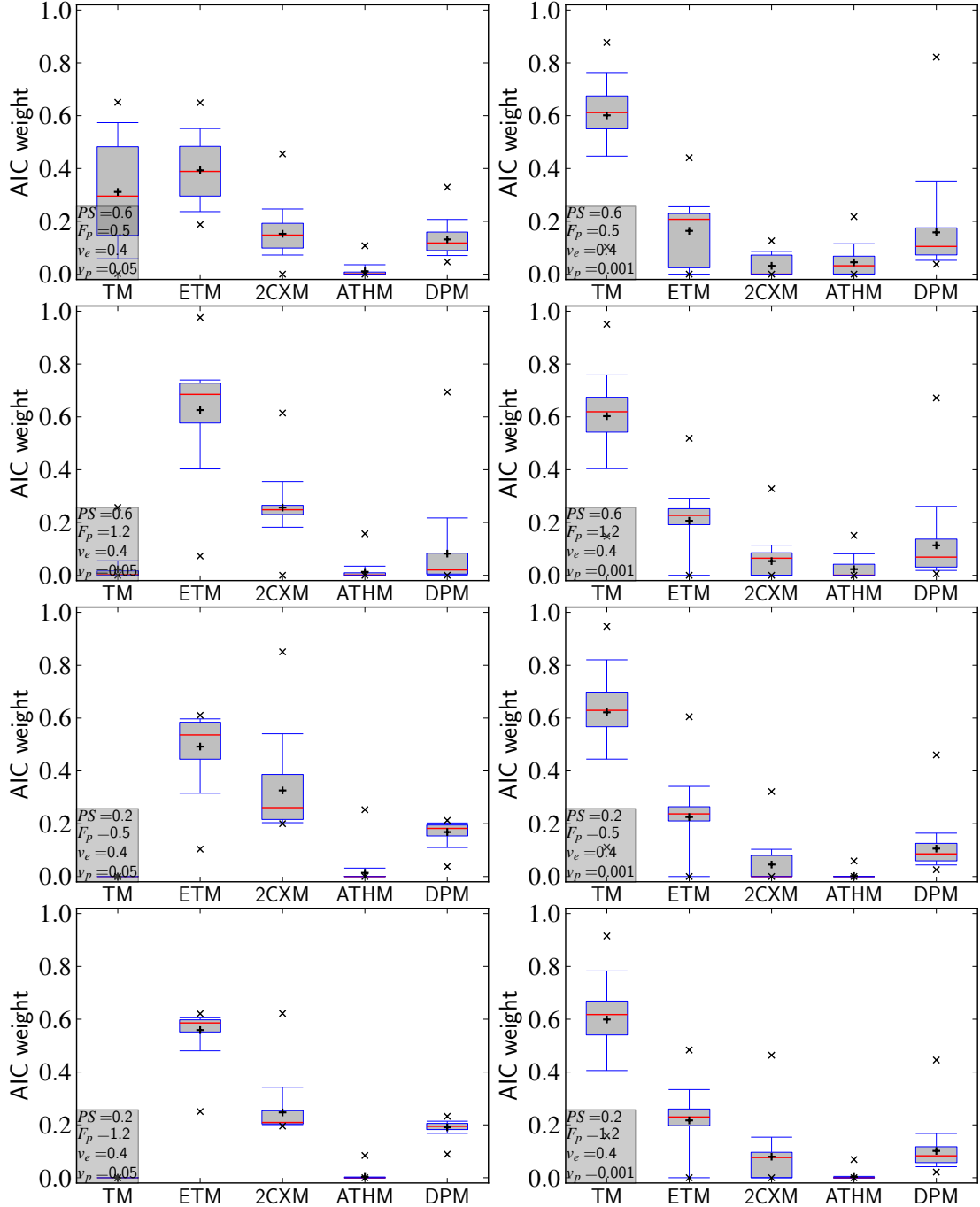


Figure 6.17: AIC weights for uptake curves, based on a mouse AIF. The corresponding K^{trans} estimates are shown in Fig. 6.16.

6.4 Information Criteria Weighted Parameter Estimates

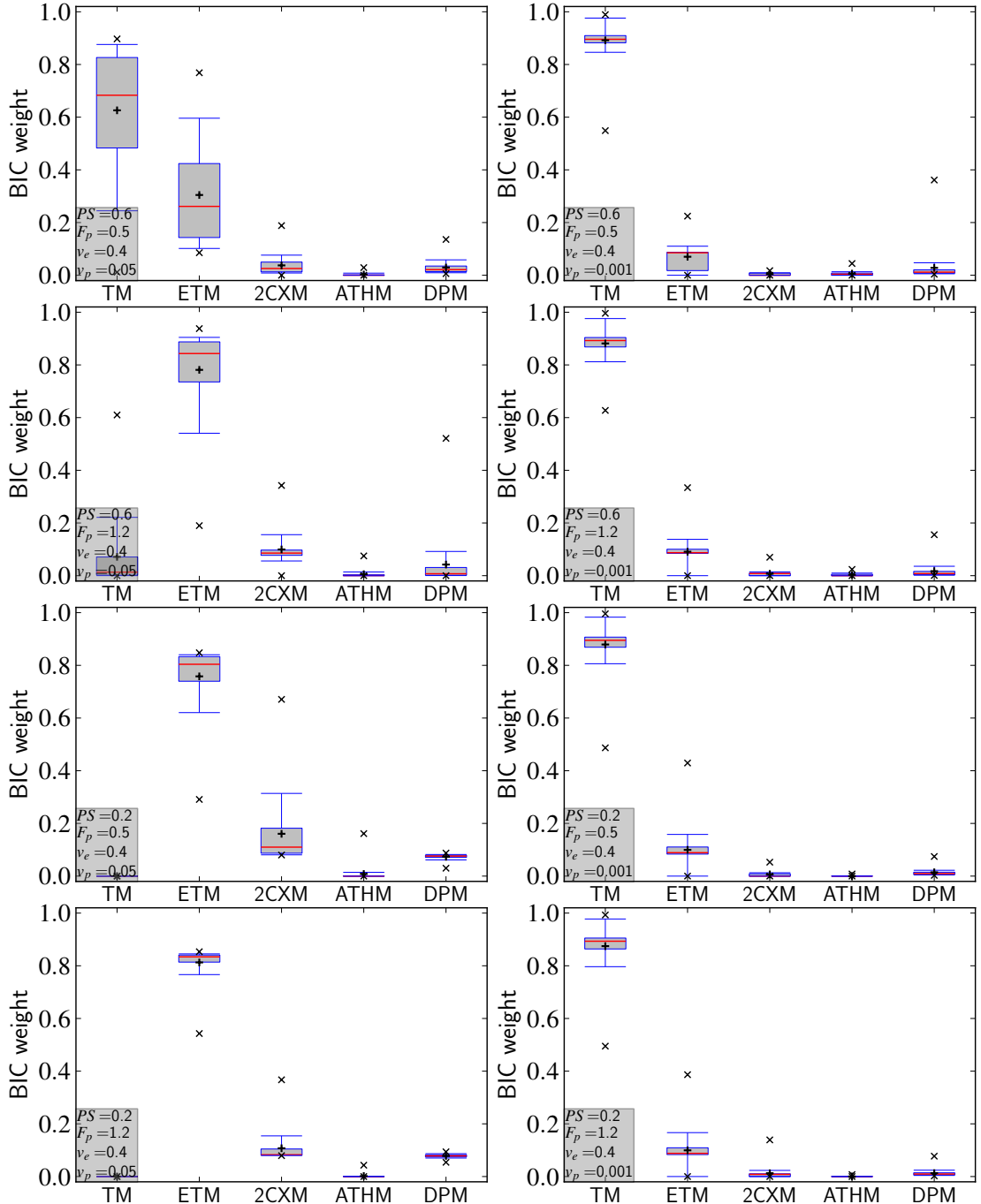


Figure 6.18: BIC weights for uptake curves, based on a mouse AIF. The corresponding K^{trans} estimates are shown in Fig. 6.16.

6. ACCURACY AND PRECISION OF HAEMODYNAMIC PARAMETERS

7

Discussion and Conclusion

For the application of pharmacokinetic models in clinical, as well as in preclinical DCE-MRI it is important to understand the meaning and the reliability of the different models and their parameter estimates. In order to do so, a variety of similar simulation studies has been carried out. One of the first investigations by [Buckley \[2002\]](#) suggested the MMID4 to generate tissue uptake curves that closely match experimental data. More recent studies generated data, by use of the the 2CXM or the ATHM [Kershaw & Buckley \[2006\]](#); [Luypaert *et al.* \[2011, 2012\]](#), which raises the difficulty to distinguish between inappropriate assumptions within the model used to simulate the data vs. inappropriate assumptions in the model used for fitting. While the MMID4 does certainly not eradicate this problem, it is a step towards a proper description of the tissue physiology.

As already shown by [Buckley \[2002\]](#), the Tofts model overpredicts K^{trans} in tissues with a non-zero vascular volume, which it does not account for. For a finite vascular volume the precision of the TM and the ETM are similar. For tissues with a negligible v_p , the precision of the TM is significantly higher, while the ETM is capable of detecting the true negligible v_p with high accuracy and precision. Thus it is an advisable strategy to apply the TM, in cases where the ETM estimates a negligible v_p . This would yield a higher precision in parameter estimation without losing information about v_p . As expected for models with a higher number of parameters, the precision of the 2CXM and the ATHM are clearly lower than those of the TM and ETM. Remarkably enough, this is not the case for the DPM, whose precision usually ranges between those of the TM and the ETM and is clearly superior to the other 4-parameter models. While the DPM outruns the ATHM and the DPM by its precision, the 2CXM is superior regarding the accuracy and consistency of its predictions under variation of the arterial

7. DISCUSSION AND CONCLUSION

input. The means values of its K^{trans} , E , and F_p estimates feature no fluctuations under variation of the injection rate.

Of the 4-parameter model studied, either the 2CXM or the DPM could be chosen. The decision between the two models comes down to a consideration of accuracy (2CXM) compared to precision (DPM).

The strong dependence of the haemodynamic parameters' accuracy and precision on the particular AIF and the actual tissue parameters emphasizes importance of the choice of a single model. Thus, it seems natural to delay the decision for a certain model to a later point in time in the analysis procedure. A promising approach is given by a voxel-wise choice of model, using the Akaike or the Bayesian information criterion (AIC, BIC). This approach has recently been investigated by [Luypaert et al. \[2012\]](#), who modelled the tissue uptake using one of the models under investigation. Especially for a model-comparison study, which seeks to find the best model out of a set of candidate models, it is advisable to simulate tissue-uptake curves not by one of the candidate models itself, as already mentioned. Due to these limitations further investigations on this issue are necessary.

Results of this study are discussed in the same order that the corresponding objectives have been presented in chapter 1:

1. Fast injections are recommended for measurements, that are to be analyzed with the ETM or the 2CXM. Nevertheless the significance of the benefit remains rather vague. The observations for the ETM comply with results from [Aerts et al. \[2008\]](#), who investigated data that was simulated and fitted with the ETM under a variation of K^{trans} , with the other parameters held constant. The magnitude of this effect varies largely between different parameter setups and AIF types and amounts to a maximum decrease in the IQR of 30% for a doubled injection rate for the 2CXM, while it is negligible for other parameter setups. E.g. for human AIFs, a gain in precision is almost absent and in any case irrelevant for practical considerations. The benefit from fast injections is highest in the range of the reference injection rates, which resemble typical experimental values and therefore correspond to the regime of practical interest. This would indicate that a further increase of injection rates over the ones currently used in typical clinical and pre-clinical DCE-MRI studies to approximate the theoretical ideal of a δ -function, do not promise improved DCE-MRI data quality. Furthermore, estimates from TM, ATHM, and DPM exhibit no systematic dependence on the injection rate.

-
2. For all models, except the ATHM, an overestimation of the AIF peak concentration causes a bias that is very small compared to other error types. In particular over and underestimation of the peak concentration have a strongly asymmetric effect. The bias that is introduced by an underestimation of the peak concentration is distinctly larger.

For the special case of an overestimation of the AIF peak within the ETM, a simulation study has been previously carried out by [Cheng \[2008\]](#). It reported a K^{trans} bias, that is inversely proportional to errors in the peak AIF concentration. This is in rough qualitative accordance with the above observations for a mouse AIF, but contradicts the results for the human AIF. The strength and direction of this bias is clearly more heterogeneous than those results suggested and depends on the model and the tissue parameters. Significant variability in the peak concentration has been observed clinically [[Parker *et al.*, 2006](#)]. Thus, special care should be taken in population averages to avoid an underestimation of the actual arterial input, as compared to a rather harmless overestimation.

The biases in estimates from the TM and the ETM are mostly consistent in size and direction, while they are hardly predictable for the other models. This can be advantageous for the inter- and intra-patient comparability, if the assumed AIF is deficient in a consistent manner.

It has been pointed out by [Parker *et al.* \[2006, chap. 6, sect. 6\]](#), that the haematocrit (HCT) is one of the major sources of error in a DCE-MRI experiment. The study at hand shows, that errors in the haematocrit introduce a very strong and remarkably consistent bias in the parameter estimates. These results agree with observations that [Roberts *et al.* \[2011\]](#) made for the TM. The consistency does not necessarily allow for inter- and intra-patient comparability, since the Haematocrit is known to feature significant variations between vessels of different sizes, known as the Fåhræus effect [[Barbee & Cokelet, 1971](#); [Gaehtgens, 1980](#)]. Furthermore, there is a inter- and intra-patient variation, which holds especially true for patients with advanced cancer [[Just *et al.*, 2011](#); [Roberts *et al.*, 2011](#)]. Therefore accurate knowledge of the Haematocrit, possibly from individual measurement, is of great importance for absolute and relative estimates of haemodynamic parameters. Since an individual HCT measurement is cheaper and easier to accomplish than an individual AIF measurement, it might be a viable strategy for the improvement of haemodynamic parameter accuracy.

3. The benefit from higher SNRs for the precision of K^{trans} estimates decreases

7. DISCUSSION AND CONCLUSION

heavily for higher SNRs (see Fig. 6.15), such that SNRs higher than 50 yield an improvement in the c_v on the order of 1%. Merely the 2CXM benefits from significantly from SNRs higher than 50 by means of its precision and its accuracy. Opposed to all other models under investigation it features a consistent K^{trans} underestimation for SNRs below 100 (see Fig. 6.14). Overall the 2CXM is the only model that benefits significantly from SNRs larger than 50.

Furthermore a surprisingly high precision for estimates from the DPM has been observed. Despite its lack of physical motivation and its limited accuracy, this is a clear advantage of this model compared to the other four-parameter models (2CXM, ATHM).

4. AIC and BIC weighted parameter estimates that combine the estimates of all 5 models under investigation perform roughly as good as the best model in each case. This is true for their accuracy as well as for their precision. These results contradict, what [Luypaert *et al.*, 2012] conclude in one of the few available studies of this issue. Choosing AIC or BIC weighted averages gives overall more accurate and more precise estimates than choosing any of the single models. The mutual performance of AIC and BIC is very similar, with a slightly better accuracy for the AIC, while the BIC features a higher precision.

Future subjects of investigation. As already done for a more limited scope by [Aerts *et al.* \[2008\]](#) the influence of the injection volume should be analyzed by a procedure, similar to the one that was employed in this study. Furthermore the effects of a different sampling rate , and total acquisition time are of interest. Together with the influence of the SNR, such considerations would yield a more comprehensive set of determinants for the best model choice and give more insights in the benefit of AIC and BIC weighted model averages.

Moreover, the behavior of E and F_p in the four-parameter models should be investigated more closely, in particular for the AIC and BIC weighted averages.

Appendices

Appendix A

Solution of the Rate Equation for the TM

The initial rate equation (see p. 13) is given by:

$$v_e \dot{c}_e(t) = K^{trans}(c_p(t) - c_e(t)) \quad (\text{A.1})$$

where the dot signifies a time derivative. Rearrangement and multiplication by $\exp\left[\frac{K^{trans} \cdot t}{v_e}\right]$ yields:

$$\dot{c}_e \exp\left[\frac{K^{trans} \cdot t}{v_e}\right] + \frac{K^{trans}}{v_e} c_e(t) \exp\left[\frac{K^{trans} \cdot t}{v_e}\right] = \frac{K^{trans}}{v_e} c_p(t) \exp\left[\frac{K^{trans} \cdot t}{v_e}\right]. \quad (\text{A.2})$$

The inverse change rule (or partical integration) gives:

$$\frac{d}{dt} \left(c_e(t) \exp\left[\frac{K^{trans} \cdot t}{v_e}\right] \right) = \frac{K^{trans}}{v_e} c_p(t) \exp\left[\frac{K^{trans} \cdot t}{v_e}\right]. \quad (\text{A.3})$$

By formal integration it is found:

$$c_e(t) = \frac{K^{trans}}{v_e} \int_{const.}^t c_p(t') \exp\left[\frac{-K^{trans} \cdot (t - t')}{v_e}\right] dt'. \quad (\text{A.4})$$

A. SOLUTION OF THE RATE EQUATION FOR THE TM

With the time of enhancement starting at $t' = 0$ and thus choosing the lower integration bound to be 0, the final result is

$$c_e(t) = \frac{K^{trans}}{v_e} \int_0^t c_p(t') \exp \left[\frac{-K^{trans} \cdot (t - t')}{v_e} \right] dt', \quad (\text{A.5})$$

which is identical to eq. (3.5) on p. 13.

Appendix B

Additional Figures

B. ADDITIONAL FIGURES

B.1 Accuracy and Precision for various Injection Speeds

B.1.1 Mouse AIFs, Negligible Vascular Volume

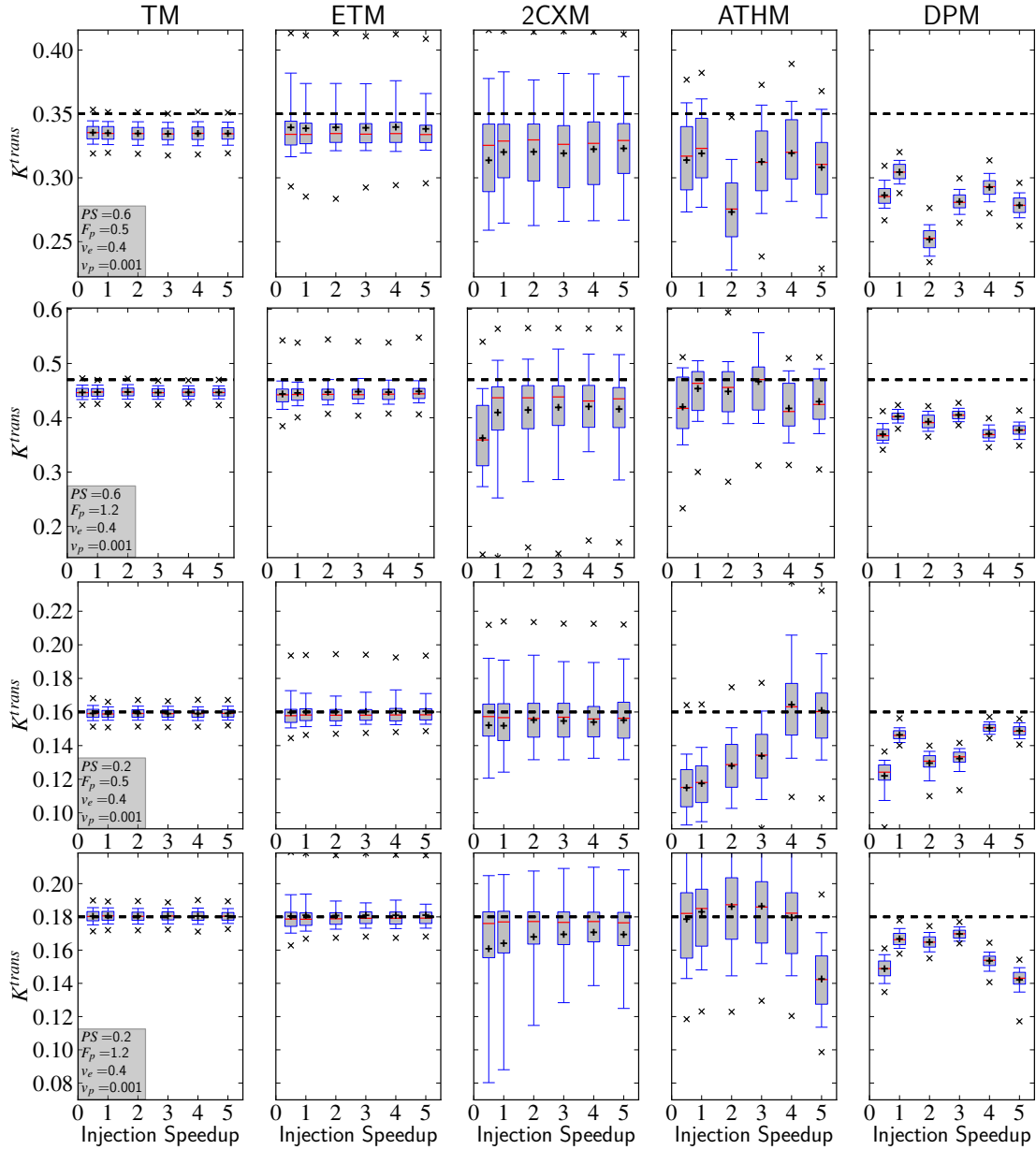


Figure B.1: Dependence of the accuracy and precision of K^{trans} estimates from five different PK models on the injection speed for an AIF in a mouse tail with a negligible vascular volume (SNR = 30).

B.1 Accuracy and Precision for various Injection Speeds

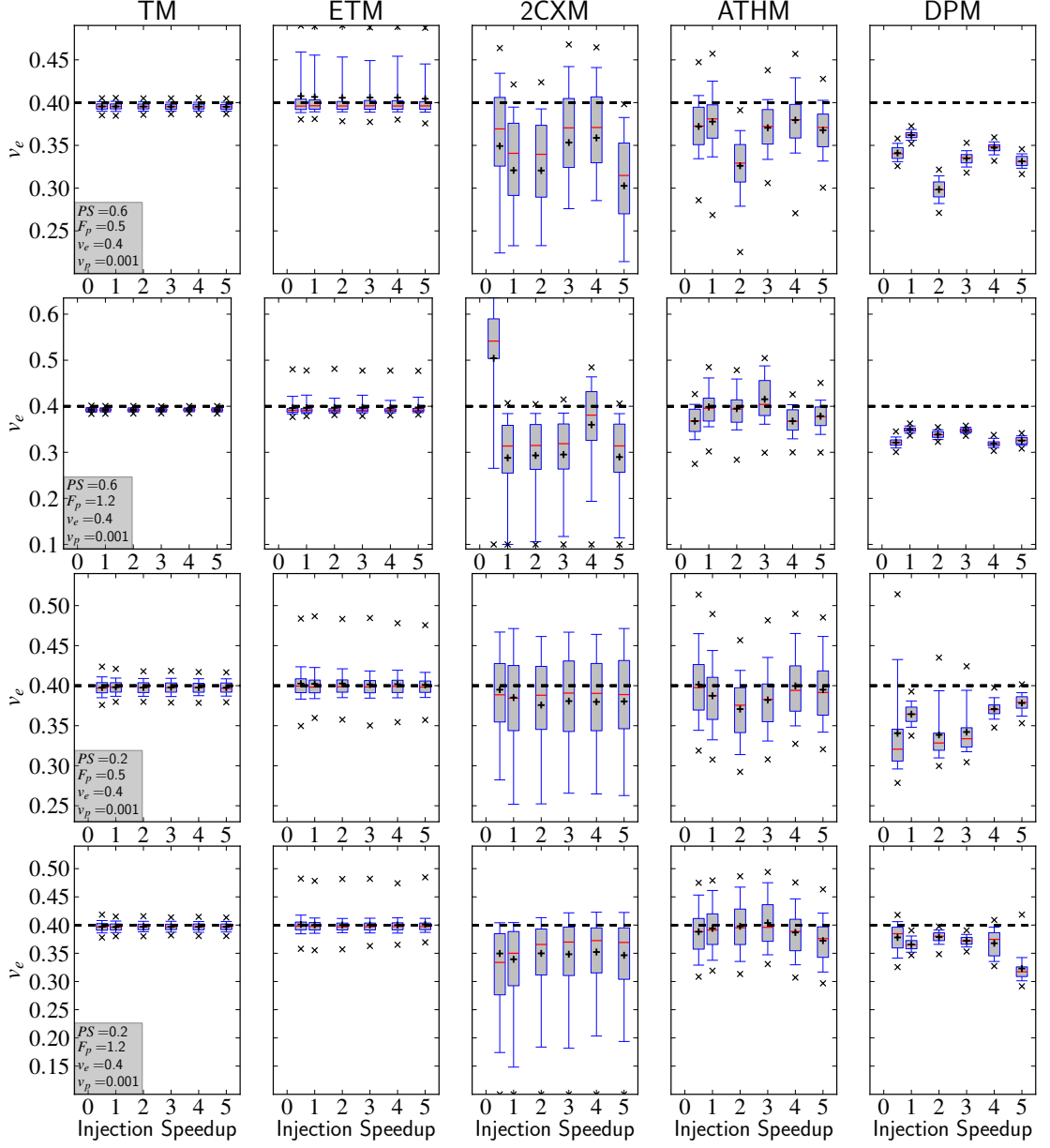


Figure B.2: Dependence of the accuracy and precision of v^e estimates from five different PK models on the injection speed for an AIF in a mouse tail with a negligible vascular volume (SNR = 30).

B. ADDITIONAL FIGURES

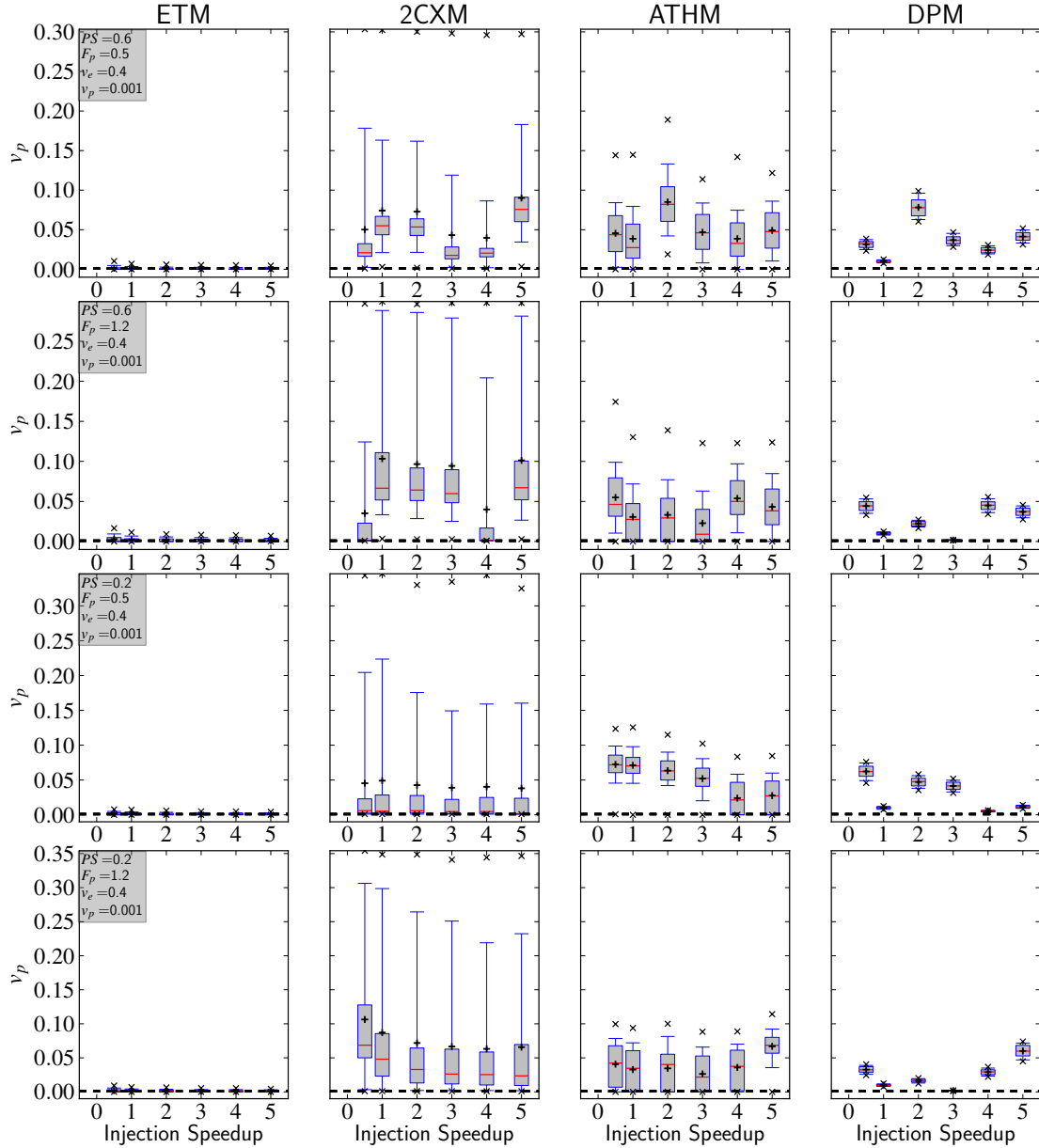


Figure B.3: Dependence of the accuracy and precision of v_p estimates from five different PK models on the injection speed for an AIF in a mouse tail with a negligible vascular volume (SNR = 30).

B.1 Accuracy and Precision for various Injection Speeds

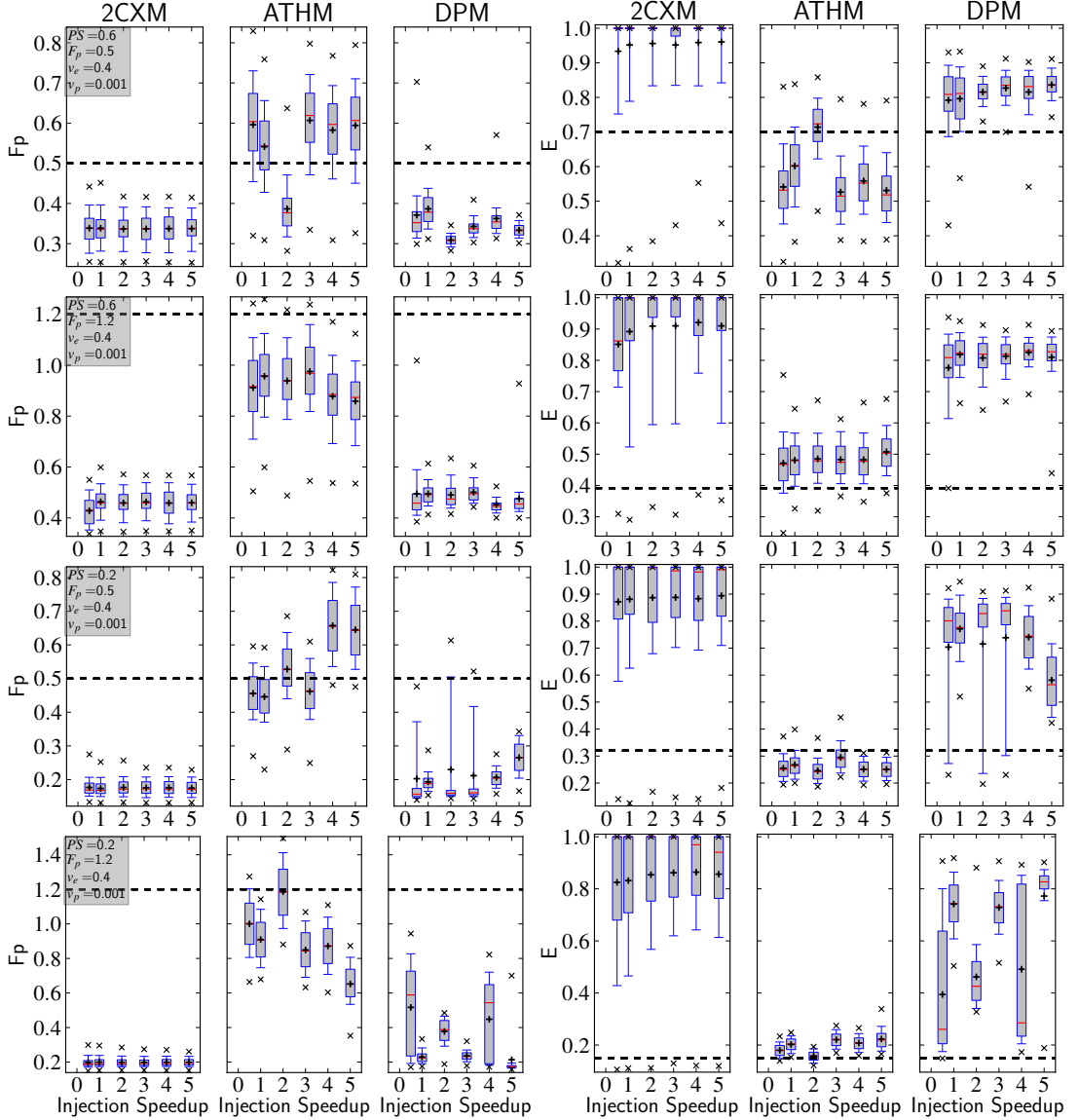


Figure B.4: Dependence of the accuracy and precision of the blood flow F_p and the extraction fraction E estimates from 2CXM and ATHM on the injection speed for a AIF in a mouse tail with an insignificant vascular volume (SNR = 30).

B. ADDITIONAL FIGURES

B.1.2 Human AIFs, significant Vascular Volume

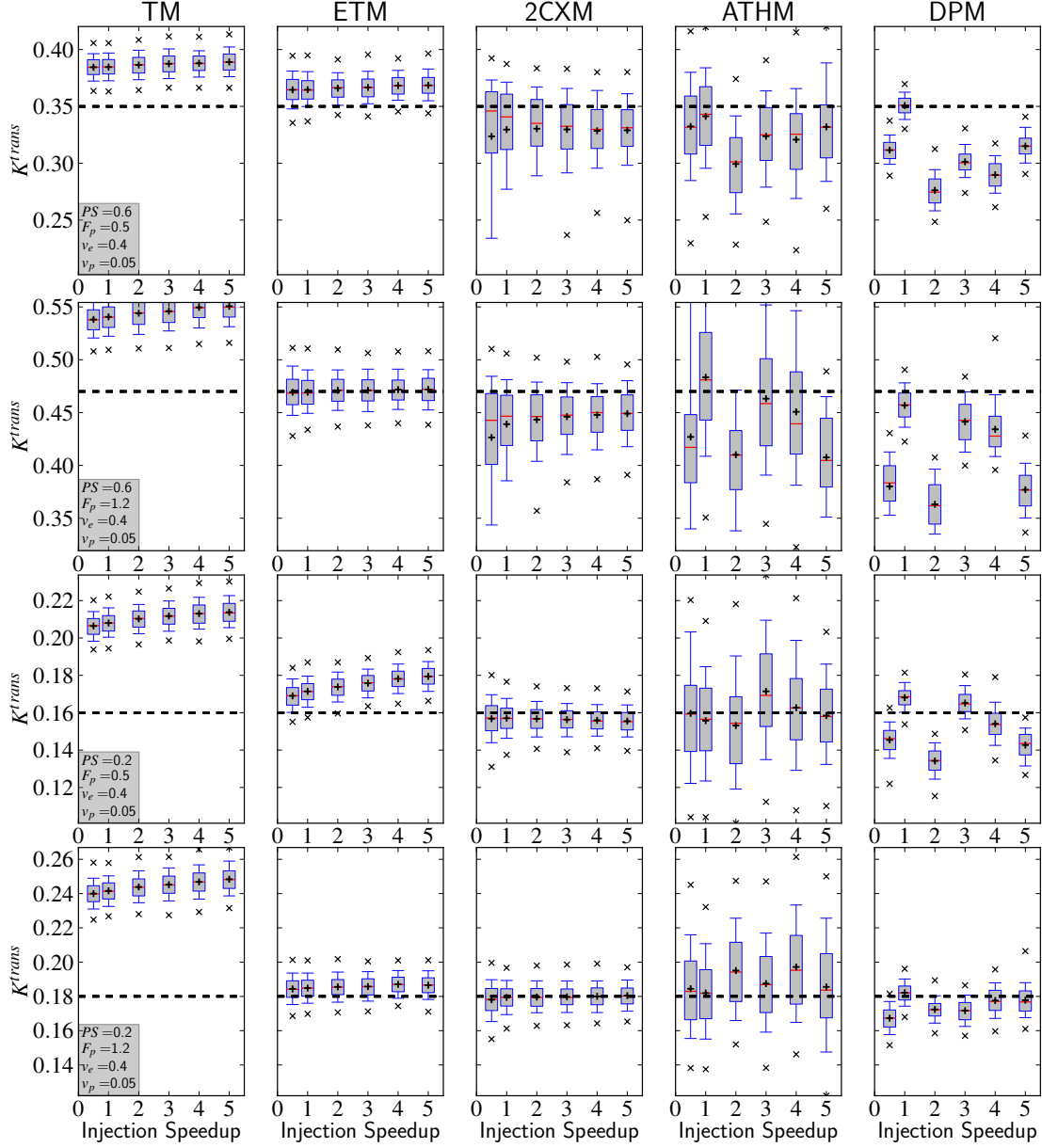


Figure B.5: Dependence of the accuracy and precision of K^{trans} estimates from five different PK models on the injection speedup for a human AIF with a significant vascular volume (SNR = 30).

B.1 Accuracy and Precision for various Injection Speeds

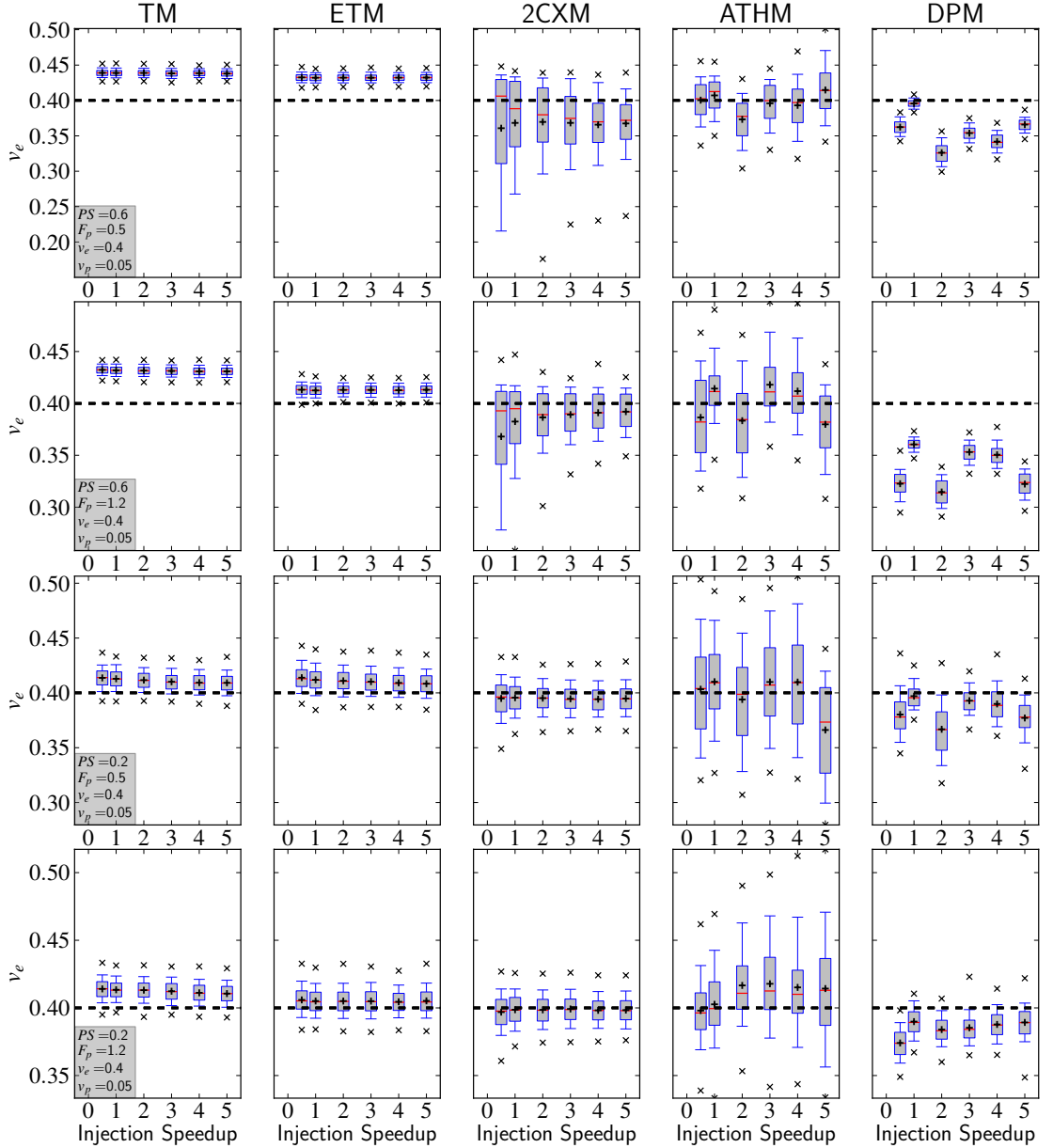


Figure B.6: Dependence of the accuracy and precision of v^e estimates from five different PK models on the injection speed for a human AIF with a significant vascular volume (SNR = 30).

B. ADDITIONAL FIGURES

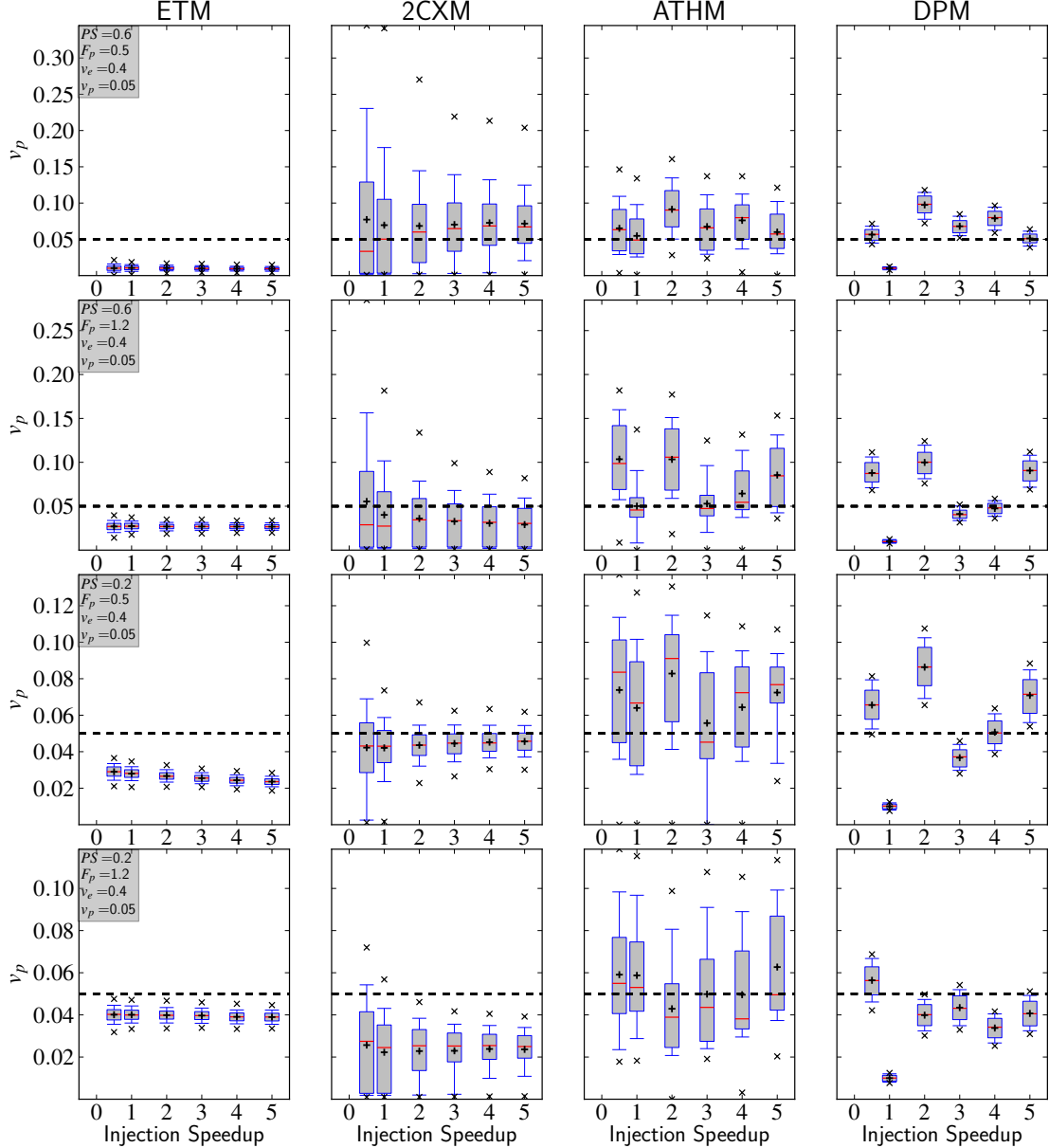


Figure B.7: Dependence of the accuracy and precision of v^p estimates from five different PK models on the injection speedup for a human AIF with a significant vascular volume (SNR = 30).

B.1 Accuracy and Precision for various Injection Speeds

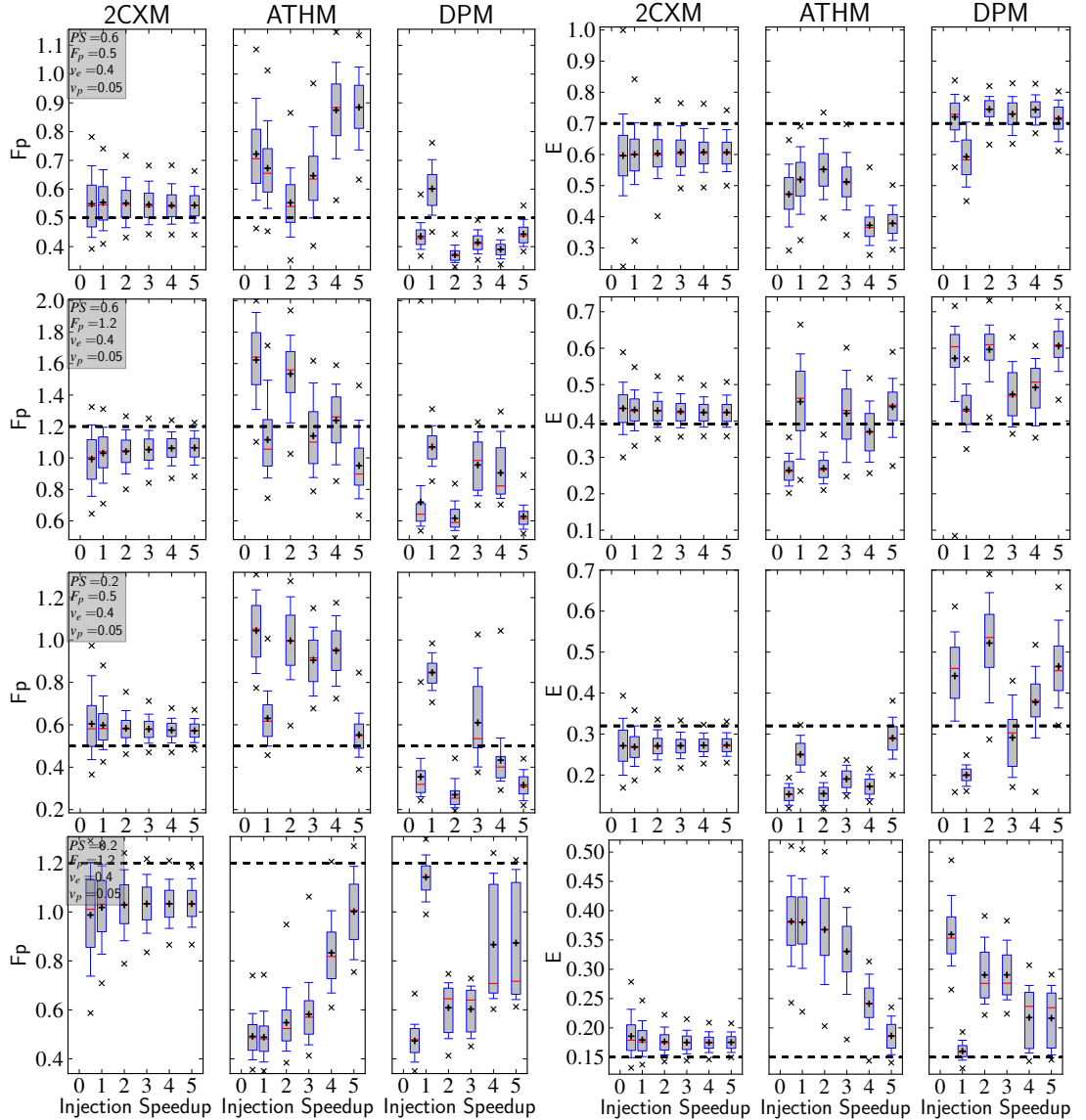


Figure B.8: Dependence of the accuracy and precision of the blood flow F_p and the extraction fraction E estimates from 2CXM and ATHM on the injection speed for a human AIF with a significant vascular volume (SNR = 30).

B. ADDITIONAL FIGURES

B.1.3 Human AIFs, negligible Vascular Volume

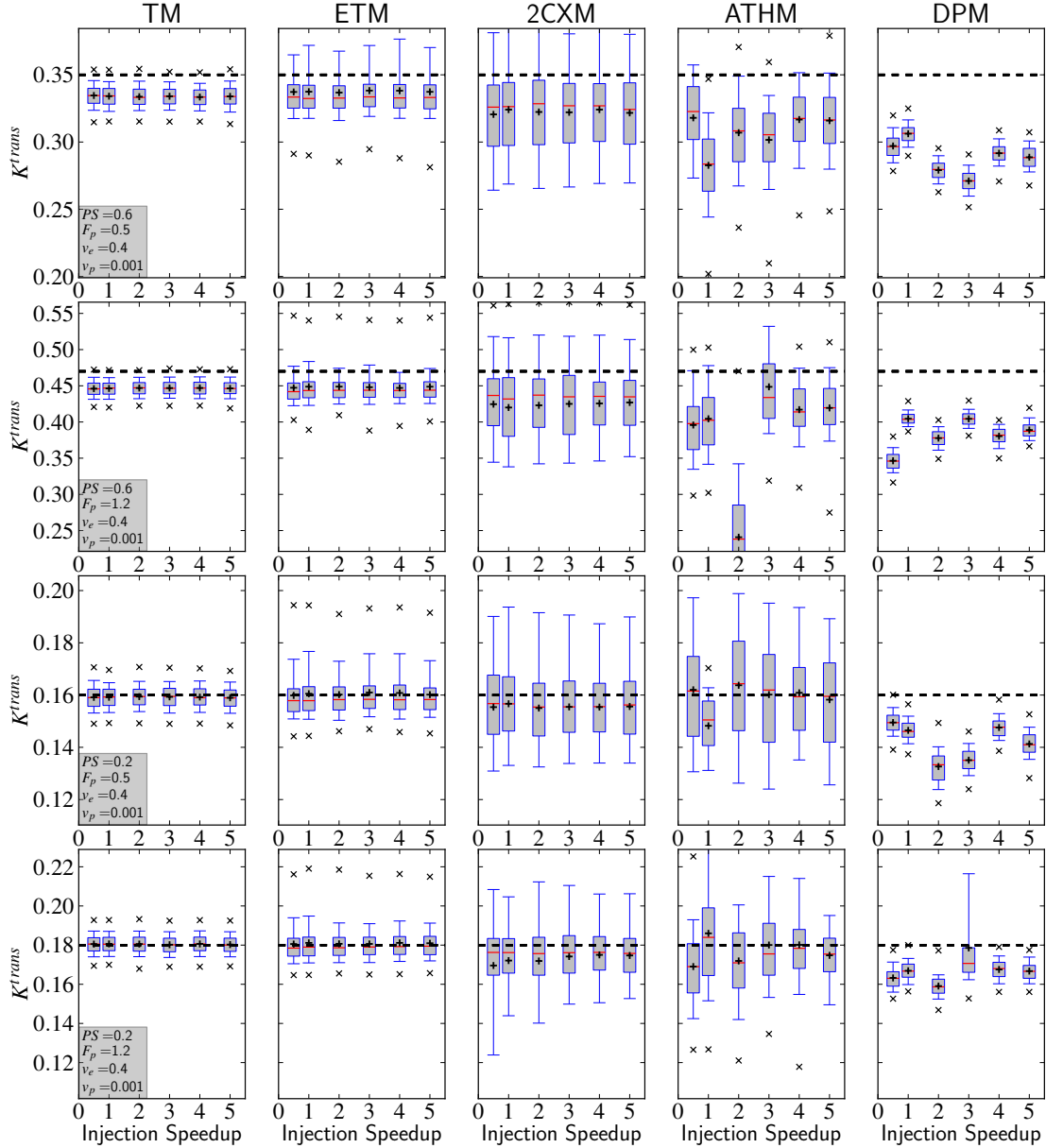


Figure B.9: Dependence of the accuracy and precision of K^{trans} estimates from five different PK models on the injection speed for a human AIF with a negligible vascular volume (SNR = 30).

B.1 Accuracy and Precision for various Injection Speeds

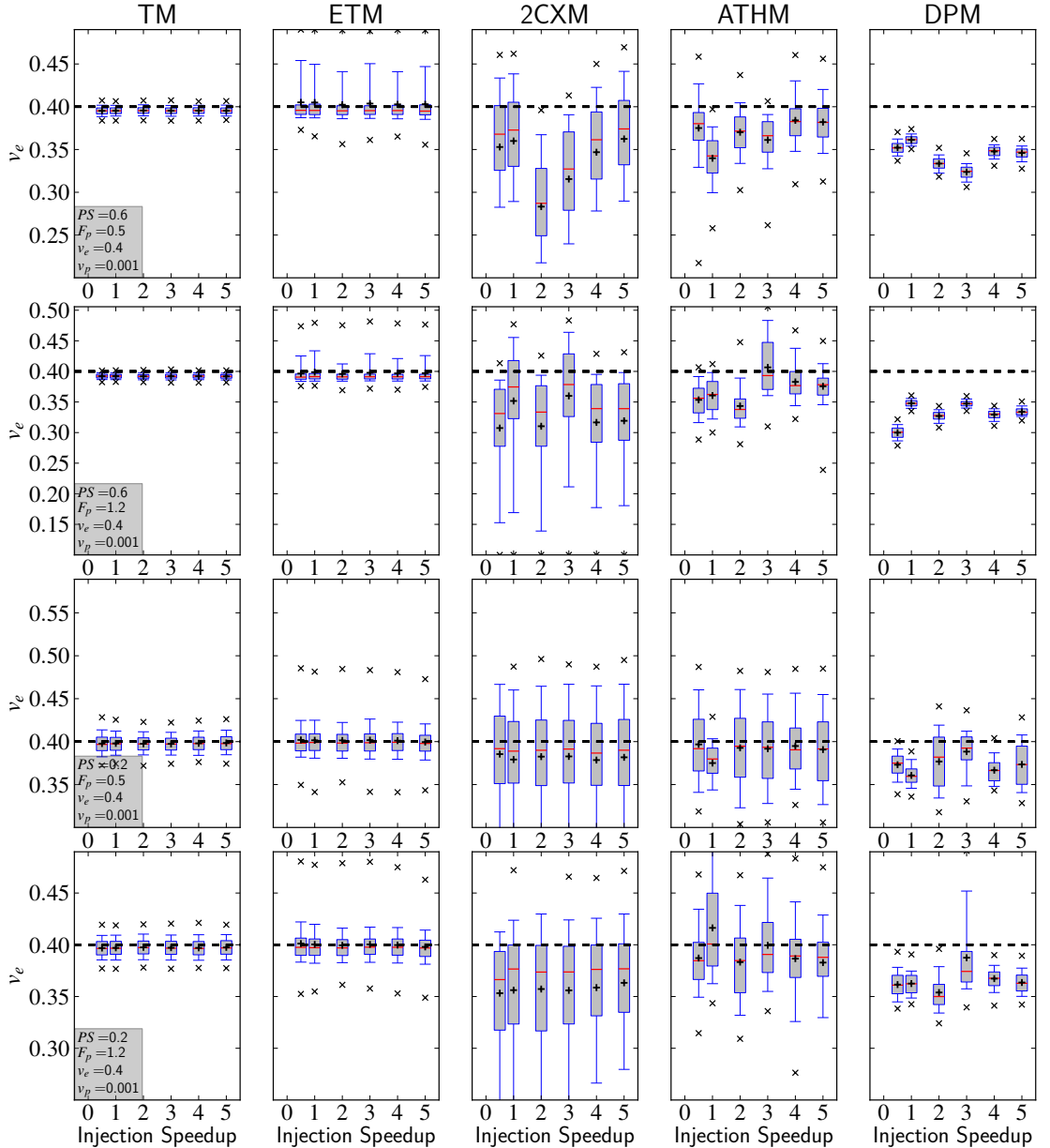


Figure B.10: Dependence of the accuracy and precision of v^e estimates from five different PK models on the injection speed for a human AIF with a negligible vascular volume (SNR = 30).

B. ADDITIONAL FIGURES

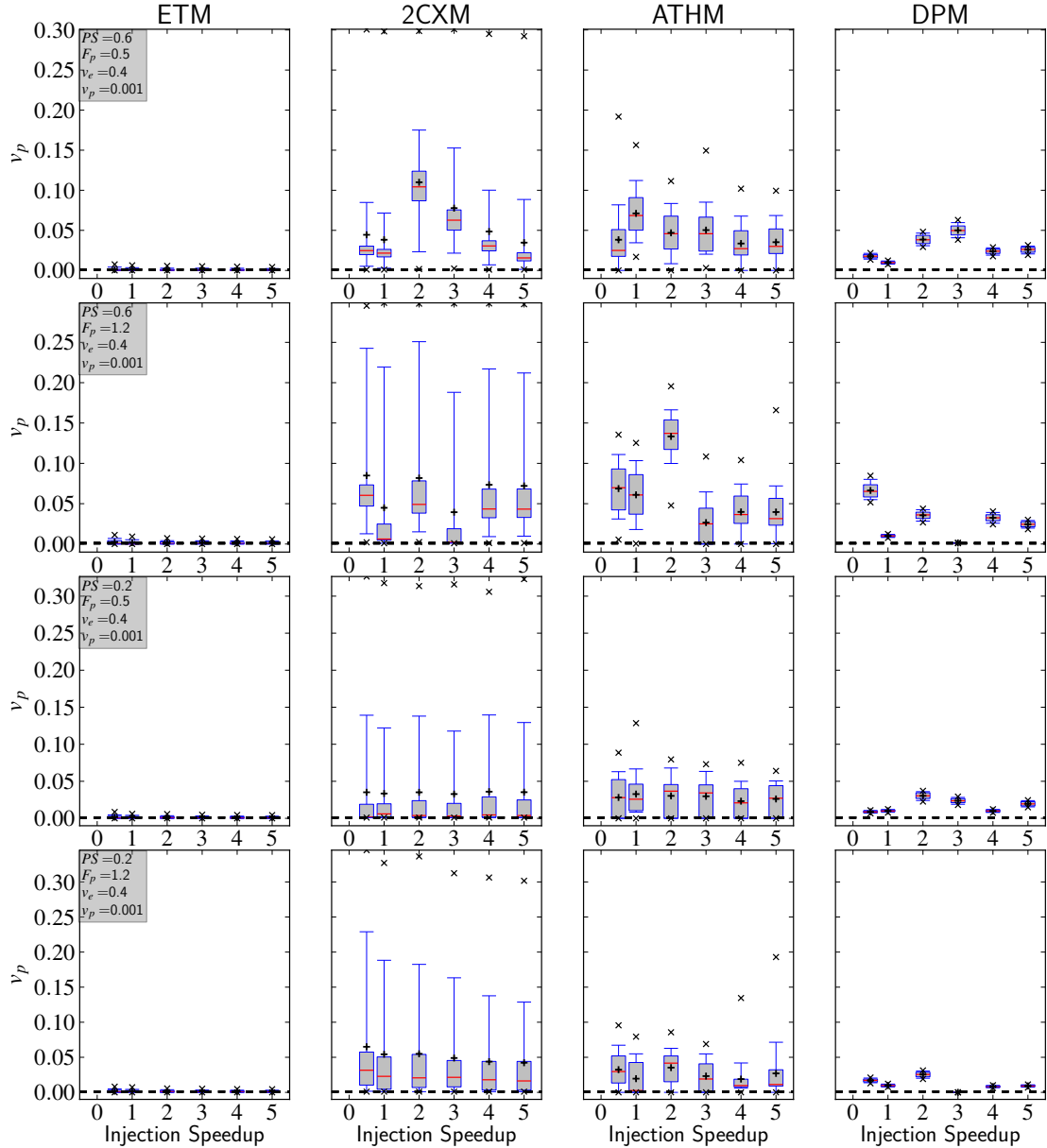


Figure B.11: Dependence of the accuracy and precision of v^p estimates from five different PK models on the injection speedup for a human AIF with a negligible vascular volume (SNR = 30).

B.1 Accuracy and Precision for various Injection Speeds

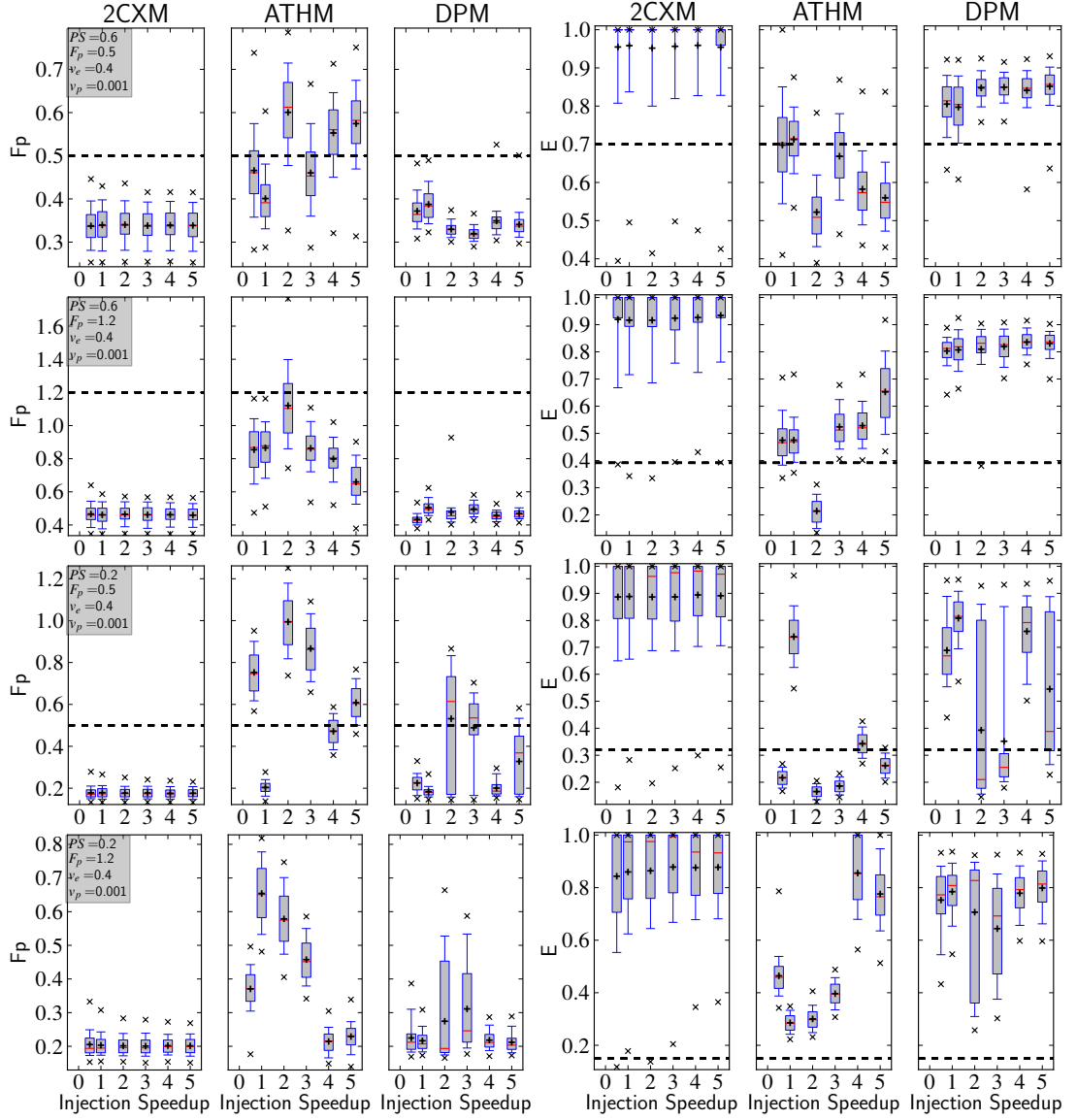


Figure B.12: Dependence of the accuracy and precision of the blood flow F_p and the extraction fraction E estimates from 2CXM and ATHM on the injection speed for a human AIF with an insignificant vascular volume (SNR = 30).

B. ADDITIONAL FIGURES

B.2 Accuracy and Precision for Deficient AIFs

B.2.1 Error in the Bolus Arrival Time

Mouse AIF, negligible v_p

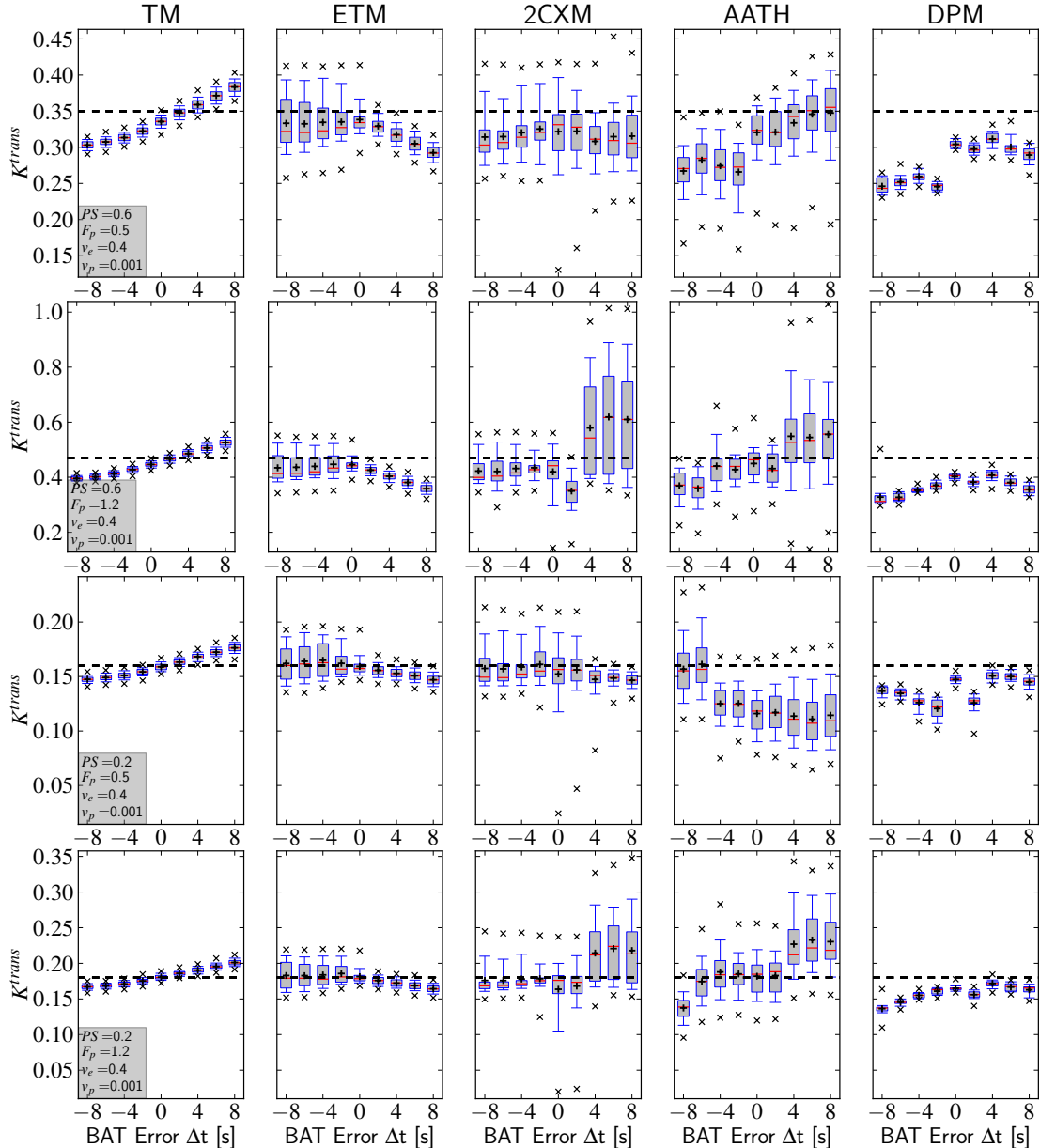


Figure B.13: Accuracy and precision in K^{trans} for mouse AIFs with a error in the bolus arrival time. The AIFs are shown in Fig. 4.3 on page 24.

B.2 Accuracy and Precision for Deficient AIFs

Human AIF, significant v_p

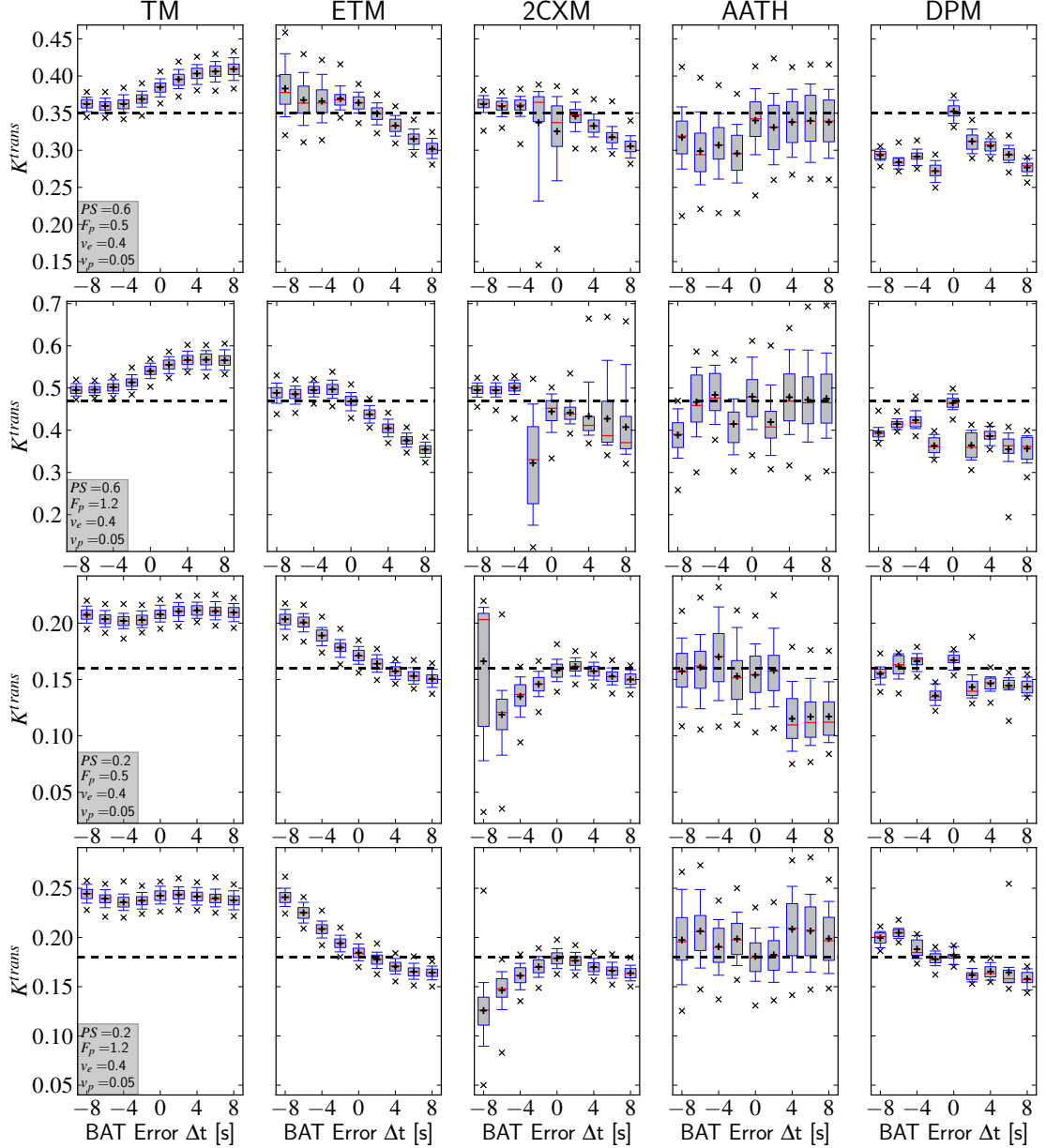


Figure B.14: Accuracy and precision in K^{trans} for human AIFs with a error in the bolus arrival time. The AIFs are shown in Fig. 4.3 on page 24.

B. ADDITIONAL FIGURES

Human AIF, negligible v_p

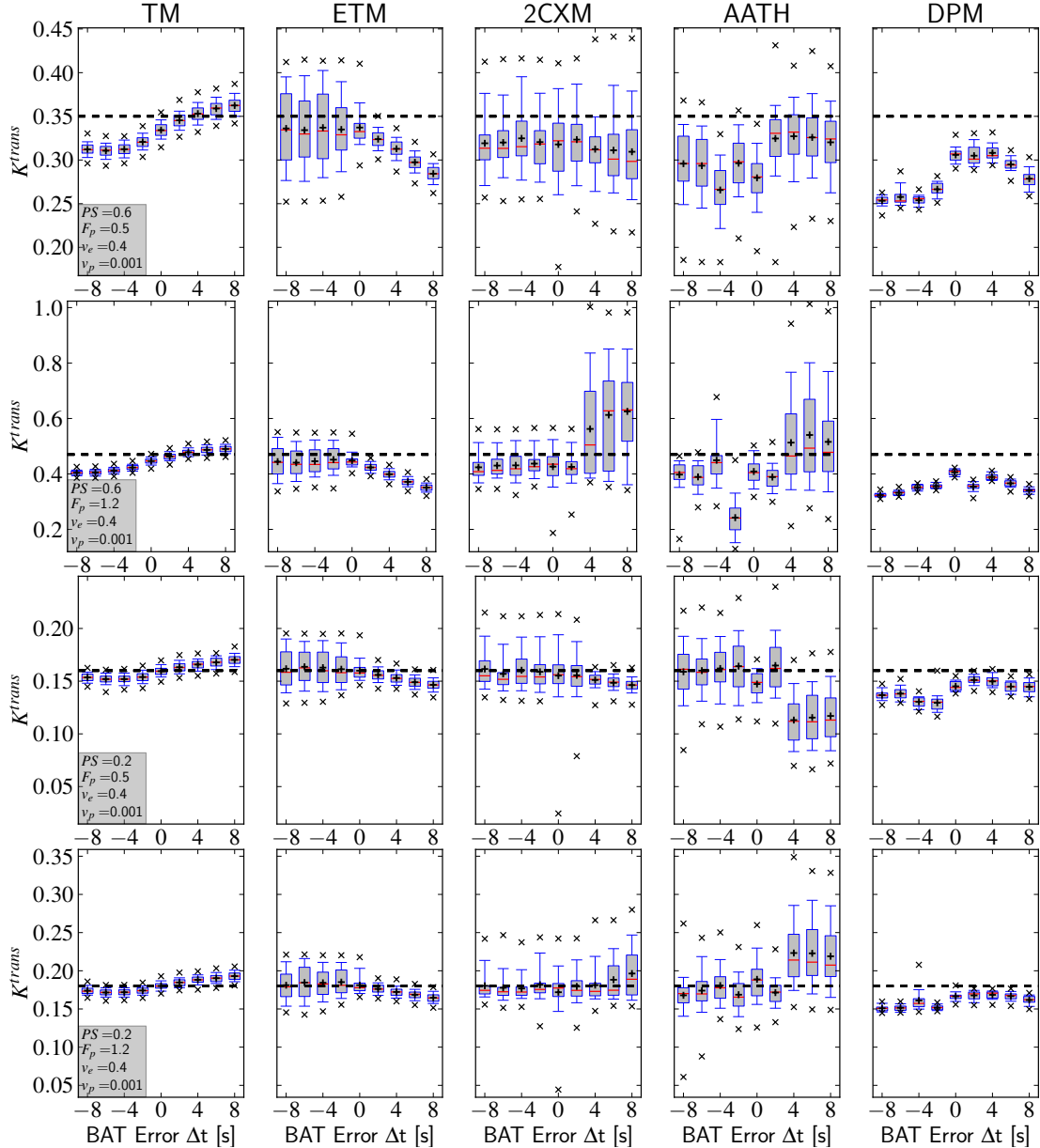


Figure B.15: Accuracy and precision in K^{trans} for human AIFs with a error in the bolus arrival time. The AIFs are shown in Fig. 4.3 on page 24.

B.2.2 Error in the Hematocrit

Mouse AIF, negligible v_p

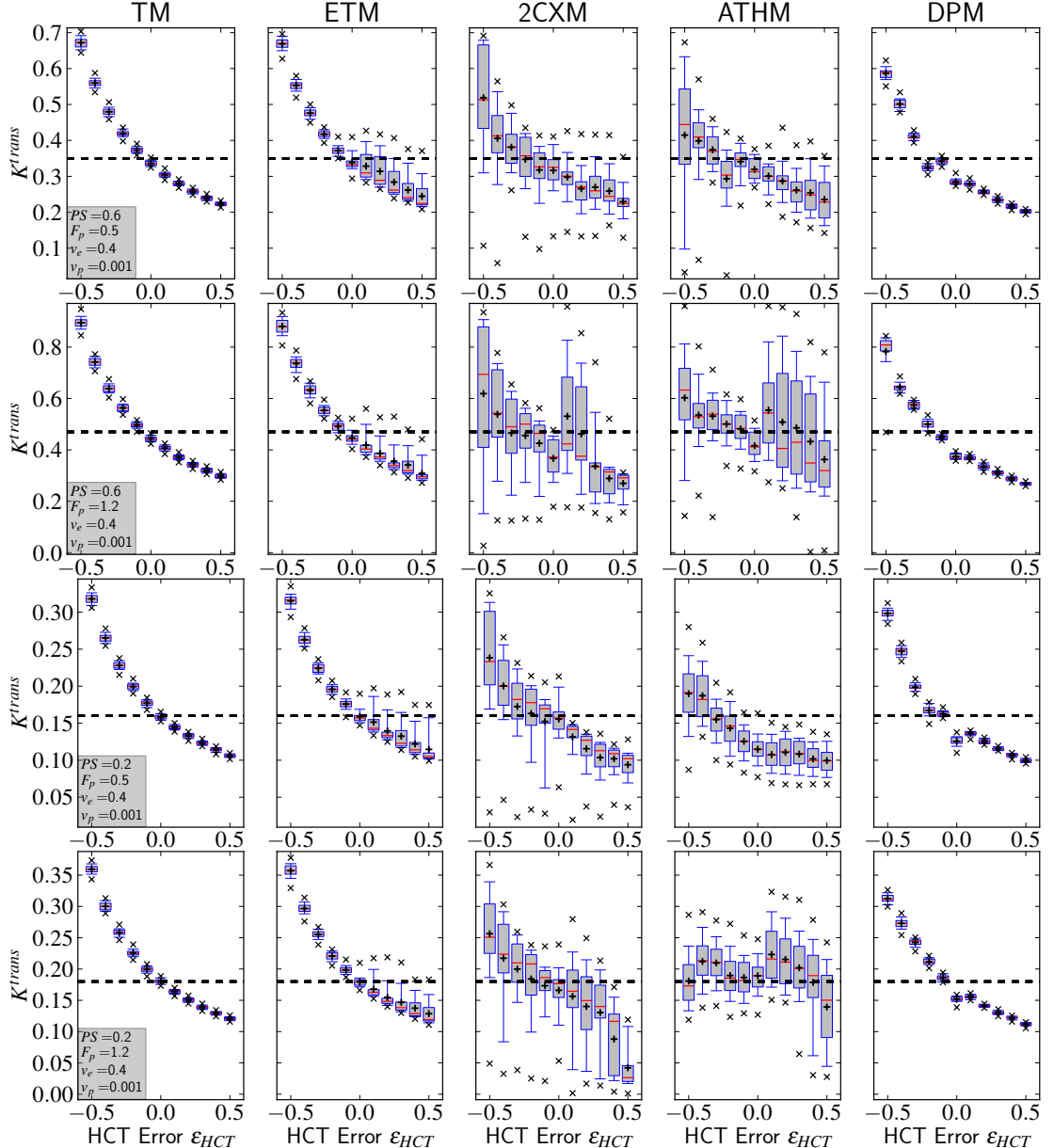


Figure B.16: Accuracy and precision in K^{trans} for mouse AIFs with a error in the hematocrit. The AIFs are shown in Fig. 4.4 on page 25.

B. ADDITIONAL FIGURES

Human AIF, negligible v_p

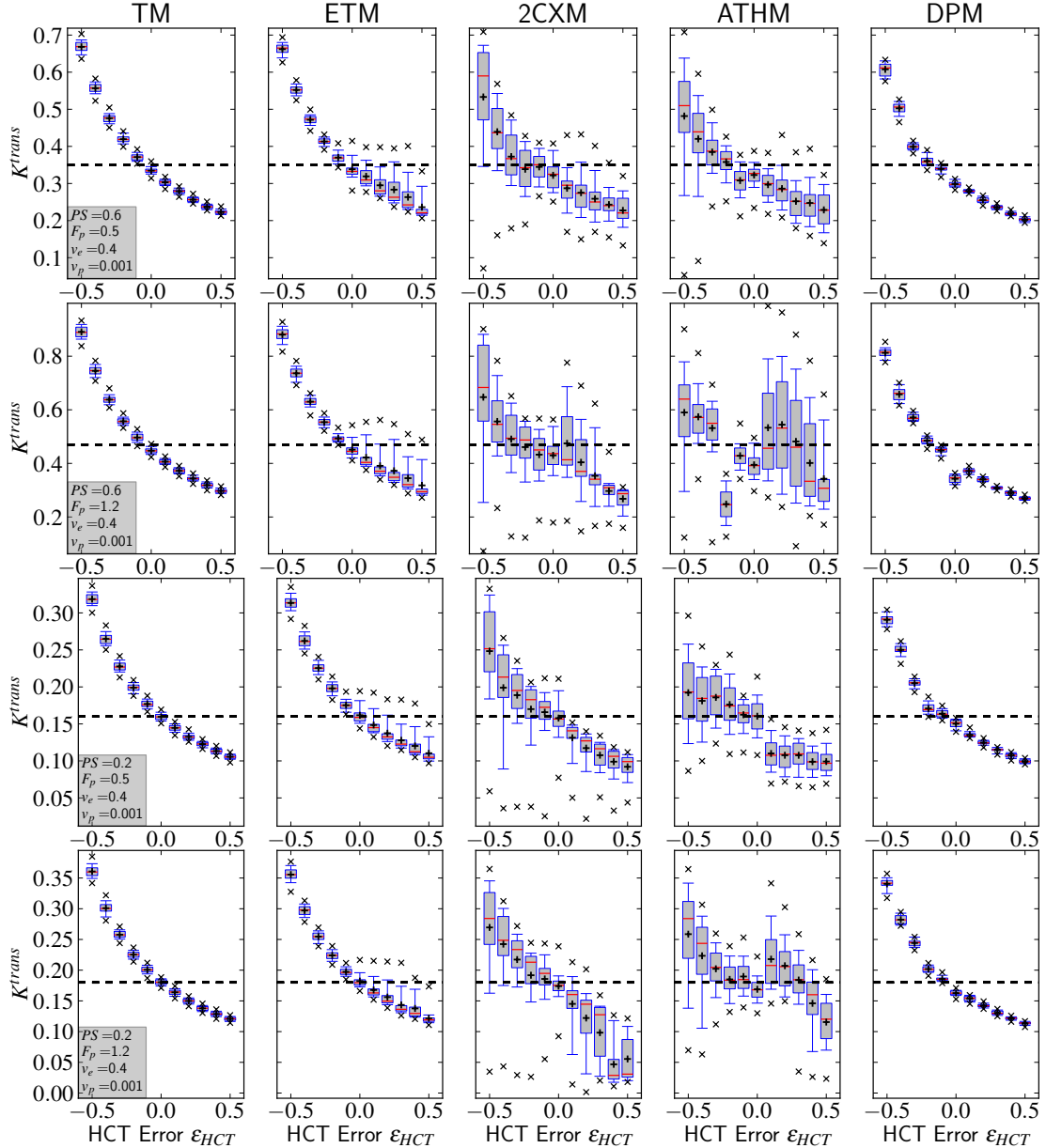


Figure B.17: Accuracy and precision in K^{trans} for human AIFs with a error in the hematocrit. The AIFs are shown in Fig. 4.4 on page 25.

B.2 Accuracy and Precision for Deficient AIFs

B.2.3 Error in the Injection Rate

Mouse AIF, negligible v_p

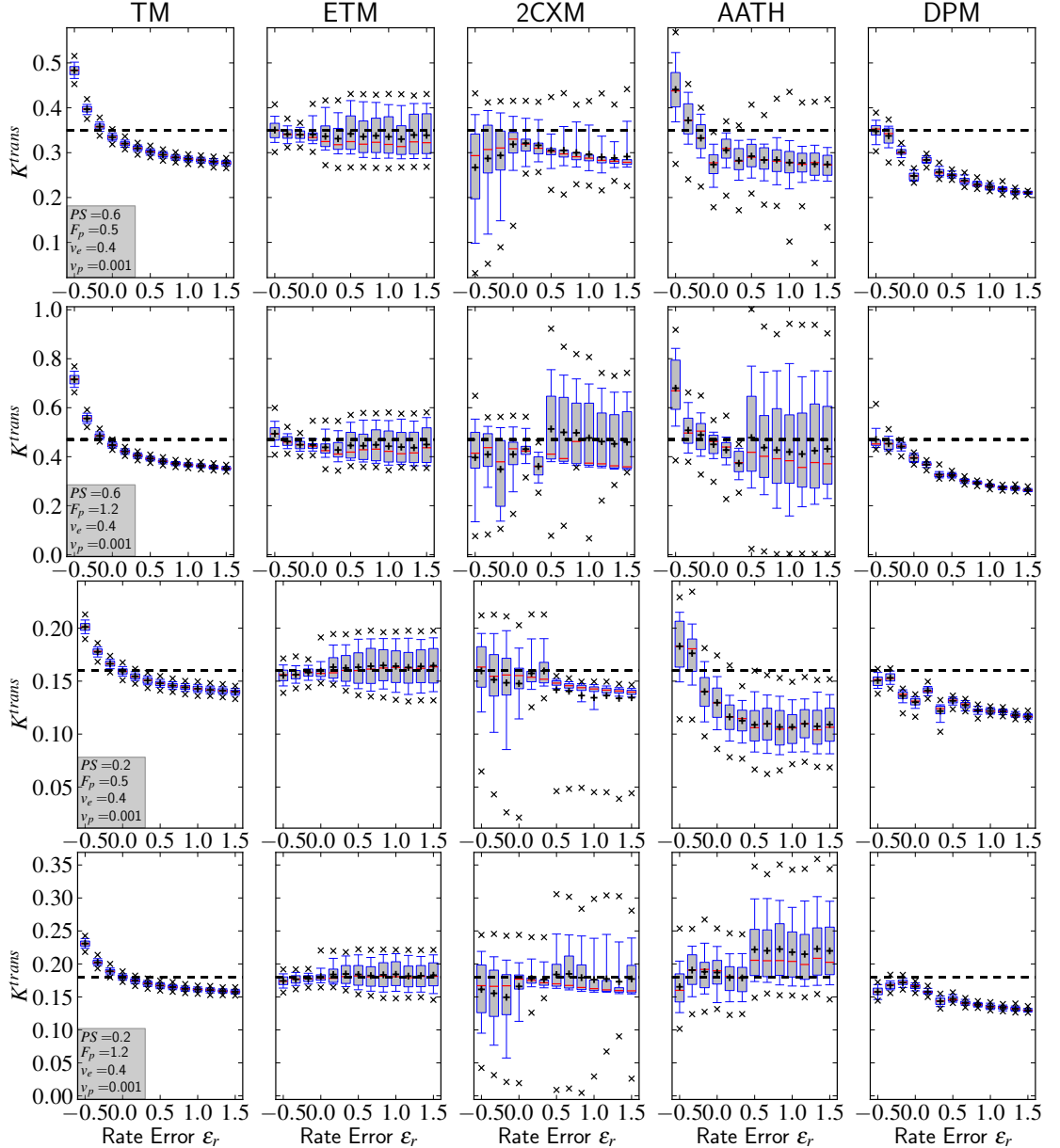


Figure B.18: Accuracy and precision in K^{trans} for mouse AIFs with a error in the rate. The AIFs are shown in Fig. 4.1 on page 21.

B. ADDITIONAL FIGURES

Human AIF, significant v_p

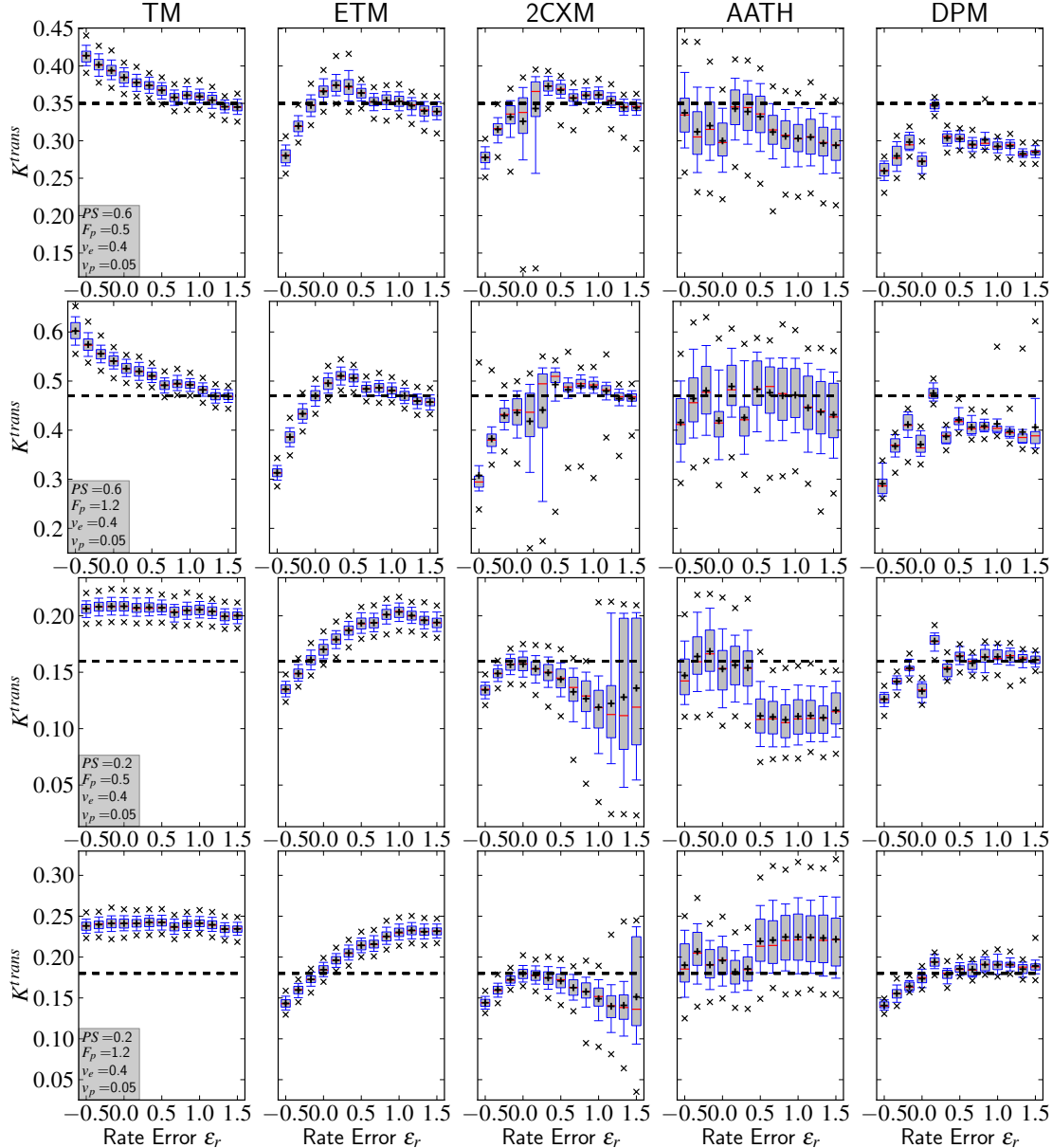


Figure B.19: Accuracy and precision in K^{trans} for human AIFs with a error in the rate.
The AIFs are shown in Fig. 4.1 on page 21.

B.2 Accuracy and Precision for Deficient AIFs

Human AIF, negligible v_p

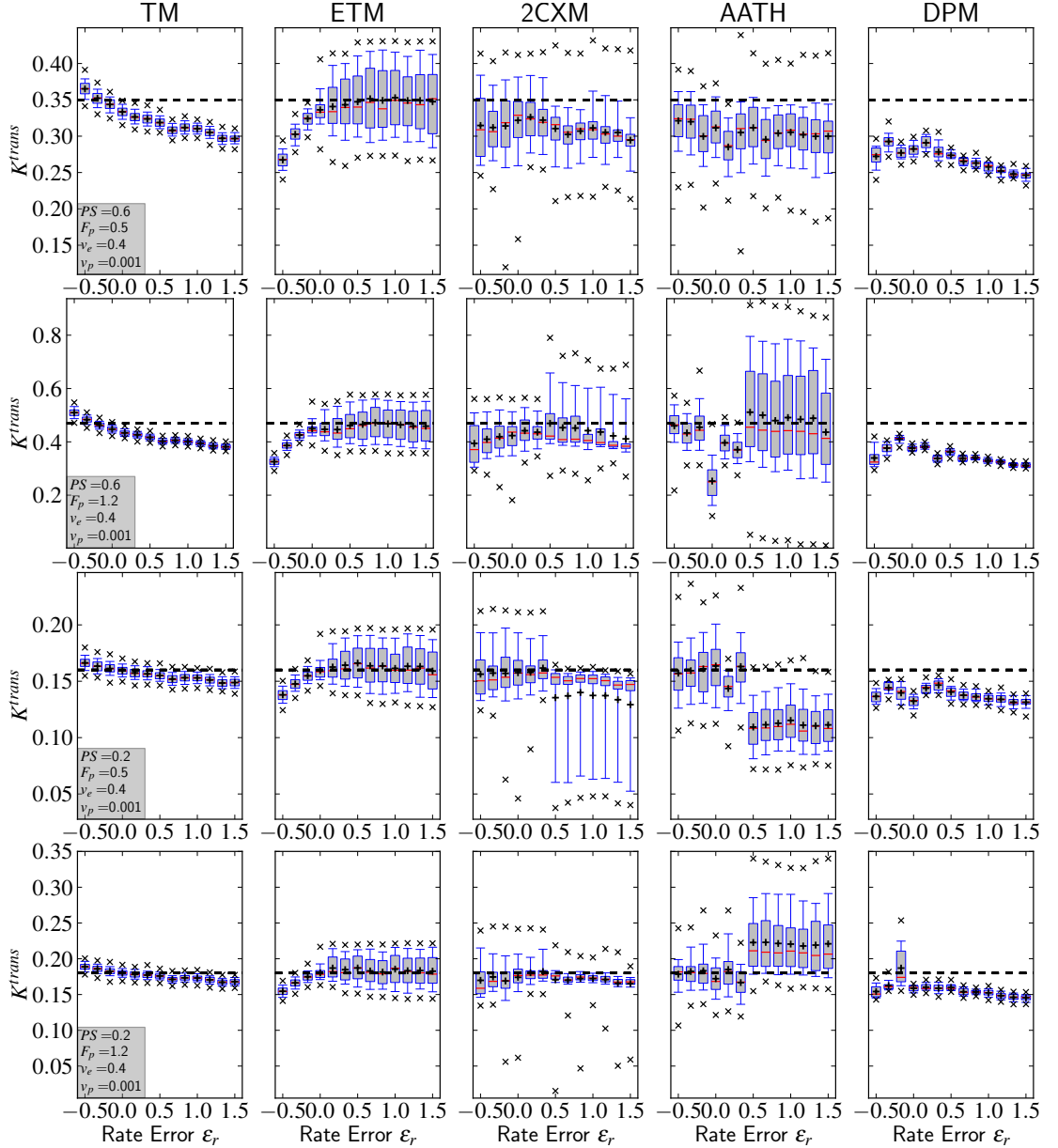


Figure B.20: Accuracy and precision in K^{trans} for human AIFs with a error in the rate. The AIFs are shown in Fig. 4.1 on page 21.

B. ADDITIONAL FIGURES

B.2.4 Error in the Vertical Peak Position

Mouse AIF, negligible v_p

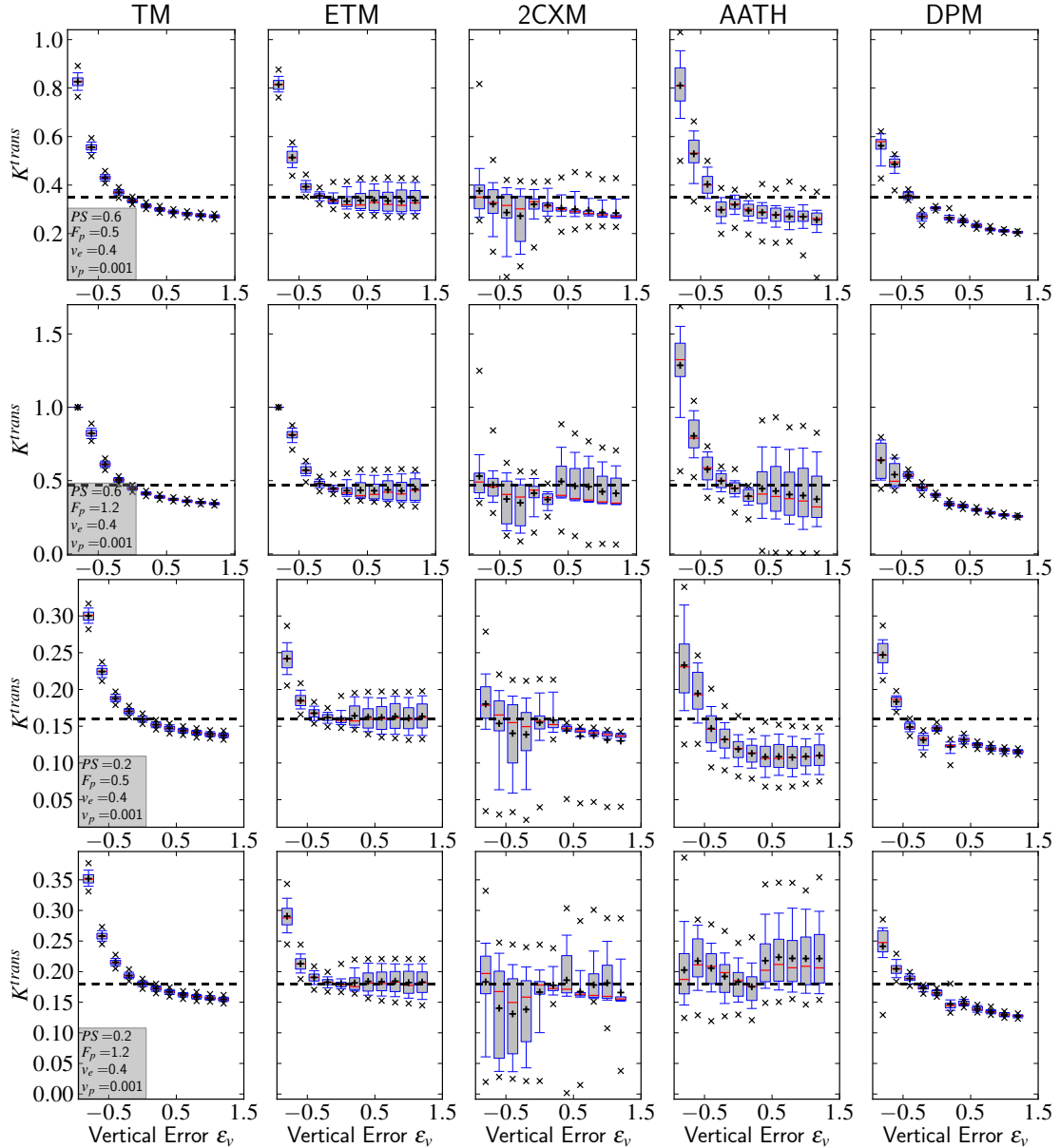


Figure B.21: Accuracy and precision in K^{trans} for mouse AIFs with a error in the vertical peak position. The AIFs are shown in Fig. 4.5 on page 27.

B.2 Accuracy and Precision for Deficient AIFs

Human AIF, significant v_p

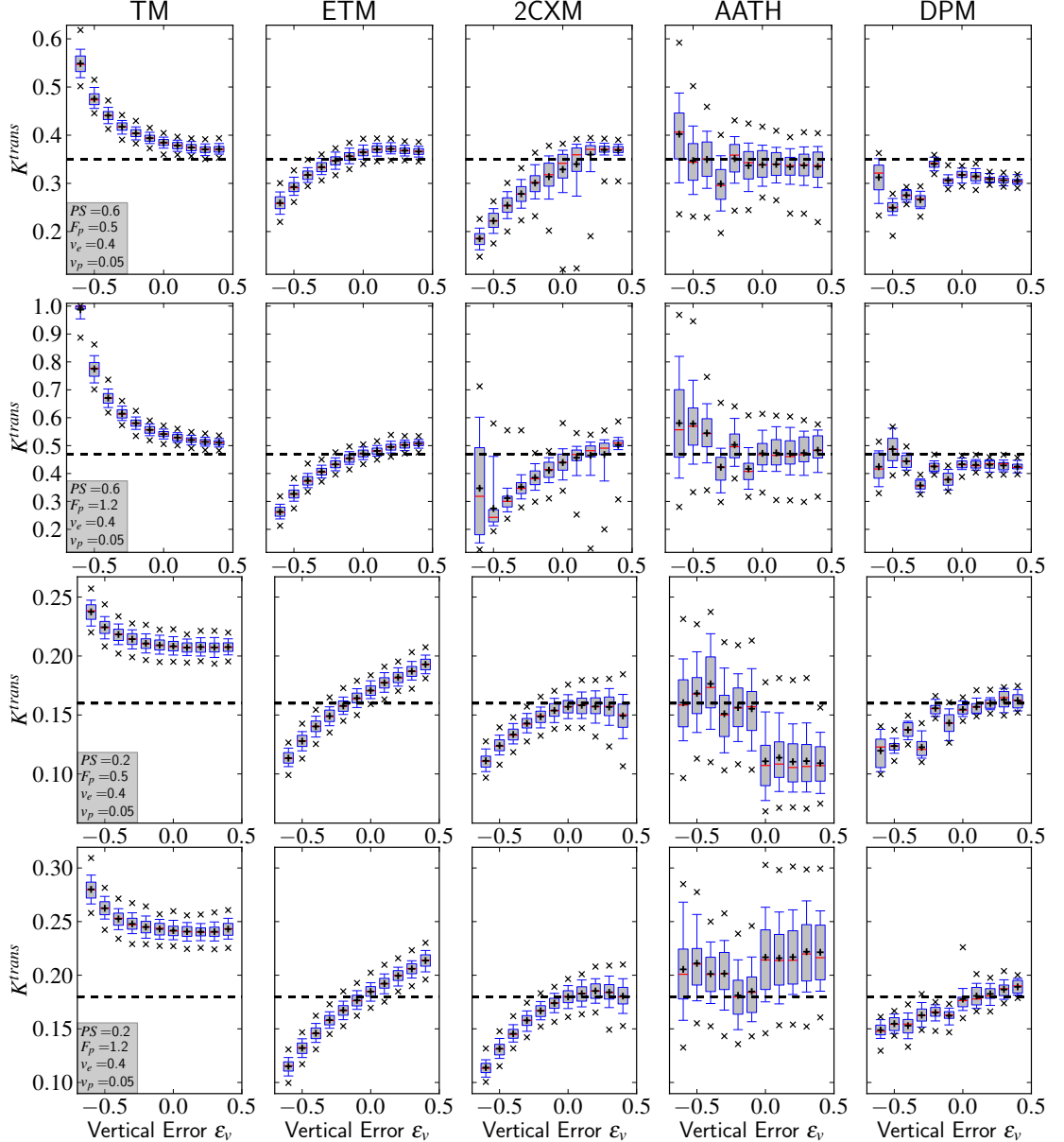


Figure B.22: Accuracy and precision in K^{trans} for human AIFs with a error in the vertical peak position. The AIFs are shown in Fig. 4.5 on page 27.

B. ADDITIONAL FIGURES

Human AIF, negligible v_p

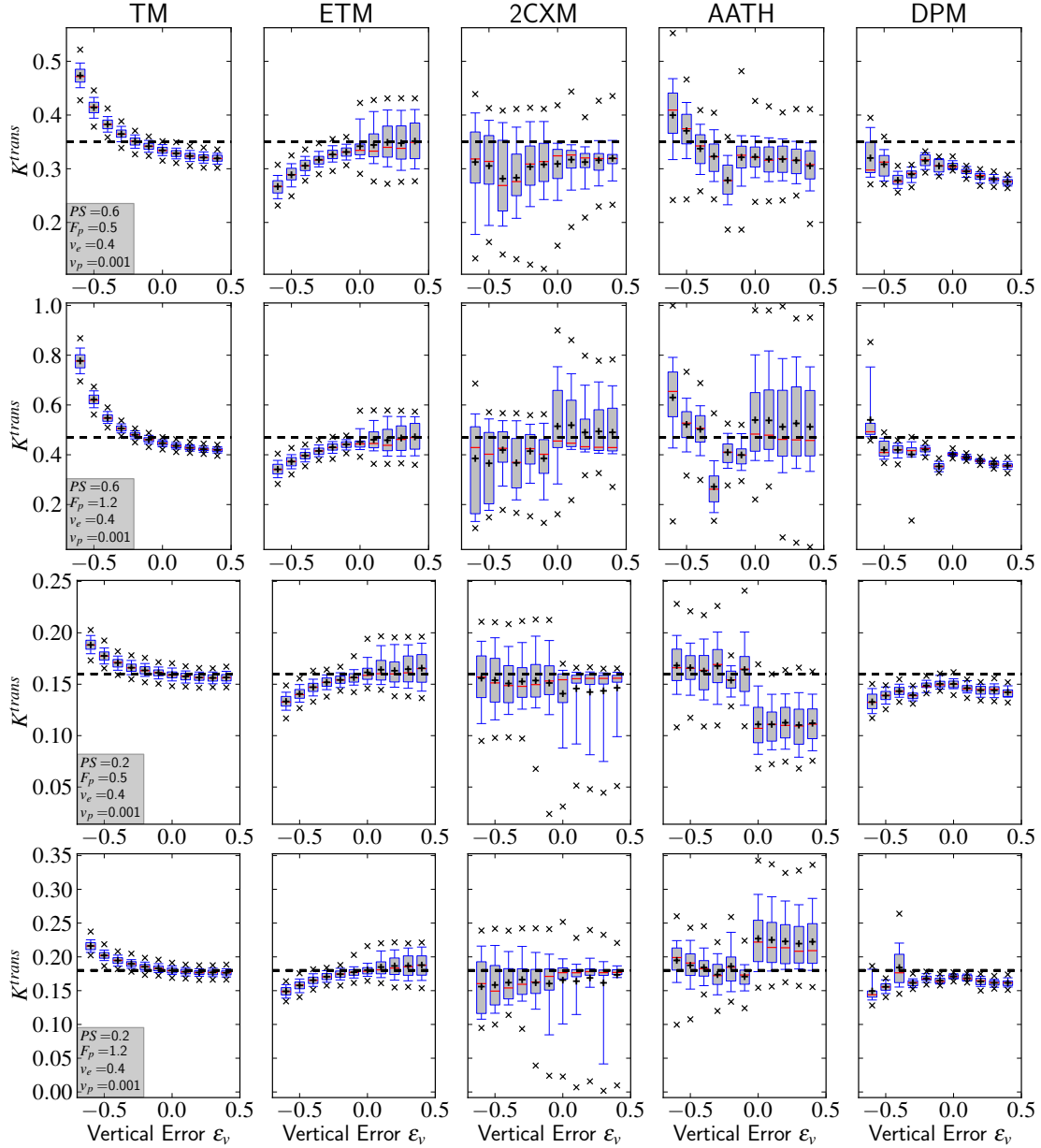


Figure B.23: Accuracy and precision in K^{trans} for human AIFs with a error in the vertical peak position. The AIFs are shown in Fig. 4.5 on page 27.

B.2 Accuracy and Precision for Deficient AIFs

B.2.5 Error in the Horizontal Peak Position

Mouse AIF, negligible v_p

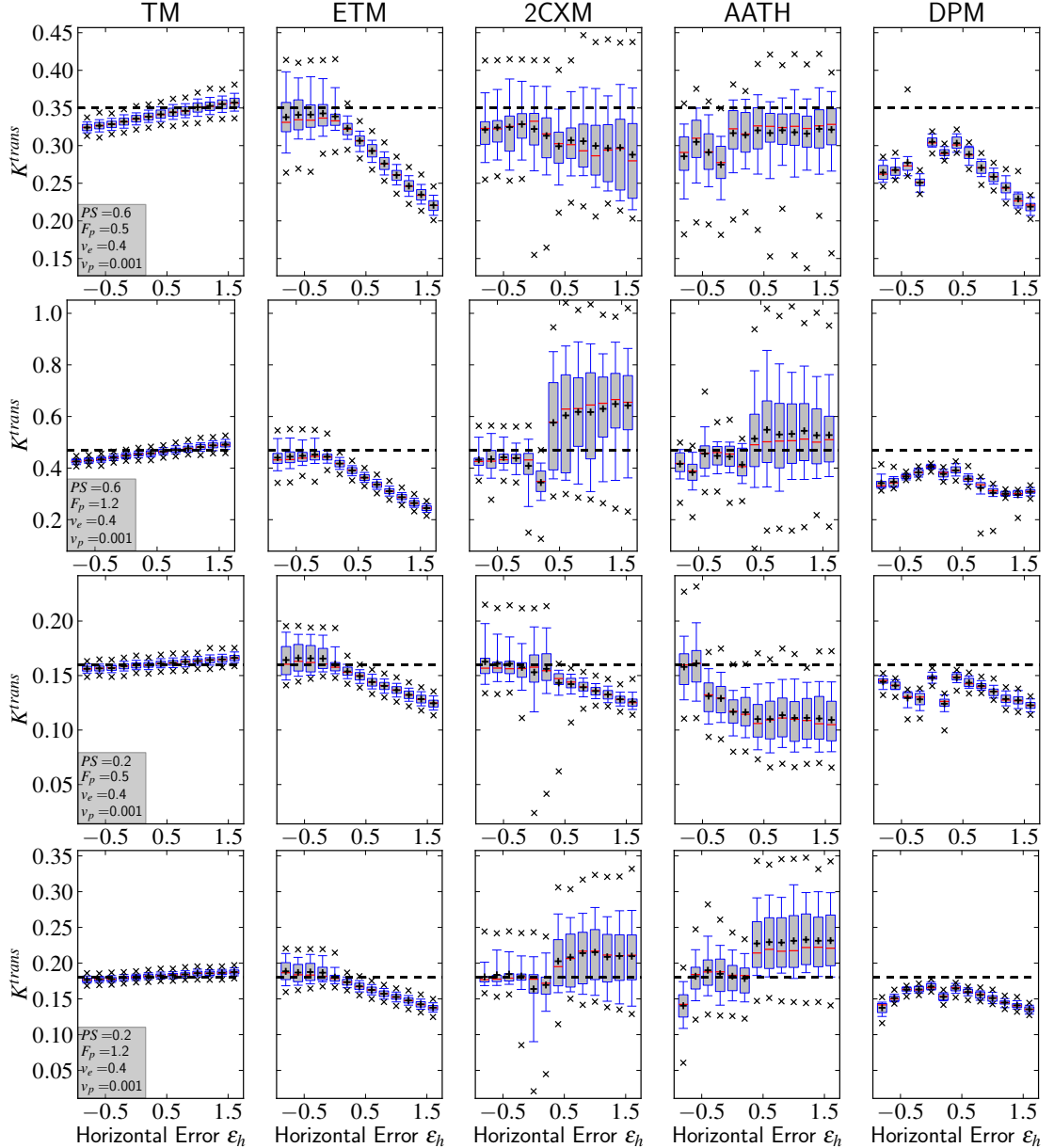


Figure B.24: Accuracy and precision in K^{trans} for mouse AIFs with a error in the horizontal peak position. The AIFs are shown in Fig. 4.5 on page 27.

B. ADDITIONAL FIGURES

Human AIF, significant v_p

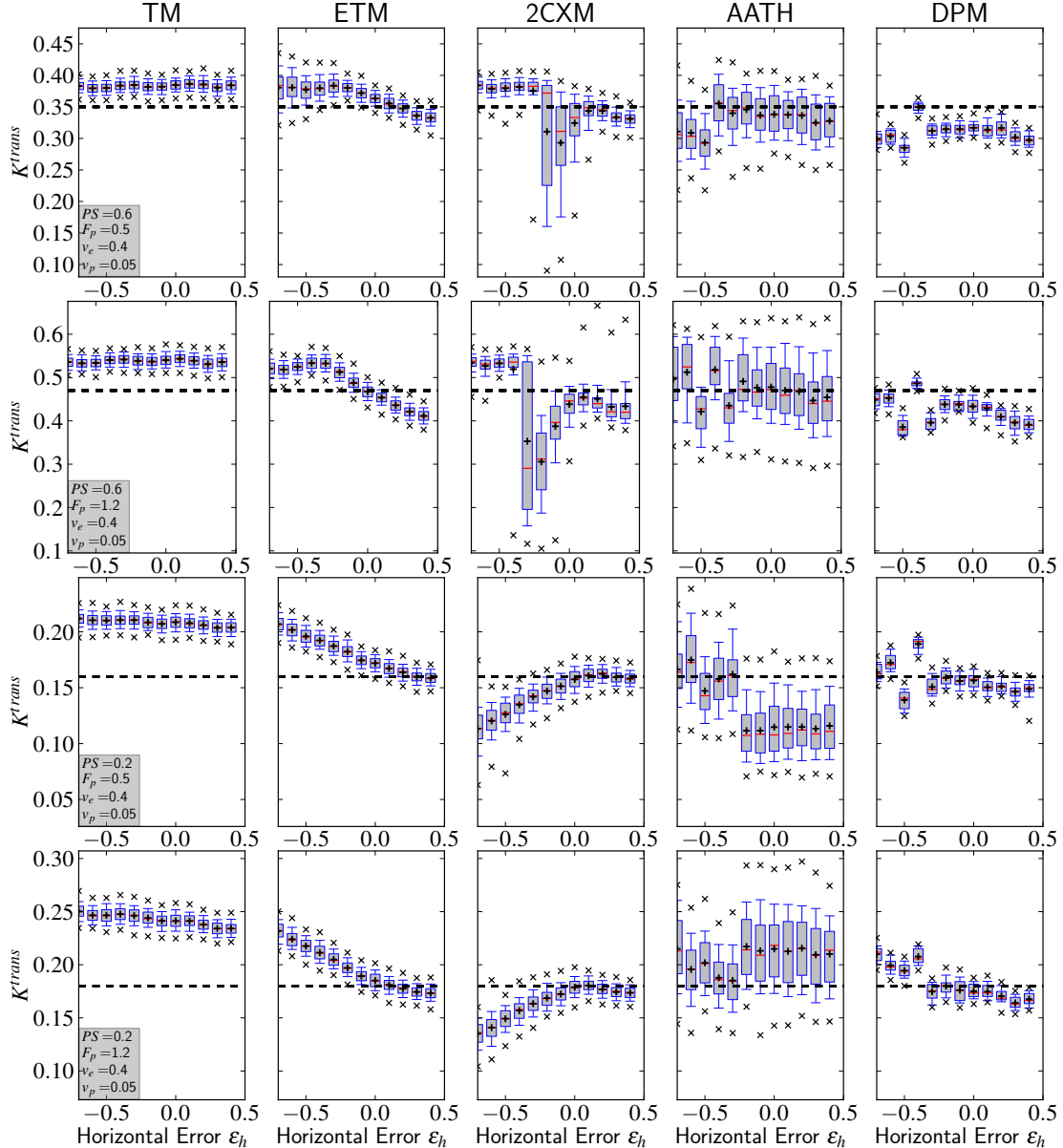


Figure B.25: Accuracy and precision in K^{trans} for human AIFs with an error in the horizontal peak position. The AIFs are shown in Fig. 4.5 on page 27.

B.2 Accuracy and Precision for Deficient AIFs

Human AIF, negligible v_p

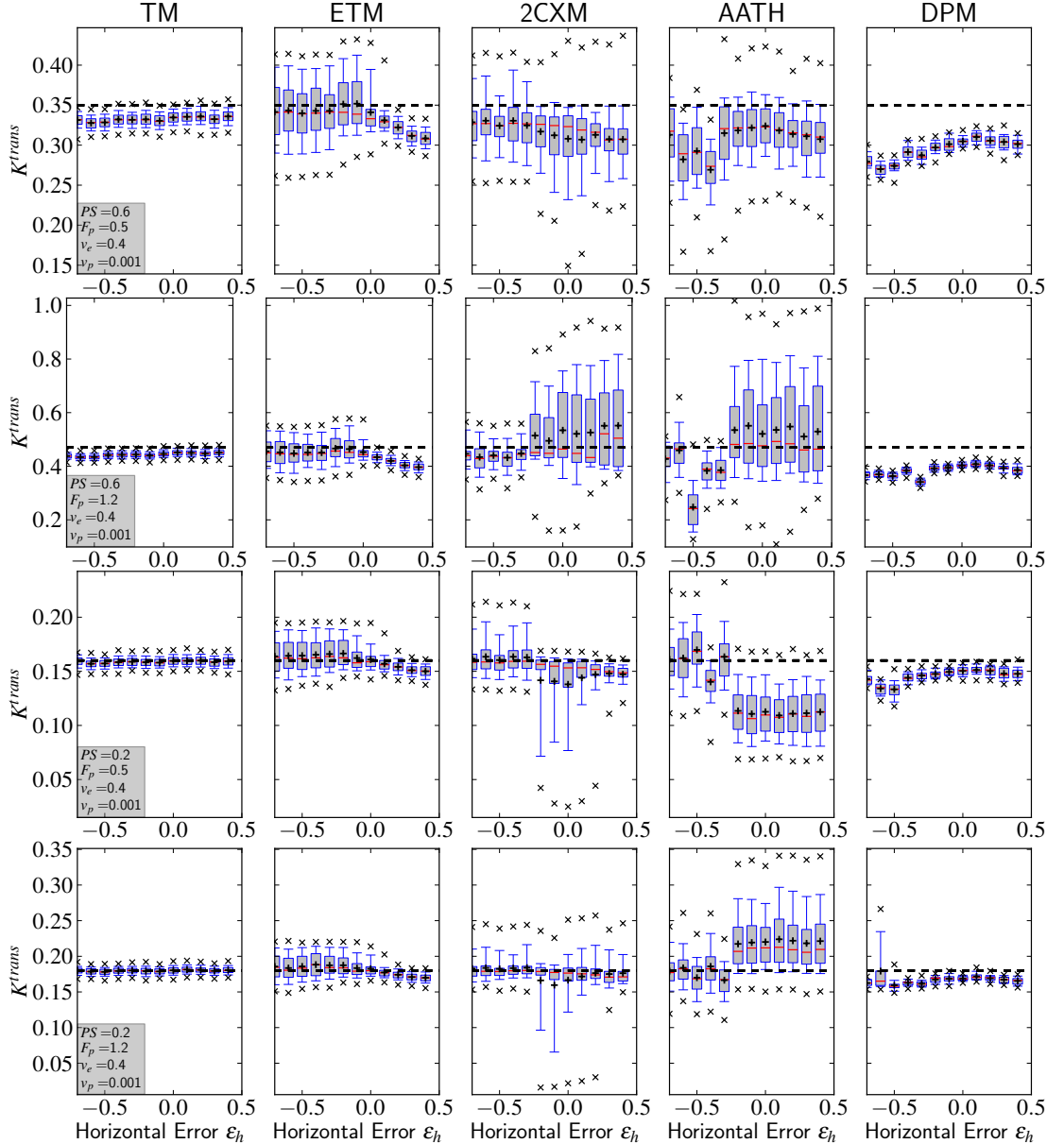


Figure B.26: Accuracy and precision in K^{trans} for human AIFs with a error in the horizontal peak position. The AIFs are shown in Fig. 4.5 on page 27.

B. ADDITIONAL FIGURES

B.3 AIC weighted Parameter Estimates for a Human AIF

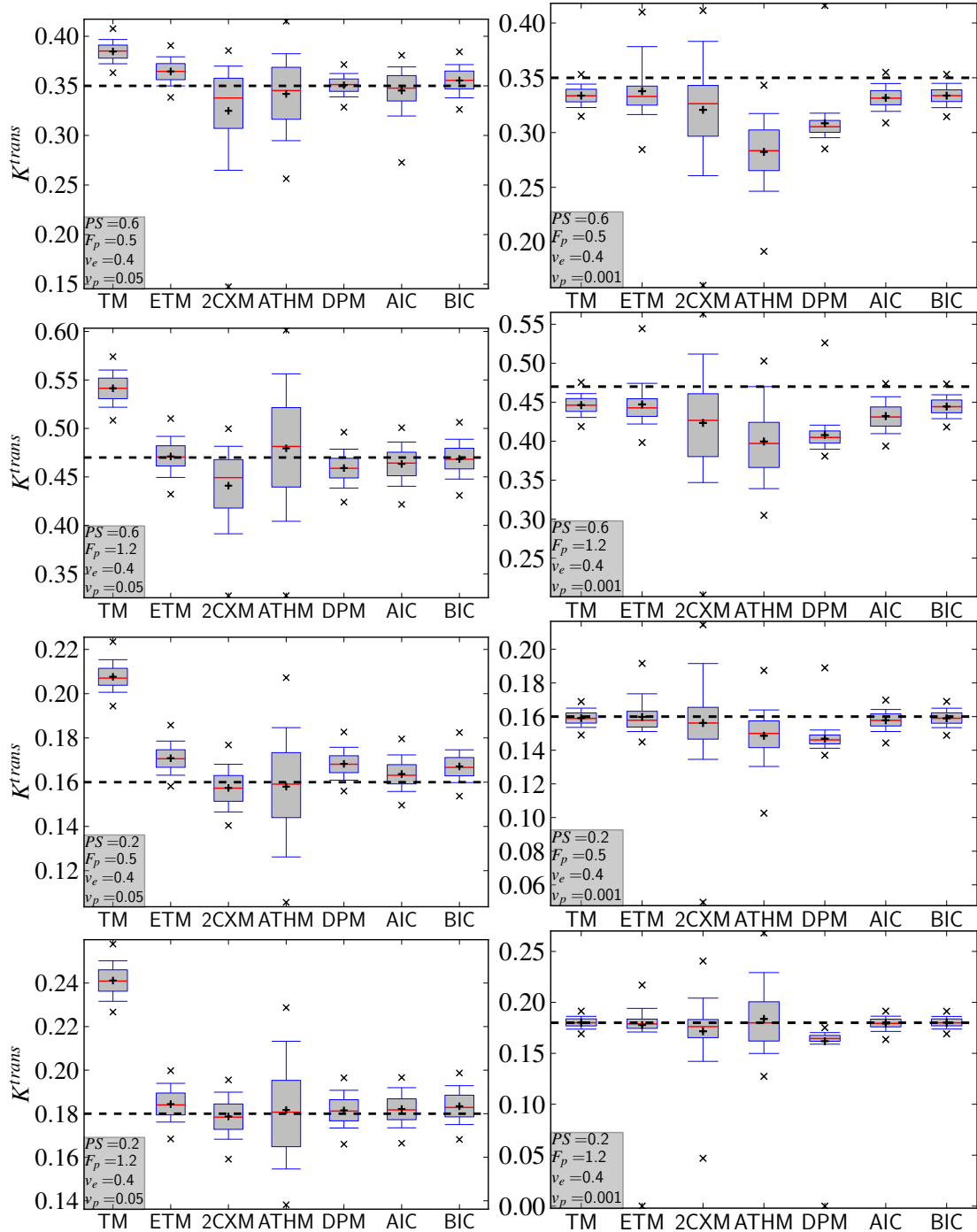


Figure B.27: Comparison of Model Estimates and AIC/BIC weighted averages for a human AIF (unmodified injection rate, Fig. 4.1c).

B.3 AIC weighted Parameter Estimates for a Human AIF

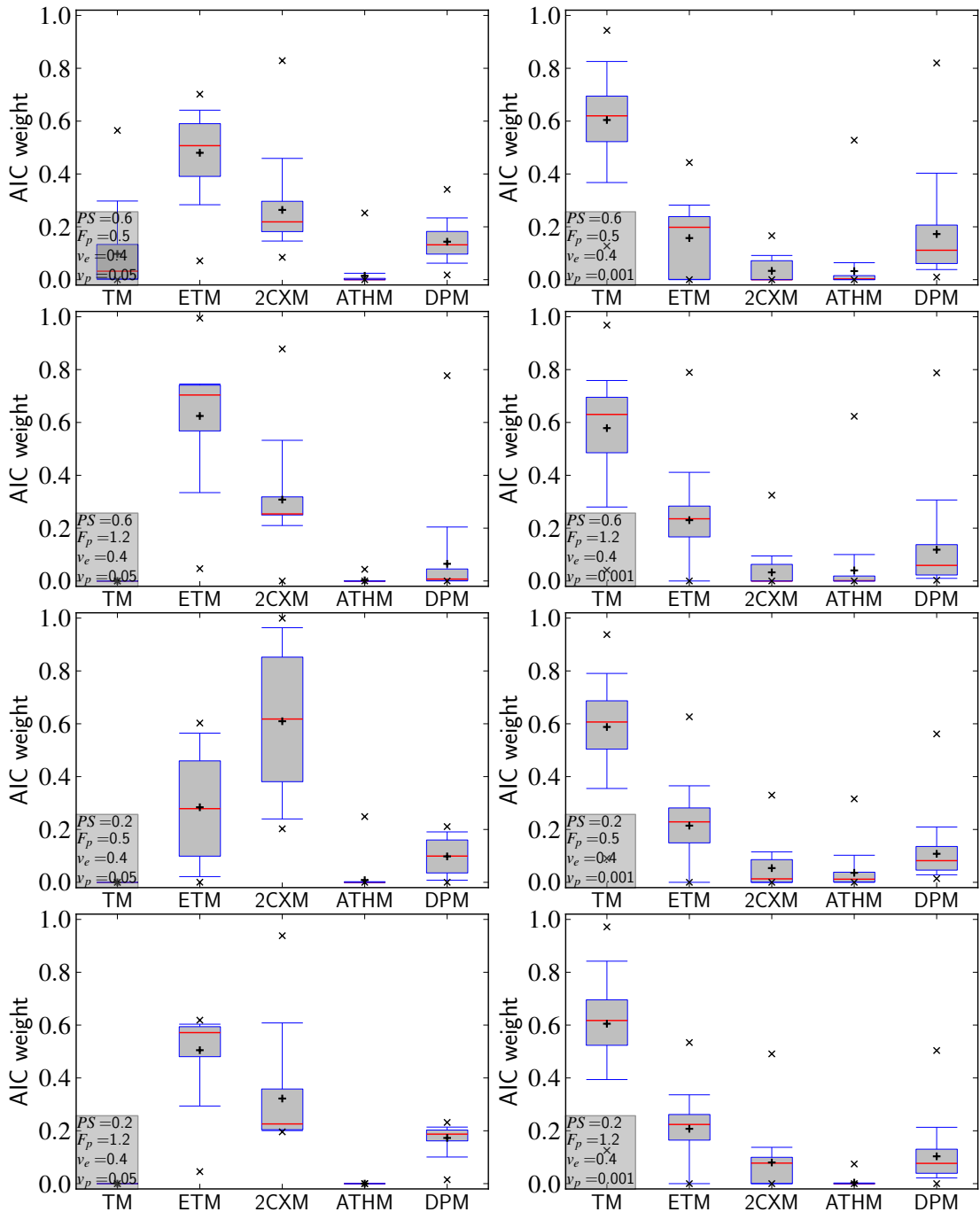


Figure B.28: AIC weights for a human AIF (unmodified injection rate, Fig. 4.1c). Compare to the corresponding parameter estimates in Fig. 6.16

B. ADDITIONAL FIGURES

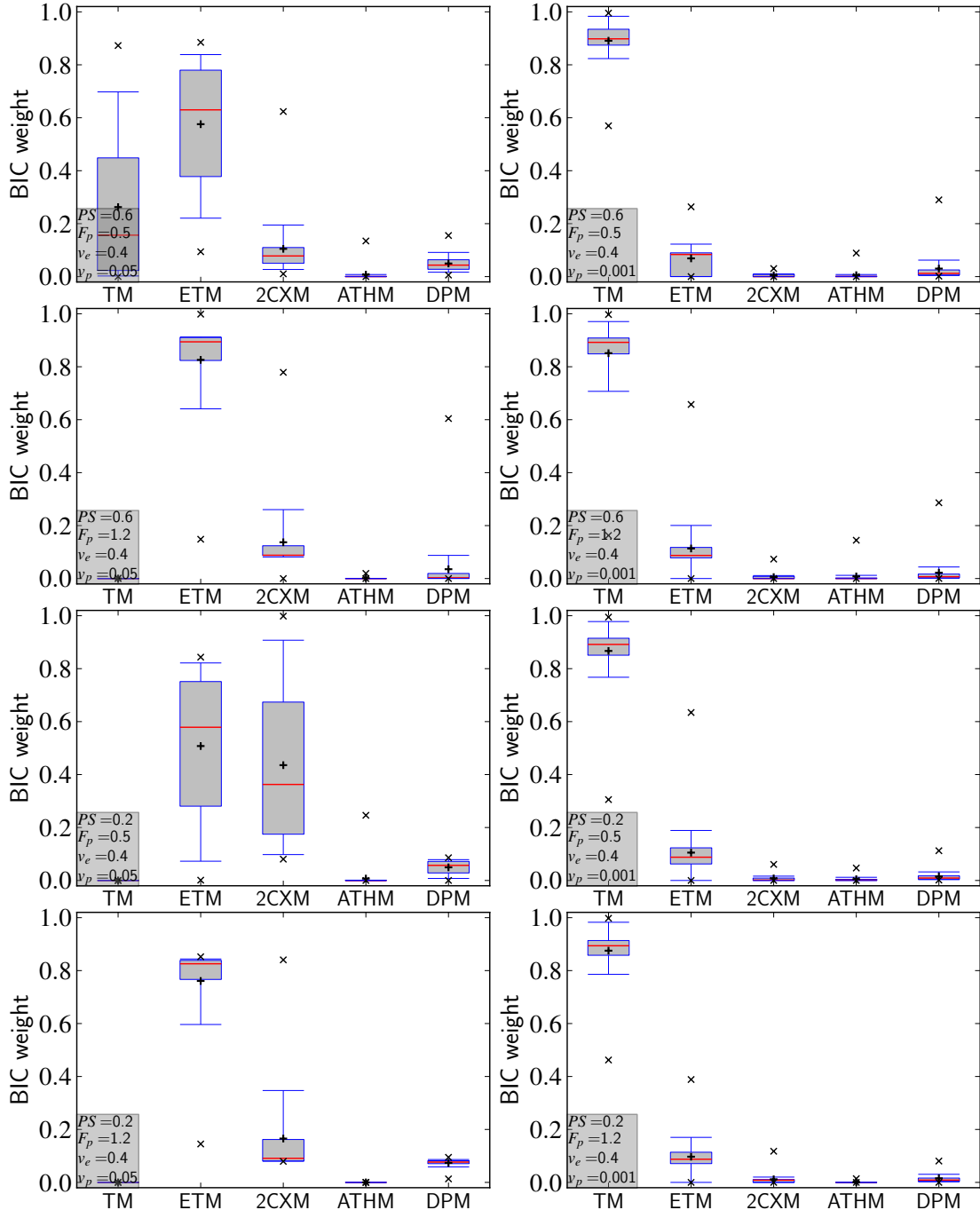


Figure B.29: BIC weights for a human AIF (unmodified injection rate, Fig. 4.1c). Compare to the corresponding parameter estimates in Fig. 6.16

Index

- adiabatic approximation to the tissue homogeneity model, 16
- Akaike information criterion, 31, 32, 68
- Akaike weights, 32
- angiogenesis, 9
- anti angiogenic drugs, 10
- arterial input function, 9, 14
- Bayesian information criterion, 33, 68
- blood-brain barrier, 9
- bolus arrival time, 23, 45
- bootstrap, 29
- box-and-whisker plot, 35
- brute force fitting, 31
- coefficient of variation, 57
- compartmental model, 15, 16
- contrast agents, 8
- convolution, 14
- diffusion, 11
- distributed parameter model, 17
- Ernst angle, 7
- extended Tofts model, 13, 14
- fast low angle shot, 7, 30
- haematocrit, 24, 25, 49
- impulse response function, 14
- initial guesses, 31
- initial parameters, 31
- intravascular retention, 9
- Kulback-Leibler information, 32
- marginal density, 33
- MMID4, 22
- noise conversion, 30
- one-region uptake model, 17
- parameter setup, 22
- parametric bootstrap, 29
- plug-flow model, 12, 15–17, 36
- radiation therapy, 10
- relaxivity, 31
- sampling rate, 68
- SNR, 31, 56, 68
- spoiled gradient acquisition in steady state, 7
- steady-state model, 17
- T2-weighted imaging, 9
- tissue homogeneity model, 15
- tissue-uptake models, 17
- Tofts model, 13, 14
- total acquisition time, 68

INDEX

two-compartment exchange model, [15](#)

vascular tube, [16](#)

References

- AERTS, H.J.W.L., VAN RIEL, N.A.W. & BACKES, W.H. (2008). System identification theory in pharmacokinetic modeling of dynamic contrast-enhanced MRI: influence of contrast injection. *Magnetic resonance in medicine : official journal of the Society of Magnetic Resonance in Medicine / Society of Magnetic Resonance in Medicine*, **59**, 1111–9. [2](#), [19](#), [37](#), [66](#), [68](#)
- AKAIKE, H. (1974a). A new look at the statistical model identification. *Automatic Control, IEEE Transactions on*. [32](#)
- AKAIKE, H. (1974b). Information theory and an extension of the maximum likelihood principle. *Proceeding of the Second International Symposium on Information Theory*,, 267–281. [32](#)
- BAGRI, A., KOUROS-MEHR, H., LEONG, K.G. & PLOWMAN, G.D. (2010). Use of anti-VEGF adjuvant therapy in cancer: challenges and rationale. *Trends in molecular medicine*, **16**, 122–32. [10](#)
- BARBEE, J.H. & COKELET, G.R. (1971). The Fahraeus effect. *Microvascular research*, **3**, 6–16. [25](#), [67](#)
- BARRETT, T., BRECHBIEL, M., BERNARDO, M. & CHOYKE, P.L. (2007). MRI of tumor angiogenesis. *Journal of magnetic resonance imaging : JMRI*, **26**, 235–49. [1](#), [9](#)
- BENJAMINSEN, I.C., BRURBERG, K.G., RUUD, E.B.M. & ROFSTAD, E.K. (2008). Assessment of extravascular extracellular space fraction in human melanoma xenografts by DCE-MRI and kinetic modeling. *Magnetic resonance imaging*, **26**, 160–70. [1](#)
- BERNSTEIN, M., KING, K. & ZHOU, X. (2004). *Handbook of MRI pulse sequences*. [6](#), [8](#)

REFERENCES

- BISDAS, S., KONSTANTINOU, G., SURLAN-POPOVIC, K., KHOSHNEVISZADEH, A., BAGHI, M., VOGL, T.J., KOH, T.S. & MACK, M.G. (2008). Dynamic contrast-enhanced CT of head and neck tumors: comparison of first-pass and permeability perfusion measurements using two different commercially available tracer kinetics models. *Academic radiology*, **15**, 1580–9. [1](#), [16](#), [17](#)
- BRIX, G., KIESSLING, F., LUCHT, R., DARAI, S., WASSER, K., DELORME, S. & GRIEBEL, J. (2004). Microcirculation and microvasculature in breast tumors: pharmacokinetic analysis of dynamic MR image series. *Magnetic Resonance in Medicine*, **52**, 420–9. [15](#)
- BUCKLEY, D. (2002). Uncertainty in the analysis of tracer kinetics using dynamic contrast enhanced T1 weighted MRI. *Magnetic Resonance in Medicine*, **606**, 601–606. [2](#), [14](#), [22](#), [60](#), [65](#)
- BURNHAM, K.P. (2004). Multimodel Inference: Understanding AIC and BIC in Model Selection. *Sociological Methods & Research*, **33**, 261–304. [32](#), [33](#)
- CARAVAN, P., FARRAR, C.T., FRULLANO, L. & UPPAL, R. (2009). Influence of molecular parameters and increasing magnetic field strength on relaxivity of gadolinium- and manganese-based T1 contrast agents. *Contrast media & molecular imaging*, **4**, 89–100. [31](#)
- CAVANAUGH, J. (1997). Unifying the derivations for the Akaike and corrected Akaike information criteria. *Statistics & Probability Letters*. [31](#)
- CAVANAUGH, J.E. & NEATH, A.A. (1999). Generalizing the Derivation of the Schwarz Information Criterion. *Communications in Statistics - Theory and Methods*, **28**, 49–66. [33](#)
- CHENG, H.L.M. (2008). Investigation and optimization of parameter accuracy in dynamic contrast-enhanced MRI. *Journal of magnetic resonance imaging : JMRI*, **28**, 736–43. [2](#), [52](#), [67](#)
- CHOYKE, P.L., DWYER, A.J. & KNOPP, M.V. (2003). Functional tumor imaging with dynamic contrast-enhanced magnetic resonance imaging. *Journal of magnetic resonance imaging : JMRI*, **17**, 509–20. [5](#)
- CHU, K.C., XU, Y., BALSCHI, J.A. & SPRINGER, C.S. (1990). Bulk magnetic susceptibility shifts in nmr studies of compartmentalized samples: use of paramagnetic reagents. *Magnetic Resonance in Medicine*, **13**, 239–262. [8](#)

REFERENCES

- CRONE, C. (1963). the Permeability of Capillaries in Various Organs As Determined By Use of the 'Indicator Diffusion' Method. *Acta physiologica Scandinavica*, **58**, 292–305. [11](#)
- DE NAEYER, D., DE DEENE, Y., CEELEN, W.P., SEGERS, P. & VERDONCK, P. (2011). Precision analysis of kinetic modelling estimates in dynamic contrast enhanced MRI. *Magma (New York, N.Y.)*, **24**, 51–66. [2](#), [57](#)
- DONALDSON, S.B., BUCKLEY, D.L., O'CONNOR, J.P., DAVIDSON, S.E., CARRINGTON, B.M., JONES, A.P. & WEST, C.M.L. (2010). Enhancing fraction measured using dynamic contrast-enhanced MRI predicts disease-free survival in patients with carcinoma of the cervix. *British journal of cancer*, **102**, 23–6. [1](#), [15](#)
- DONALDSON, S.B., BETTS, G., BONINGTON, S.C., HOMER, J.J., SLEVIN, N.J., KERSHAW, L.E., VALENTINE, H., WEST, C.M.L. & BUCKLEY, D.L. (2011). Perfusion estimated with rapid dynamic contrast-enhanced magnetic resonance imaging correlates inversely with vascular endothelial growth factor expression and pimonidazole staining in head-and-neck cancer: a pilot study. *International journal of radiation oncology, biology, physics*, **81**, 1176–83. [1](#), [15](#)
- EFRON, B. (1979). Bootstrap methods: another look at the jackknife. *The annals of Statistics*. [29](#)
- ERNST, R.R. & ANDERSON, W.A. (1966). Application of Fourier Transform Spectroscopy to Magnetic Resonance. *Review of Scientific Instruments*, **37**, 93. [6](#)
- EVANS, S.M. & KOCH, C.J. (2003). Prognostic significance of tumor oxygenation in humans. *Cancer Letters*, **195**, 1–16. [10](#)
- FOLKMAN, J. (1995). Angiogenesis in cancer, vascular, rheumatoid and other disease. *Nat. Med.*, **1**, 27–31. [9](#)
- FOLKMAN, J. (2002). Role of angiogenesis in tumor growth and metastasis. *Semin. Oncol.*, **29**, 15–18. [1](#), [9](#)
- FREEMAN, A. & GOWLAND, P. (1994). Dynamic T1 studies of gadolinium uptake in brain tumors using LL-EPI. *Magnetic Resonance Materials in Physics, Biology and Medicine*, **2**, 409–412. [8](#)
- GAEHTGENS, P. (1980). Flow of blood through narrow capillaries: rheological mechanisms determining capillary hematocrit and apparent viscosity. *Biorheology*, **17**, 183–189. [25](#), [67](#)

REFERENCES

- GARPEBRING, A., OSTLUND, N. & KARLSSON, M. (2009). A novel estimation method for physiological parameters in dynamic contrast-enhanced MRI: application of a distributed parameter model using Fourier-domain calculations. *IEEE transactions on medical imaging*, **28**, 1375–83. [17](#)
- GARPEBRING, A., BRYNOLFSSON, P., YU, J., WIRESTAM, R., JOHANSSON, A., ASKLUND, T. & KARLSSON, M. (2012). Uncertainty estimation in dynamic contrast-enhanced MRI. *Magnetic resonance in medicine : official journal of the Society of Magnetic Resonance in Medicine / Society of Magnetic Resonance in Medicine*, **100**, 2, 992–1002. [2](#)
- HENDERSON, E., RUTT, B. & LEE, T. (1998). Temporal sampling requirements for the tracer kinetics modeling of breast disease. *Magnetic resonance imaging*, **16**, 1057–1073. [24](#)
- HODGSON, R.J., CONNOLLY, S., BARNES, T., EYES, B., CAMPBELL, R.S.D. & MOOTS, R. (2007). Pharmacokinetic modeling of dynamic contrast-enhanced MRI of the hand and wrist in rheumatoid arthritis and the response to anti-tumor necrosis factor-alpha therapy. *Magnetic resonance in medicine : official journal of the Society of Magnetic Resonance in Medicine / Society of Magnetic Resonance in Medicine*, **58**, 482–9. [1](#)
- JACKSON, A., BUCKLEY, D. & PARKER, G. (2005). *Dynamic Contrast-Enhanced Magnetic Resonance Imaging in Oncology*. Springer New York. [5](#), [6](#), [8](#), [11](#)
- JACKSON, A., O'CONNOR, J.P.B., PARKER, G.J.M. & JAYSON, G.C. (2007). Imaging tumor vascular heterogeneity and angiogenesis using dynamic contrast-enhanced magnetic resonance imaging. *Clinical cancer research : an official journal of the American Association for Cancer Research*, **13**, 3449–59. [13](#)
- JOHNSON, J.A. & WILSON, T.A. (1966). A model for capillary exchange. *Am. J. Physiol.*, **210**, 1299–1303. [16](#)
- JUST, N., KOH, D.M., D'ARCY, J., COLLINS, D.J. & LEACH, M.O. (2011). Assessment of the effect of haematocrit-dependent arterial input functions on the accuracy of pharmacokinetic parameters in dynamic contrast-enhanced MRI. *NMR in biomedicine*, **24**, 902–15. [25](#), [43](#), [67](#)
- KERSHAW, L.E. & BUCKLEY, D.L. (2006). Precision in measurements of perfusion and microvascular permeability with T1-weighted dynamic contrast-enhanced MRI.

REFERENCES

- Magnetic resonance in medicine : official journal of the Society of Magnetic Resonance in Medicine / Society of Magnetic Resonance in Medicine*, **56**, 986–92. [2](#), [16](#), [22](#), [65](#)
- KERSHAW, L.E. & CHENG, H.L.M. (2010). Temporal resolution and SNR requirements for accurate DCE-MRI data analysis using the AATH model. *Magnetic resonance in medicine : official journal of the Society of Magnetic Resonance in Medicine / Society of Magnetic Resonance in Medicine*, **64**, 1772–80. [2](#), [56](#)
- KERSHAW, L.E., LOGUE, J.P., HUTCHINSON, C.E., CLARKE, N.W. & BUCKLEY, D.L. (2008). Late tissue effects following radiotherapy and neoadjuvant hormone therapy of the prostate measured with quantitative magnetic resonance imaging. *Radiotherapy and oncology : journal of the European Society for Therapeutic Radiology and Oncology*, **88**, 127–34. [1](#)
- KETY, S. (1951). The theory and applications of the exchange of inert gas at the lungs and tissues. *Pharmacological Reviews*. [11](#)
- KNOPP, M.V., WEISS, E., SINN, H.P., MATTERN, J., JUNKERMANN, H., RADEL-EFF, J., MAGENER, A., BRIX, G., DELORME, S., ZUNA, I. & VAN KAICK, G. (1999). Pathophysiologic basis of contrast enhancement in breast tumors. *Journal of magnetic resonance imaging : JMRI*, **10**, 260–6. [9](#)
- KOH, T.S., CHEONG, L.H., HOU, Z. & SOH, Y.C. (2003). A physiologic model of capillary-tissue exchange for dynamic contrast-enhanced imaging of tumor microcirculation. *IEEE transactions on bio-medical engineering*, **50**, 159–67. [17](#)
- KOH, T.S., THNG, C.H., HARTONO, S., KWEK, J.W., KHOO, J.B.K., MIYAZAKI, K., COLLINS, D.J., ORTON, M.R., LEACH, M.O., LEWINGTON, V. & KOH, D.M. (2011a). Dynamic contrast-enhanced MRI of neuroendocrine hepatic metastases: A feasibility study using a dual-input two-compartment model. *Magnetic resonance in medicine : official journal of the Society of Magnetic Resonance in Medicine / Society of Magnetic Resonance in Medicine*, **65**, 250–60. [1](#), [17](#)
- KOH, T.S., THNG, C.H., HARTONO, S., TAI, B.C., RUMPEL, H., ONG, A.B., SUKRI, N., SOO, R.A., WONG, C.I., LOW, A.S.C., HUMERICKHOUSE, R.A. & GOH, B.C. (2011b). A comparative study of dynamic contrast-enhanced MRI parameters as biomarkers for anti-angiogenic drug therapy. *NMR in biomedicine*, **24**, 1169–80. [1](#), [17](#)

REFERENCES

- KORPORAAL, J.G., VAN VULPEN, M., VAN DEN BERG, C.A.T. & VAN DER HEIDE, U.A. (2012). Tracer kinetic model selection for dynamic contrast-enhanced computed tomography imaging of prostate cancer. *Investigative radiology*, **47**, 41–8. [1](#), [16](#)
- KROLL, K., WILKE, N., JEROSCH-HEROLD, M., WANG, Y., ZHANG, Y., BACHE, R. & JB, B. (1996). Modeling regional myocardial flows from residue functions of an intravascular indicator. *American J Physiol*, **271**, H1634–H1655. [2](#), [22](#)
- KULLBACK, S. & LEIBLER, R. (1951). On information and sufficiency. *The Annals of Mathematical Statistics*. [31](#)
- KUPERMAN, V. (2000). *Magnetic Resonance Imaging - Physical Principles and Applications*. Academic Press. [6](#)
- LARSON, B., MARKHAM, J. & RAICHLE, M.E. (1987). Tracer-Kinetic Models for Measuring Cerebral Blood Flow Using Externally Detected Radiotracers. 443–463. [17](#)
- LAWRENCE, K. & LEE, T. (1998). An adiabatic approximation to the tissue homogeneity model for water exchange in the brain: I. Theoretical derivation. *Journal of Cerebral Blood Flow & Metabolism*, 1365–1377. [16](#), [24](#)
- LEEUW, D. (1992). J.(1992). Introduction to Akaike (1973) Information theory and an extension of the maximum likelihood principle. *Breakthroughs in Statistics (S. Kotz and NL Johnson,* [31](#)
- LEVENBERG, K. (1944). A method for the solution of certain non-linear problems in least-squares. *Quarterly of Applied Mathematics*, **2**, 164–168. [31](#)
- LEVITT, M. (2008). *Spin Dynamics*. John Wiley and Sons, Ltd, second edi edn. [6](#)
- LI, X., WELCH, E.B., ARLINGHAUS, L.R., CHAKRAVARTHY, A.B., XU, L., FARLEY, J., LOVELESS, M.E., MAYER, I.A., KELLEY, M.C., MESZOELY, I.M., MEANS-POWELL, J.A., ABRAMSON, V.G., GRAU, A.M., GORE, J.C. & YANKEELOV, T.E. (2011). A novel AIF tracking method and comparison of DCE-MRI parameters using individual and population-based AIFs in human breast cancer. *Physics in medicine and biology*, **56**, 5753–69. [43](#)
- LOVELESS, M.E., HALLIDAY, J., LIESS, C., XU, L., DORTCH, R.D., WHISENANT, J., WATERTON, J.C., GORE, J.C. & YANKEELOV, T.E. (2012). A quantitative comparison of the influence of individual versus population-derived vascular input

REFERENCES

- functions on dynamic contrast enhanced-MRI in small animals. *Magnetic Resonance in Medicine*, **67**, 226–36. [43](#)
- LUYPAERT, R., SOURBRON, S. & DE MEY, J. (2011). Validity of perfusion parameters obtained using the modified Tofts model: a simulation study. *Magnetic resonance in medicine : official journal of the Society of Magnetic Resonance in Medicine / Society of Magnetic Resonance in Medicine*, **65**, 1491–7. [22](#), [65](#)
- LUYPAERT, R., INGRISCH, M., SOURBRON, S. & DE MEY, J. (2012). The Akaike information criterion in DCE-MRI: does it improve the haemodynamic parameter estimates? *Physics in medicine and biology*, **57**, 3609–28. [22](#), [60](#), [65](#), [66](#), [68](#)
- MCGRATH, D.M., BRADLEY, D.P., TESSIER, J.L., LACEY, T., TAYLOR, C.J. & PARKER, G.J.M. (2009). Comparison of model-based arterial input functions for dynamic contrast-enhanced MRI in tumor bearing rats. *Magnetic resonance in medicine : official journal of the Society of Magnetic Resonance in Medicine / Society of Magnetic Resonance in Medicine*, **61**, 1173–84. [43](#)
- MENG, R., CHANG, S.D., JONES, E.C., GOLDENBERG, S.L. & KOZLOWSKI, P. (2010). Comparison between population average and experimentally measured arterial input function in predicting biopsy results in prostate cancer. *Academic radiology*, **17**, 520–5. [43](#)
- MEYER, E. (1989). Simultaneous correction for tracer arrival delay and dispersion in CBF measurements by the H₂15O autoradiographic method and dynamic PET. *Journal of nuclear medicine : official publication, Society of Nuclear Medicine*, **30**, 1069–78. [24](#)
- MICHOUX, N., HUWART, L., ABARCA-QUINONES, J., DORVILLIUS, M., ANNET, L., PEETERS, F. & VAN BEERS, B.E. (2008). Transvascular and interstitial transport in rat hepatocellular carcinomas: dynamic contrast-enhanced MRI assessment with low- and high-molecular weight agents. *Journal of magnetic resonance imaging : JMRI*, **28**, 906–14. [1](#), [16](#)
- MORAN, G.R. & PRATO, F.S. (2001). Modeling Tissue Contrast Agent Concentration : A Simulated Arterial Input Function. *Magnetic Resonance in Medicine*, **45**, 42–45. [16](#)
- MOROZ, J., WONG, C.L., YUNG, A.C., KOZLOWSKI, P. & REINSBERG, S.A. (2013). Rapid measurement of arterial input function in mouse tail from projection phases.

REFERENCES

- Magnetic resonance in medicine : official journal of the Society of Magnetic Resonance in Medicine / Society of Magnetic Resonance in Medicine*, **000**, 1–8. [20](#), [21](#)
- NAISH, J.H., KERSHAW, L.E., BUCKLEY, D.L., JACKSON, A., WATERTON, J.C. & PARKER, G.J.M. (2009). Modeling of contrast agent kinetics in the lung using T1-weighted dynamic contrast-enhanced MRI. *Magnetic resonance in medicine : official journal of the Society of Magnetic Resonance in Medicine / Society of Magnetic Resonance in Medicine*, **61**, 1507–14. [1](#), [16](#)
- O'CONNOR, J.P.B., JACKSON, A., PARKER, G.J.M. & JAYSON, G.C. (2007). DCE-MRI biomarkers in the clinical evaluation of antiangiogenic and vascular disrupting agents. *British journal of cancer*, **96**, 189–95. [1](#)
- PADHANI, A.R. (1999). Dynamic contrast-enhanced MRI studies in human tumours. *The British journal of radiology*, **72**, 427–31. [9](#)
- PARKER, G.J.M., ROBERTS, C., MACDONALD, A., BUONACCORSI, G.A., CHEUNG, S., BUCKLEY, D.L., JACKSON, A., WATSON, Y., DAVIES, K. & JAYSON, G.C. (2006). Experimentally-derived functional form for a population-averaged high-temporal-resolution arterial input function for dynamic contrast-enhanced MRI. *Magnetic resonance in medicine : official journal of the Society of Magnetic Resonance in Medicine / Society of Magnetic Resonance in Medicine*, **56**, 993–1000. [20](#), [21](#), [25](#), [67](#)
- PICKUP, S., ZHOU, R. & GLICKSON, J. (2003). MRI Estimation of the Arterial Input Function in Mice. *Academic Radiology*, **10**, 963–968. [43](#)
- RIBATTI, D., VACCA, A. & PRESTA, M. (2000). The discovery of angiogenic factors: a historical review. *General pharmacology*, **35**, 227–31. [9](#)
- ROBERTS, C., HUGHES, S., NAISH, J.H., HOLLIDAY, K., WATSON, Y., CHEUNG, S., BUONACCORSI, G.A., YOUNG, H., CLARKE, N. & PARKER, G.J. (2011). Use of An Individually Measured Hematocrit in DCE-MRI studies. In *Proc. Intl. Soc. Mag. Reson. Med.*, vol. 19, 1078. [25](#), [49](#), [67](#)
- SANGREN, W.C. & SHEPPARD, C.W. (1953). A mathematical derivation of the exchange of a labeled substance between a liquid flowing in a vessel and an external compartment*. *Bulletin of Mathematical Biophysics*, **15**, 387–394. [17](#)

REFERENCES

- SCHWARZ, G. (1978). Estimating the dimension of a model. *The Annals of Statistics*, **6**, 461–464. [33](#)
- SINGH, A., RATHORE, R.K.S., HARIS, M., VERMA, S.K., HUSAIN, N. & GUPTA, R.K. (2009). Improved bolus arrival time and arterial input function estimation for tracer kinetic analysis in DCE-MRI. *Journal of magnetic resonance imaging : JMRI*, **29**, 166–76. [24](#)
- SINGH, K. & XIE, M. (2009). Bootstrap: A Statistical Method. [29](#)
- SLICHTER, C. (1990). *Principles of magnetic resonance*. Springer-Verlag, third edit edn. [6](#)
- SOURBRON, S., INGRISCH, M., SIEFERT, A., REISER, M. & HERRMANN, K. (2009). Quantification of cerebral blood flow, cerebral blood volume, and blood-brain-barrier leakage with DCE-MRI. *Magnetic resonance in medicine : official journal of the Society of Magnetic Resonance in Medicine / Society of Magnetic Resonance in Medicine*, **62**, 205–17. [1](#)
- SOURBRON, S.P. & BUCKLEY, D.L. (2011). On the scope and interpretation of the Tofts models for DCE-MRI. *Magnetic Resonance in Medicine*, **66**, 735–45. [15](#)
- SOURBRON, S.P. & BUCKLEY, D.L. (2013). Classic models for dynamic contrast-enhanced MRI. *NMR in biomedicine*. [1](#), [11](#), [17](#), [22](#)
- SUGIURA, N. (1978). Further analysts of the data by akaike' s information criterion and the finite corrections. *Communications in Statistics - Theory and Methods*, **7**, 13–26. [32](#)
- THOMASSIN-NAGGARA, I., BALVAY, D., CUENOD, C.A., DARAÏ, E., MARSAULT, C. & BAZOT, M. (2010). Dynamic contrast-enhanced MR imaging to assess physiologic variations of myometrial perfusion. *European radiology*, **20**, 984–94. [1](#), [15](#)
- TOFTS, P.S. (1997). Modeling tracer kinetics in dynamic Gd-DTPA MR imaging. *J Magn Reson Imaging*, **7**, 91–101. [1](#), [14](#)
- TOFTS, P.S., BERKOWITZ, B. & SCHNALL, M.D. (1995). Quantitative analysis of dynamic Gd-DTPA enhancement in breast tumors using a permeability model. *Magn Reson Med*, **33**, 564–568. [1](#)

REFERENCES

TOFTS, P.S., BRIX, G., BUCKLEY, D.L., EVELHOCH, J.L., HENDERSON, E., KNOPP, M.V., LARSSON, H.B., LEE, T.Y., MAYR, N.A., PARKER, G.J., PORT, R.E., TAYLOR, J. & WEISSKOFF, R.M. (1999). Estimating kinetic parameters from dynamic contrast-enhanced T(1)-weighted MRI of a diffusible tracer: standardized quantities and symbols. *Journal of magnetic resonance imaging : JMRI*, **10**, 223–32.

[14](#)

VAUPEL, P. (2004). Tumor microenvironmental physiology and its implications for radiation oncology. *Seminars in radiation oncology*, **14**, 198–206. [10](#)

WEISHAUPt, D., KÖCHLI, V.D. & MARINCEK, B. (2006). *How Does MRI Work? An Introduction to the Physics and Function of Magnetic Resonance Imaging..* Springer-Verlag, Berlin Heidelberg, second edi edn. [6](#)

XIANG, Q.S. (2012). Lecture at UBC - PHYS540 - Chapter 6 - Fast Imaging. [6](#)

YANKEELOV, T. & GORE, J. (2009). Dynamic contrast enhanced magnetic resonance imaging in oncology: theory, data acquisition, analysis, and examples. *Current medical imaging reviews*, **3**, 91–107. [1](#), [6](#), [8](#), [9](#)

Declaration

I confirm that the work presented in this research report has been performed and interpreted solely by myself except where identified to the contrary.

Hiermit versichere ich, dass ich die vorliegende Arbeit selbstständig verfasst und keine anderen als die angegebenen Quellen und Hilfsmittel verwendet habe.

Vancouver, September 2013



Tammo Rukat